STRUCTURE-PROPERTY RELATIONSHIPS IN ALLOY CATALYSTS AS DETERMINED USING *AB-INITIO* METHODS

by

Liang Cao

A dissertation submitted to The Johns Hopkins University in conformity with the requirements for the degree of Doctor of Philosophy.

Baltimore, Maryland
October, 2016

Abstract

The cluster expansion approach, with the training data calculated by density functional theory (DFT) calculations, is used to investigate the structure-property relationships of Pt_3Ni alloy catalysts for oxygen reduction reaction (ORR) at atomic level so as to enable the rational design of catalysts with desired catalytic activity and stability by tailoring surface structures. Firstly, a cluster expansion built on extended surfaces is developed to construct a direct bridge between the atomic structure and ORR catalytic activity of Pt-Ni alloy catalysts at a variety of compositions and chemical environments. Thermodynamically stable $Pt_3Ni(111)$ extended surfaces are predicted to have substantial sub-surface disorder, and as a result the ORR activity of different surface sites varies by approximately three orders of magnitude. Using this model, I identify a $Pt_3Ni(111)$ surface with a multi-layer Pt skin that is predicted to maximize catalytic activity.

Secondly, a cluster expansion built on nanoparticles has been developed to investigate the structure and stability of Pt-Ni and Pt-Ni-Mo nanoparticles in both vacuum and oxidizing conditions. For Pt-Ni nanoparticles, my calculations indicate that the preferential oxidation of edge sites makes (111) facet sites more vulnerable to dissolution than edge sites. Furthermore, I predict that for Mo-doped Pt_3Ni nanoparticles with only a small amount of Mo doping (around 1.6% molar), the equilibrium concentration of Ni atoms on the particle surface is greatly reduced, limiting the rate at which Ni atoms dissolve from the particles.

Mo doping also increases Pt/Ni vacancy formation energies in the surface layer, which further stabilizes the nanoparticles against Ni dissolution and may help preserve the nanoparticle shape.

Finally, the thermodynamics of CO_2/CO reduction on four different copper (Cu) facets, Cu(211), Cu(110), Cu(100) and Cu(111), are investigated by building the free energy diagrams for CO_2/CO reduction to C_1 and C_2 products. For two possible reaction mechanisms of C-C coupling, CHO-CHO coupling and CO-CO coupling mechanisms, the Cu(110) facet is identified to be the surface with the lowest onset potential (about -0.30 V), which is in agreement with the most recent experimental observation of high catalytic activities and selectivity on highly dense Cu nanowires.

Thesis Advisor: Professor Tim Mueller

Thesis Reader: Professor Chao Wang

Thesis Committee: Michael Falk, Robert Leheny, Tim Mueller, Dan Reich, and Chao Wang.

Acknowledgement

First and foremost, I would like to acknowledge my Ph.D. advisor, Prof. Tim Mueller, for his guidance, patience and support in all these years. I first met Prof. Mueller in the second year of my Ph.D. period when I had trouble in choosing my research topics and considered quitting graduate school. Without his support and guidance, I would not have finished my Ph.D. thesis. I have learned a lot from his broad knowledge of materials science and tremendous experiences of computational simulation. I am also beneficial from his attitude to scientific research and persistent pursuit of creativity. Although there were difficult times during my thesis research, he always encourages me and keeps my study in the right direction. I enjoy the five years working with Prof. Mueller.

I thank Prof. Chao Wang and his graduate student, David Raciti, from the Department of Chemical and Biomolecular Engineering, who are my experimental collaborators. Mueller group (theoretical side) and Wang group (experimental side) closely work together to investigate CO_2/CO reduction mechanisms on copper nanowires (related work will be demonstrated in Chapter 5). I also would like to thank Chao Wang for insightful comments on my thesis. My deepest gratitude also goes to Prof. Dan Reich, he is not only my first-year faculty mentor, but also serves as my advisor in the Department of Physics and Astronomy. I would like to acknowledge him for his encouragement, support and a lot of valuable advice. I also want to thank Prof. Michael Falk, who introduced Prof. Mueller to me as a potential research advisor even before Prof. Mueller came to Hopkins. I also

acknowledge Prof. Mueller, Prof. Reich, and Prof. Falk for their services on my thesis advisory committee. I also want to thank my thesis committee members: Prof. Michael Falk, Prof. Robert Leheny, Prof. Tim Mueller, Prof. Dan Reich, and Prof. Chao Wang.

My thanks also go to André Botelho, Fenglin Yuan, Pandu Wisesa, Thomas Nilson, Chenyang Li, Peter Lile, Alberto Hernandez-Valle, Kyle McGill, and the rest of my labmates in the Mueller's group for making our lab friendly and supportive. I also acknowledge Fenglin for his helpful comments on my thesis. I thank my fellow graduate students for their friendship and company at Hopkins. I also would like to acknowledge the help from Carm, Kelley, Marge, Ada and the rest of the administrative staff in both the Department of Physics and Astronomy, and the Department of Materials Science and Engineering.

Last but not least, I would like to thank my family, my parents and my elder brother, for their unconditional love and support.

Dedication

This thesis is dedicated to my family, who offer unconditional love and support in my Ph.D. period and much beyond.

Contents

List of Tables

List of Figures

Chapter 1

Introduction

1.1 Progress in the cluster expansion computational research

The cluster expansion[1] is a lattice Hamiltonian, which is a generalized Ising model[2]. In Condensed Matter Physics and Materials Science, the cluster expansions have proven to be a valuable tool, and are widely used to investigate structure-property relationships for AB binary or ABC ternary material systems that share a similar underlying lattice.[3-13]

The benefit of a cluster expansion is that only fitted to a relatively small number of training structures, I can use the cluster expansion Hamiltonian to rapidly and accurately predict the properties (such as energy) of structures with all possible and random atomic configurations under different ensembles, such as canonical ensemble, and grand canonical ensemble. The typical prediction speed is millions of structures per minute. In order to have a better understanding of the interested material (such as, draw the phase diagrams, identify the ground state structures, and calculate thermodynamic averages of material properties), it is necessary for us to screen through the space of all possible configurations of material

system, the number of which can be tremendously larger than that of training structures. Thus, cluster expansions can help scientists dramatically reduce the computational cost and speed up the process of investigation.

To realize the cluster expansion Hamiltonian for a specific material system, the computational cost to generate the required training data can be computationally expensive (such as, density functional theory (DFT)[14-16] calculations). In recent years, scientists have made a lot of efforts to develop methods of selecting training structures in a way that efficiently reduces the number of training structures for a targeted prediction error.[17-20] In 2009, Mueller et al.[21] developed a Bayesian approach to cluster expansions that explicitly introduce physical insights into the fitting procedure so as to highly improve the accuracy of cluster expansions for a given set of training structures. This Bayesian approach can be used to efficiently generate cluster expansion training set for low-symmetry systems, such as extended surfaces and nanoparticles.[21]

Here, I give some recent examples that cluster expansions were developed to investigate the structure-property relationships of material systems. For the 3-dimensional bulk lattice, the cluster expansion was applied to calculate the phase diagrams of binary systems (Si-Ge, CaO-MgO, Ti-Al, and Cu-Au).[18] Also, it has been used to search for the equilibrium and ground state (or low-energy) structures for lithium imide (Li_2NH).[13, 22]

With the speed of scientific computation increases, the calculation of low-symmetrical systems becomes possible, which enables the generation of cluster expansions for extended surfaces and nanoparticles. For extended surfaces, in 1999, Sadigh et al.[23] used cluster expansion built on monolayer of PdAu alloys on Ru(0001) to investigate the phase stability. This implementation of cluster expansion on monolayer is a typical example that cluster

expansion is a generalized Ising model. In 2004, instead of monolayer, Wieckhorst et al.[24] developed a cluster expansion on multilayer extended Co-Al surfaces to construct a phase diagram for fully-relaxed CoAl binary alloy surfaces. In 2005, a cluster expansion was built on a fcc(111) alloy surface of $Pt_{(1-x)}Au_x$ to study the surface segregation and ordering of alloy surfaces in the presence of adsorbed oxygen atoms.[25]

For nanoparticles, in 2010, Mueller et al.[26] investigated the nanoparticle-size effect on hydrogen release from sodium alanate ($NaAlH_4$) nanoparticles using a size and shape changeable cluster expansion. In 2012, Tan et al.[27] built a cluster expansion on a 55-atom Pd-Pt cuboctahedral nanoparticles to search for ground state structures. In 2014, Yuge[28] built cluster expansions for $Pt_{28}Rh_{27}$ nanoparticles with fixed shape and size, and demonstrated that the electronic structures of surface Pt d-band at specific site can be tuned by changing surrounding atomic orders, which enables the control of molecular adsorption energy and catalytic properties of nanoparticle surface sites.

1.2 Progress in Pt/Ni alloy catalysts for Oxygen Reduction Reaction

Because of the limited supply of fossil fuels and pollution caused by consuming them, future energy needs to transition from fossil fuels to some new, more environmentally friendly, and renewable energy sources. Fuels cells that can directly convert chemical energy of fossil fuels to electricity by electrochemical processes are one of these potential sources.[29-31] Among all of the existing fuel cells, the proton exchange membrane fuel cell (PEMFC) has been actively studied for commercial use in the areas of transportation, stationary, and portable power generation. The work mechanism of fuel cell is as follows. In the acidic environment, the oxygen reduction reaction (ORR) happens at the cathode by reducing oxygen (O_2) via following step:

$$O_2(g) + 4(H^+ + e^-) \leftrightarrow 2H_2O(l). \quad (1.1)$$

The electrons and protons $(H^+ + e^-)$ needed in Eq.(1.1) are produced by oxidizing hydrogen (H_2) at the anode of a PEMFC and then transferred to the cathode through the proton exchange membrane. This hydrogen oxidation reaction is called as HOR, which can be expressed as:

$$H_2(g) \leftrightarrow 2(H^+ + e^-). \quad (1.2)$$

We need low-price, and high-activity catalysts to improve the reaction rates of HOR at the anode and ORR at the cathode. So far, Pt has been considered as one of the most promising candidates for fuel cell catalysts.[32-35] Both cathode and anode electrodes are

loaded with highly dispersed Pt-based nanoparticles (NPs) supported on carbon black (Pt/C). Since the reaction rate of HOR at the anode is extremely fast compared with that of ORR at the cathode,[31, 36-37] it is the reaction rate of ORR at the cathode that limits the efficiency of fuel cells. The economic viability of these fuel cells is constraint by three main challenges, the high cost of catalysts, the sluggish kinetics of the oxygen reduction reaction (ORR), and the low durability of the catalysts in oxidizing conditions.

For the first challenge, alloying Pt with transition metals M (M = Fe[38-40], Co[38, 41-42], Ni[38, 41, 43-44], etc.) will not only reduce the cost of catalysts, but also enhance the ORR activity compared with pure Pt. Pt-Ni alloy catalysts are among the most successful Pt-based alloy catalysts for ORR. Their catalytic properties have been studied extensively by experimental[34-35, 38, 43, 45] and computational[46-51] methods. Recent experimental and theoretical works have shown that Pt_3Ni alloys have a much higher oxygen reduction reaction (ORR) activity than pure Pt.[50, 52-53] Stamenkovic et al.[53] synthesized and measured the ORR activity of $Pt_3Ni(111)$ extended surfaces with Pt-skin structures, and demonstrated that these have a 90-fold enhancement of specific activity versus commercial Pt/C catalysts. Recently, Huang et al.[54] reported Pt_3Ni nanoparticles with a very small amount of molybdenum (Mo) doping (1.6% in molar) have highly enhanced ORR activity and durability, with a specific activity of 10.3 mA/cm^2 and mass activity of 6.98 A/mg_{Pt}, which are 81- and 73-fold enhancements compared with the commercial Pt/C catalyst (0.127 mA/cm^2 and 0.096 A/mg_{Pt}).

In the field of chemical catalysis, in order to have optimal catalytic activity, the qualitative Sabatier principle, which can be graphically shown in a volcano plot, states that the interactions between the intermediate adsorbates (e.g. adsorbed O and adsorbed OH for

ORR) and the surface of catalysts should be "just right" (meaning neither too strong nor too weak). The oxygen binding energy (ΔE_O) has been shown to be a valuable descriptor for ORR activity.[48-49, 55-56] Here I represent the oxygen binding energy as the potential energy of oxygen adsorption, ΔE_O, calculated as

$$\Delta E_O = \mathrm{E_{DFT}}\left(\mathrm{slab{+}{*}O}\right) - \mathrm{E_{DFT}}\left(\mathrm{slab}\right) + \mathrm{E_{DFT}}\left(\mathrm{H_2}\right) - \mathrm{E_{DFT}}\left(\mathrm{H_2O}\right). \quad (1.3)$$

In Eq. (1.3), $\mathrm{E_{DFT}}\left(\mathrm{slab{+}{*}O}\right)$ is the total DFT energy of the slab with an adsorbed oxygen atom, $\mathrm{E_{DFT}}\left(\mathrm{slab}\right)$ is the DFT energy of the clean slab, and $\mathrm{E_{DFT}}\left(\mathrm{H_2}\right)$ and $\mathrm{E_{DFT}}\left(\mathrm{H_2O}\right)$ are the DFT energies of gas-phase H_2 and H_2O. My choice of H_2(g) and H_2O(g) as reference states avoids potential errors in the calculation of the energy of O_2(g) and allows for more direct comparisons with previous calculations.[55] By this definition, lower ΔE_O indicates stronger binding between oxygen and Pt/Ni(111) surface, while larger ΔE_O indicates weaker oxygen binding. The oxygen binding energy mentioned in this thesis stands for ΔE_O in Eq. (1.3) unless otherwise noted.

Theoretically, according to a Sabatier volcano plot (Figure 1.1), there is still room for enhancement of catalytic activity. To further reduce the second challenge of sluggish kinetics of the ORR, scientists need to design a catalytic system with optimal oxygen binding energy so as to reach the peak of the volcano plot, where oxygen binding was predicted to be ~0.2 eV weaker than the oxygen binding on pure Pt(111).[57]

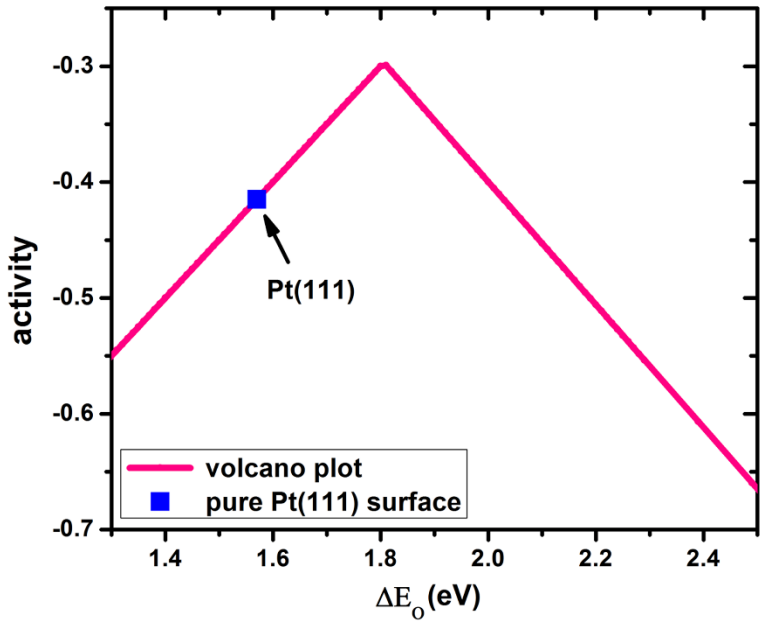

Figure 1.1. A volcano plot at an applied potential of 0.9 V under associative mechanism based on the work of Karlberg et al.[56] The peak is at $\Delta E_O = 1.81$ eV. The value of ΔE_O used in this plot for pure Pt(111) is at 1/4 ML oxygen coverage.

For the third challenge, Ni atoms tend to dissolve in oxidizing conditions compared with Pt.[54, 58-59] Although alloying Ni can enhance the activity and lower the cost, it has the disadvantage of low durability under the cell operating conditions. Typically, the Pt_3Ni alloy catalysts will lose at least ~50% of the mass activity of ORR after 8000 potential cycles.[54, 60] For instance, in the work of Beermann et al.[60], the result of electrochemical durability of synthesized Pt-Ni/C octahedral nanoparticles using the accelerated durability test (ADT) between 0.6 V and 1.1 V versus the reversible hydrogen electrode (RHE) is as follows. The initial mass activity of ORR is 1.0 A/mg_{Pt}, which is dramatically reduced to 0.5 A/mg_{Pt} (by a factor of ~2) after 4000 cycles, and even further to 0.25 A/mg_{Pt} (by a factor of ~4) after 8000 cycles. All further potentials discussed in this thesis are versus the RHE unless otherwise noted. A similar loss of activity for Pt_3Ni/C nanoparticles was reported in

the work of Huang et al.[54] Tailoring surface structures of Pt-based catalysts so as to tune their electronic structure can help prevent Ni atoms on the surface (near surface) dissolution, and stabilize the morphology of catalysts. The newly developed synthesis approaches of multi-layer Pt-skin[61], transition metal doping (such as doping Mo[54], and doping Rh[60]), interior erosion of $PtNi_3$ to form Pt-rich nanoframes[58], and Pt-based nanocages[62], have highly improved the stability and catalytic activity of Pt-Ni alloy catalysts.

1.3 Cluster expansion models developed in this thesis

In order to investigate the thermodynamic and catalytic properties of Pt-Ni alloy catalysts, computational cluster expansion models for Pt-Ni extended surfaces and Pt-Ni nanoparticles are developed to build a direct bridge between the atomic order and Hamiltonian of alloy systems. The developed cluster expansion Hamiltonians enable Monte Carlo simulations on the Pt-Ni catalysts under different thermodynamic ensembles.

For Pt-Ni extended surfaces, in order to predict the interaction between near-surface atomic order of catalysts and the adsorbed species (e.g., *O) on the surface of Pt_3Ni alloys, a cluster expansion for the Pt-Ni(111) surface with up to a monolayer of adsorbed atomic oxygen (Pt-Ni-Oxygen surface system) was generated, the details of which are provided in Chapter 3. The canonical ensemble, grand canonical ensemble and mixed ensemble of Pt-Ni-Oxygen surface system are implemented under different constraints to allow for setting a variety of temperatures, Pt compositions, oxygen coverages, and chemical potentials to mimic the real-world synthesis and electrochemical environments. By performing Monte Carlo simulations to accurately and rapidly screen through all possible configurations of Pt_3Ni surfaces, I am able to calculate thermodynamic averages, build phase diagrams of Pt-Ni surfaces and identify ground state structures under different combination of chemical environments. Furthermore, based on the local atomic order nearby the oxygen adsorbed site (fcc or hcp), this cluster expansion can predict the oxygen binding energy, which has a linear relationship with ORR activity (volcano plot,[55-57] shown in Figure 1.1). By introducing a computational average current over all possible fcc oxygen binding sites to

define the specific activity of Pt-Ni surfaces, this cluster expansion can be used to search for the surface structures with optimal ORR activity.

In addition to the Pt-Ni extended surfaces, I also developed cluster expansions for the Pt-Ni nanoparticles since they have been found to be highly active as the ORR catalysts.[54, 59, 63] The cluster expansion built on the extended surfaces is not capable of capturing the edge/vertex effects on the stability and catalytic activity of nanocrystals. Thus, it is straightforward for us to extend the cluster expansion to alloy nanoparticles. To my knowledge, this is the first use of a single cluster expansion to predict the energies of nanoparticles as a function of shape, size, and internal atomic order. I want to highlight the extendable size of this cluster expansion, which enables simulations on the nanoparticles at experimentally synthesized sizes (nearly 4 – 20 nm[54, 59-61, 63-68]), which is preferable to previous cluster expansions built on fixed shape nanoparticles (no more than 2 nm)[27-28, 69-71]. Moreover, the oxygen reduction reaction (ORR) happens under cell operating conditions instead of in vacuum. Therefore, the cluster expansion built in vacuum condition, are unable to predict the change of structure and properties of nanoparticles as a function of applied potential or oxygen chemical potential. In order to investigate the structural behaviors of experimentally-observed nanoparticles[54, 59-60, 72] in oxidizing conditions, I extended the cluster expansion model to include the metal specific and site-specific correction terms that account for the possible presence of adsorbed atomic oxygen atom (*O) and hydroxyl (*OH) on the surface of nanoparticles. The details of how I calculated these correction terms based on the type of adsorbates, surface metal element, local atomic order near the adsorption site, the applied potential and the chemical potentials are provided in Chapter 4.

With the help of the cluster expansion Hamiltonian on nanoparticles, Monte Carlo simulations can calculate the thermodynamic properties of nanoparticles at the atomic level, which is difficult to do in the experimental measurement in part because of equipment limitations. The examples of predictions enabled by the cluster expansion are as follows. Firstly, the ground state shapes of nanoparticles can be predicted for a given size and alloy composition of a particle. Secondly, composition profiles (composition for each layer) of Pt_3Ni nanoparticles can be predicted to investigate the size effect, and temperature effect. Thirdly, the average site occupancies for nanoparticles can straightforwardly show the preferred sites for Pt/Ni/Mo atoms under different chemical environments. Fourthly, the predicted surface vacancy formation energy of Pt/Ni can be used to better understand the stability of nanoparticle surfaces. Last but not least, provided that the activity and durability of Pt_3Ni have been highly improved due to Mo-doping, it is worth investigating Mo doping effects on the atomic structures and stability under cell operating conditions. All of these predictions can give us insights into the loss of activity and stability of Pt/Ni catalysts after high potential cycles at the atomic level, and help us determine the likely reasons for the highly enhanced stability of Mo-doped Pt_3Ni nanoparticles, and furthermore may enable rational design of alloy catalysts with desired properties.

Although all discussions of cluster expansions in this thesis are based on Pt/Ni binary and Pt/Ni/Mo ternary alloy systems, I anticipate that the two cluster expansion approaches demonstrated in this thesis will provide valuable insights that can be applied in general to the investigation of other similar low-symmetry systems (extended surfaces and nanoparticles). For example, it has been shown that local atomic order can dramatically affect the catalytic properties of Pd-Au alloy surfaces[73], and the cluster expansion approach

definitely can help to study this effect of Pt-Au alloys at atomic level.

1.4 CO_2/CO reduction catalysts: Cu nanowires

Electrochemical reduction of CO_2 and CO to produce hydrocarbons (e.g., CH_4, HCOOH, C_2H_4, C_2H_5OH, and C_2H_6) is one of the candidate processes for a new source of energy that creates a sustainable fuel cycle in which the fossil fuels' waste products (CO_2 and CO) are recycled back into fuel.[74] Among the metal catalysts tested so far, copper (Cu) is one of the most successful catalysts for CO_2/CO reduction with exceptional catalytic activity.[75-76] However, the commercial usage of Cu as catalysts for CO_2/CO reduction has been limited by the relatively high overpotentials (~1 V).[77-78] The strategy to improve Cu electrocatalytic performance and lower (in absolute value) the overpotentials is to tailor the surface morphology of Cu catalysts, such as surface roughness[79-80], crystal facets[81-82], and particle size[83]. Recently, low overpotentials were experimentally observed (~0.4 V) for CO_2/CO reduced to C_1 and C_2 products on Cu catalysts, which have drawn both experimental and theoretical researchers' attention.[79-80, 82, 84]

Here, I present the most recent advances of CO_2/CO reduction. For the CO_2 reduced to CO, in 2012, Li et al.[80] reported that CO_2 can be reduced to CO and HCOOH with current density of 1 mA/cm^2 at overpotentials less than 0.4 V on the Cu catalysts synthesized by reduction of Cu_2O films. In 2015, my collaborators, Chao Wang and David Raciti, reported that highly dense Cu nanowires prepared by electrochemical reduction from CuO nanowires have high activity and selectivity for CO_2 reduction to CO and HCOOH at low overpotentials of 0.3 – 0.4 V.[84] However, only reducing CO_2 to CO is not enough, CO should be further reduced to form hydrocarbons in order to produce environmentally

friendly and renewable energy. Thus, I present some recently reported Cu catalysts with relative low overpotentials and high selectivity for CO reduced to C_1 and C_2 hydrocarbons below. In 2012, Schouten et al.[82] reported low potentials (~ -0.4 V versus RHE) for CO reduction to C_2H_4 on the Cu(100) facet through a CO dimerization mechanism. In 2014, Li el al.[79] reported low potentials (-0.24 – -0.5 V versus RHE) and high selectivity of products (multi-carbon oxygenates with 57% Faraday Efficiency (FE) on Cu nanocatalysts prepared in the same method as the work of Li et al.[80] In 2016, Chao Wang and David Raciti tailored the surface structures of Cu nanowires by controlling the CuO reduction conditions and demonstrated that high percentage of Cu(110) facet may be responsible for the low potentials (-0.2 – -0.35 V versus RHE) and highly selective reduction of CO toward oxygenated C_2 products.[85]

Theoretically, a lot of efforts have been made to formulate the likely mechanisms that can explain the low overpotentials and high selectivity for CO reduction to C_2 products in terms of structure (facet)-property relationship. In the work of Calle-Vallejo et al.[86], a CO-CO coupling mechanism (the formation of surface $OCCO^{\delta-}$ dimer via the direct coupling two CO), where proton-electron transfer is decoupled, was proposed to explain the experimental observation that C_2 species are produced, but C_1 species are suppressed at low overpotential (~ 0.4 V) on the Cu(100) facet.[82, 87] In 2013, Montoya et al.[88] demonstrated that the higher degree of hydrogenation of adsorbed CO (*CO) will give the lower kinetic barriers to C-C coupling and form multi-carbon hydrocarbons: starting from *CO, for two single carbon adsorbates each with one or more H atoms hydrogenated (*CHO, *CH2O), the C-C coupling will be energetically favorable on Cu(211) through the "DFT-backed" nudged elastic band (NEB) calculations.[89-90] In 2015, Montoya et al.[91] used

a charged water layer on both the Cu(111) and Cu(100) surfaces to calculate energy barriers of charged CO dimer ($OCCO^{\delta-}$) formation, identified a previously unreported CO dimer configuration that is stabilized by a charged water layer, and predicted a lower kinetic barrier on Cu(100) than Cu(111), in agreement with the experimental results of higher activity and selectivity on Cu(100) facet for the C_2 products.

In addition to using the cluster expansion approach to investigate Pt/Ni ORR catalysts, in Chapter 5 I performed DFT calculations to study possible reaction pathways for CO_2/CO reduction reaction on the different Cu facets (mainly on close-packed facet Cu(111), and more open facets: Cu(211), Cu(110), and Cu(100)). Together with the experimental characterization of surface structure and electrochemical properties of synthesized Cu nanowires catalysts from my collaborators,[85] I suggest likely explanations for the low overpotentials and high selectivity of C_2 products due to facet effects on the Cu nanowires.

1.5 The scope of this thesis

I will present what I have done during my Ph. D. career in the rest of this thesis. The organization is as follows. In Chapter 2, I present the basic methodology of cluster expansion and Metropolis Monte Carlo simulations. In Chapter 3, cluster expansions built on Pt/Ni-Oxygen/Vacancy 2-dimensinal extended surfaces are developed to investigate the structure-property relationship of Pt-Ni alloy catalysts at the atomic level. This work was published as J. Phys. Chem. C 119, 17735-17747 (2015).[92] In Chapter 4, I extend cluster expansions on extended surfaces to Pt/Ni/Mo 0-dimensinal nanoparticles, which are more realistic in the electro-chemistry environment. The related work of Chapter 4 led to two papers, one published as Science 348, 1230–1234 (2015)[54] and the other[93] submitted for publication. In Chapter 5, I investigate the possible CO_2/CO reduction pathways on the four different Cu crystalline facets (Cu(211), Cu(110), Cu(100) and Cu(111)) by building free energy diagrams, and identify Cu(110) as highly active facet responsible for the observation of low overpotentials and high selective reduction CO toward C_2 products. The preliminary work of CO reduction has been submitted for publication in reference 85. In Chapter 6, I will briefly talk about the future work that may be done related to my Ph.D. research.

Chapter 2

Methodology

2.1 First principles calculations

2.1.1 Density functional theory calculations

Solving Schrödinger's equation is viewed as the fundamental problem of quantum mechanics.[94] However, few problems in quantum mechanics – with time-independent or time-dependent Hamiltonians – can be solved exactly in mathematics, such as single harmonic oscillator. For the low-dimensional systems I am interested in, for example, Pt-Ni surfaces (2-dimension) or nanoparticles (0-dimension), and Cu surfaces (2-dimension), I need to calculate their ground-state energies given specific atomic orders so as to investigate the relationships between their surface structure and catalytic properties. The problem of calculating the ground-state energies of these low-symmetrical systems is to solve a many-body Schrödinger's equation.

The density functional theory (DFT) calculations aim to solve the time-independent Schrödinger's equation, $H\Psi = E\Psi$, which is a many-body problem as expressed in Eq. (2.1):

$$\left[-\frac{\hbar}{2m}\sum_{i=1}^{N}\nabla_i^2+\sum_{i=1}^{N}V(\mathbf{r_i})+\sum_{i=1}^{N}\sum_{j<i}U(\mathbf{r_i},\mathbf{r_j})\right]\Psi=E\Psi\,, \tag{2.1}$$

where m is the electron mass. The three terms inside of summation signs in brackets in Eq. (2.1) are defined as, the kinetic energy of each electron, $-\frac{\hbar}{2m}\nabla_i^2$, the interaction energy between each electron and the collection of all atomic nuclei within the system, $V(\mathbf{r_i})$, and the interaction energy between two distinguishing electrons (i and j), $U\left(\mathbf{r}_i,\mathbf{r}_j\right)$. For the Hamiltonian expression in Eq. (2.1), Ψ is the electronic wave function (the solution to Schrödinger's equation), expressed as $\Psi=\Psi(\mathbf{r}_1,\mathbf{r}_1...,\mathbf{r}_N)$, which is a function of 3N coordinates (three spatial coordinates of each electron for N electrons). E in Eq. (2.1) is the ground state energy of the system. Provided electrons have spins (spin up +1/2 and spin down -1/2), the multi-electrons system (N electrons) is a multi-fermionic system, which satisfies anti-symmetry requirements and consequently the Pauli principle. Thus, the wave function of N electrons, $\Psi=\Psi(\mathbf{r}_1,\mathbf{r}_1...,\mathbf{r}_N)$, can be exactly expressed as a Slater determinant, which is a normalized linear combination of Hartree products.[95] A Hartree product, defined as $\Psi=\Psi_1(\mathbf{r})*\Psi_2(\mathbf{r})*,...,*\Psi_N(\mathbf{r})$, is a product of individual electron wave functions. Here, $\Psi_i(\mathbf{r})$ is the individual wave function for the individual electron i. Without loss of generality, I use a single Hartree product, $\Psi=\Psi_1(\mathbf{r})*\Psi_2(\mathbf{r})*,...,*\Psi_N(\mathbf{r})$, as the approximation of the wave function $\Psi=\Psi(\mathbf{r}_1,\mathbf{r}_1...,\mathbf{r}_N)$.

In this section, I briefly present the basic terms and concepts of density functional theory (DFT) based primarily on the book of Sholl et al.[96] The basic idea of density functional theory (DFT) is rewriting the Hamilton as a functional of electronic density.[97] Density

functional theory is to move from wave functions to electron density when people solve the Schrödinger's equation. The density of electrons is defined as follows,

$$n(\mathbf{r}) = \sum_{i=1}^{N} \Psi_i^*(\mathbf{r})\Psi_i(\mathbf{r}), \tag{2.2}$$

where $\Psi_i(\mathbf{r})$ is the individual wave function for electron *i*. The electron density in Eq. (2.2) is a function of only three coordinates, contains the information that can be derived from the full wave function solution to the Schrödinger's equation, $\Psi = \Psi(\mathbf{r}_1, \mathbf{r}_1 ..., \mathbf{r}_N)$, which is a function of 3N coordinates. Thus, if the Schrödinger's equation can be solved in the form of the electron density instead of the full wave function, the coordinates of the many-body problem will be dramatically reduced from 3N to 3.

Then the problem becomes whether we can find such a solution to the Schrödinger's equation in Eq. (2.1) expressed in the form of electron density $n(\boldsymbol{r})$. The entire field of density functional theory is built on two fundamental mathematical theorems proved by Kohn and Hohenberg[97] and the derivation of a set of equations by Kohn and Sham[14] in 1960s. The first theorem is: "The ground-state energy from Schrödinger's equation is a unique functional of the electron density."[96] The second Hohenberg-Kohn theorem explains an important property of the functional of the electron density: "The electron density that minimizes the energy of the overall functional is the true electron density corresponding to the full solution of the Schrödinger's equation."[96]

Given the two fundamental theorems, Hohenberg and Kohn[97] stated that the energy functional can be written as:

$$E[\{\Psi_i\}] = E_{known}[\{\Psi_i\}] + E_{XC}[\{\Psi_i\}], \tag{2.3}$$

which is in terms of single electron wave functions, $\Psi_i(\mathbf{r})$. Here, $E[\{\Psi_i\}]$ is split into

two parts: $E_{known}[\{\Psi_i\}]$, analytical form and $E_{XC}[\{\Psi_i\}]$, the exchange-correlation functional.

The analytical part $E_{known}[\{\Psi_i\}]$ can be expressed as:

$$E_{known}[\{\Psi_i\}] = -\frac{\hbar}{2m}\sum_i \int \Psi_i^* \nabla^2 \Psi_i d^3\mathbf{r} + \int V(\mathbf{r}) n(\mathbf{r}) d^3\mathbf{r} + e^2 \iint \frac{n(\mathbf{r}) n(\mathbf{r}')}{|\mathbf{r}-\mathbf{r}'|} d^3\mathbf{r} d^3\mathbf{r}' + E_{ion} \quad (2.4)$$

The terms in the right hand side of Eq. (2.4) are, the summation of kinetic energy for each electron ($-\frac{\hbar}{2m}\sum_i \int \Psi_i^* \nabla^2 \Psi_i d^3\mathbf{r}$), the Coulomb interactions between all electrons and the collection of all nuclei ($\int V(\mathbf{r}) n(\mathbf{r}) d^3\mathbf{r}$), the Hartree term ($e^2 \iint \frac{n(\mathbf{r}) n(\mathbf{r}')}{|\mathbf{r}-\mathbf{r}'|} d^3\mathbf{r} d^3\mathbf{r}'$), which is the approximation of the Coulomb interactions between pairs of electrons, and the Coulomb interactions between all pairs of nuclei (E_{ion}). The other term, $E_{XC}[\{\Psi_i\}]$, includes all quantum mechanical effects that have not been included into the known term of $E_{known}[\{\Psi_i\}]$ in Eq. (2.4).

By applying variational calculus to Eq. (2.3) and Eq. (2.4), the Kohn-Sham equations[14] are derived as follows:

$$\left[-\frac{\hbar}{2m} \quad (\mathbf{r}) + V_H(\mathbf{r}) + V_{XC}(\mathbf{r})\right]\Psi_i(\mathbf{r}) = \varepsilon_i \Psi_i(\mathbf{r}). \quad (2.5)$$

As shown in Eq. (2.5), the solutions to Kohn-Sham equations are single electron wave functions $\Psi_i(\mathbf{r})$. On the left hand side of Eq. (2.5), there are three potentials, $V(\mathbf{r})$, $V_H(\mathbf{r})$ and $V_{XC}(\mathbf{r})$. The first one, $V(\mathbf{r})$, represents the interaction between an electron and the

collection of all atomic nuclei. The second one, $V_H(\mathbf{r})$, is called as the Hartree potential and defined as:

$$V_H(\mathbf{r}) = e^2 \int \frac{n(\mathbf{r}')}{|\mathbf{r}-\mathbf{r}'|} d^3\mathbf{r}'. \tag{2.6}$$

The third one, $V_{XC}(\mathbf{r})$, defines the exchange and correlation contributions to Kohn-Sham equations, and can be defined as a "functional derivative" of the exchange-correlation energy:

$$V_{XC}(\mathbf{r}) = \frac{\delta E_{XC}(\mathbf{r})}{\delta n(\mathbf{r})}. \tag{2.7}$$

The algorithm to solve the Kohn-Sham equations is iterative and self-consistent, which is outlined as follows[96]:

1. Define an initial and trial electron density, $n(\mathbf{r})$.
2. Solve the Kohn-Sham equations in Eq. (2.5) defined using the trail electron density in step 1 to determine the single electron wave functions, $\Psi_i(\mathbf{r})$.
3. Calculate the electron density based on the solutions to Kohn-Sham equations from step 2, $n_{\mathrm{KS}}(\mathbf{r}) = \sum_{i=1}^{N} \Psi_i^*(\mathbf{r})\Psi_i(\mathbf{r})$.
4. Compare the calculated electron density in step 3, $n_{\mathrm{KS}}(\mathbf{r})$, with the trail electron density used in solving the Kohn-Sham equations, $n(\mathbf{r})$, defined in step 1. If two of them are the same, then $n_{\mathrm{KS}}(\mathbf{r})$ is the ground-state electron density so that it can be used to compute the total ground-state energy. If two of them are different, then the trail electron density ($n(\mathbf{r})$) in step 1 must be updated in some pre-defined

way. Iterate from step 1 to step 4 until $n_{\mathrm{KS}}(\mathbf{r})$ and $n(\mathbf{r})$ are the same.

2.1.2 Vienna Ab initio Simulation Package (VASP)

All density functional theory (DFT) calculations in this thesis were performed with the Vienna Ab initio Simulation Package (VASP),[15-16, 98-100] in which the Kohn-Sham equations are solved by self-consistent algorithms. The setting of all DFT calculations is as follows unless otherwise noted. The C_GW_new, Cu_pv_GW, H_GW, Mo_pv, Ni, O_GW and Pt_pv_GW PBE projector-augmented wave (PAW)[101] potentials provided with VASP were used to improve the calculation efficiency, and VASP was run with high precision. The revised Perdew-Burke-Ernzerhof (RPBE)[102-103] exchange-correlation functional was used for all calculations. Spin polarization was taken into account in the calculations and the Methfessel–Paxton method[104] of order 2 was employed to determine electron occupancies with a smearing parameter of 0.2 eV. The convergence criteria for the electronic self-consistent iteration and the ionic relaxation loop were set to be 10^{-4} eV and 10^{-3} eV, respectively.

2.2 Cluster expansions

2.2.1 Basic theory of cluster expansions

The cluster expansions are generalized Ising models.[2] The beginning of cluster expansions is in the early of 1950s when Kikuchi developed a "Cluster Variation Method" of approximation for the order-disorder phenomena in 1-dimensional, 2-dimensional and 3-dimensional Ising lattices.[105] In 1984, Sanchez et al.[1] developed a general formalism for the description of configurational cluster functions, which were described in terms of an orthogonal basis in the multidimensional space of discrete spin variables, in multicomponent systems.

Here, I introduce the basic idea of the cluster expansions based primarily on the work of Sanchez et al.[1] Generally, cluster expansions are generalized Ising models, in which the "spin" variables assigned to each site in an Ising model are replaced by "site" variables that each site variable indicates which species (or vacancy) is present at a certain site. To have a better understanding of assigning site variables, the example for a simple A-B binary alloy is shown in Figure 2.1. As illustrated in Figure 2.1(a), each atomic site in the crystal is assigned a site variable, s_j, where $s_j = 1$ means element A is present at the *j*th site, and $s_j = -1$ means element B is present. A straightforward example of a cluster is a nearest-neighbor pair of sites, marked as cluster "**b**" in Figure 2.1(b).

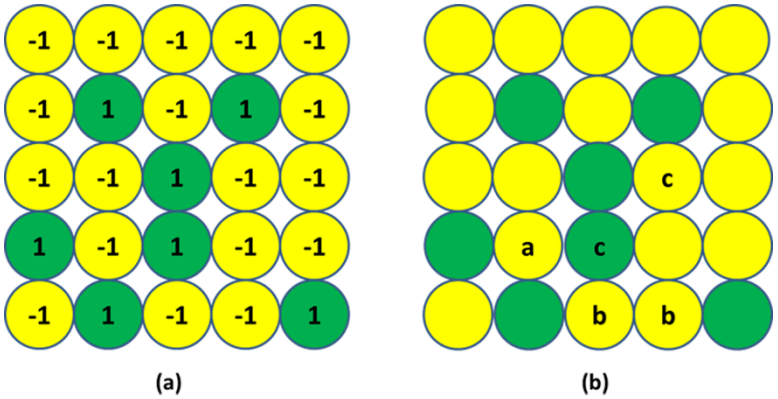

Figure 2.1. An illustration of site variables and clusters of an A-B binary alloy. Green and yellow spheres represent the A and B atoms respectively. (a) How site variables are assigned. A atoms are marked as "1", B atoms are marked as "-1"; (b) Examples of clusters used in a cluster expansion. The one atom marked as "**a**" is a single-site cluster, the two atoms marked as "**b**" are in a nearest-neighbor two-site cluster, and the two atoms marked as "**c**" are in a second-nearest-neighbor two-site cluster.

Generally, an orthogonal single-site basis is defined for each site variable. The expression is shown as follows:

$$\frac{\sum_{s_j}^{N_j} \Theta_b(s_j)\Theta_{b'}(s_j)}{N_j} = \delta_{bb'}, \tag{2.8}$$

where s_j is the site variable for the site labeled as j, and N_j is the number of values that this site variable s_j may take. For example, if the cluster expansions represent an A-B binary alloy bulk lattice, then N_j is equal to 2 ($s_j = 1$ or $s_j = -1$ in Figure 2.1). If the cluster expansions represent the lattice for ABC ternary alloy nanoparticles including the vacuum site, then N_j is equal to 4 (the first, second, and thrid values for A, B, and C metal sites respectively, and the fourth value for the vacuum site). Also, $\Theta_b(s_j)$ is the bth basis function for the jth site, and $\delta_{bb'}$ is the Kronecker delta, where $\delta_{bb'} = 1$ if $b = b'$ and

$\delta_{bb'} = 0$ if $b \neq b'$. Again, taking cluster expansions represent AB binary alloy as an example (Figure 2.1), whose site variable s_j may take on the values of -1 or +1, one set of commonly used single-site basis functions that meets the orthonormal condition in Eq. (2.8) is as follows:

$$\begin{cases} \Theta_0(s_j) = 1 \\ \Theta_1(s_j) = s_j. \end{cases} \tag{2.9}$$

Then for each cluster, $\mathbf{S}$, which contains a certain number of sites in the lattice ($\mathbf{S} = (s_1, s_1, ..., s_n)$, given the number of sites is n), a cluster function is defined. The way to produce a basis of "cluster functions" is to use the tensor product of all single-site basis functions (defined in Eq. (2.9)) corresponding to all single sites that belong to a specific cluster, $\mathbf{S}$. Each cluster function can be denoted as:

$$\Phi_{\mathbf{b}}(\mathbf{s}) = \prod_j \Theta_{b_j}(s_j), \tag{2.10}$$

where $\mathbf{S}$ is the set of all site variables for a certain cluster, and $\mathbf{b}$ is a single vector representing the indices of basis functions defined in Eq. (2.9). b_j stands for the *j*th elements of $\mathbf{b}$ and s_j stands for the site variable at site *j*. Generally, $\Theta_0(s_j) = 1$ when $b_j = 0$ for all site variables, s_j, and the value of cluster function in Eq. (2.10) only depends on the $\Theta_{b_j}(s_j)$, in which $b_j \neq 0$.

As shown in the work of Sanchez et al.[1], the cluster functions defined in Eq. (2.10) must be orthonormal if the underlying single-site basis functions defined in Eq. (2.9) are

orthonormal. For a certain cluster, $\mathbf{s}$, containing a group of sites within lattice, the orthogonality property is as follows:

$$\frac{\sum_{i=1}^{N_{\mathbf{s}}} \Theta_{\mathbf{b}}(\mathbf{s}_i)\Theta_{\mathbf{b}'}(\mathbf{s}_i)}{N_{\mathbf{s}}} = \delta_{\mathbf{bb}'}\,, \tag{2.11}$$

where $\mathbf{s}_i$ is the ith set of possible values for the cluster $\mathbf{s}$, and $N_{\mathbf{s}}$ is the total number of possible values of $\mathbf{s}$. Please pay attention to the different meanings of indices i and j : the index of i in Eq. (2.11), where $\mathbf{s}_i$ stands for ith set of the value of the cluster $\mathbf{s}$ ($\mathbf{s}_i$ is actually a value of "a vector"); and the index of j in Eq. (2.8), Eq. (2.9) and Eq. (2.10), where s_j stands for the site variable of at jth site.

If a property (e.g. formation energy and lattice parameter) of the material can be expressed as a function of the site variables across lattice, $F(\mathbf{s})$, then it also can be expanded exactly as a linear combination of cluster functions:

$$F(\mathbf{s}) = V_0 + \sum_{\mathbf{b}} V_{\mathbf{b}} \Phi_{\mathbf{b}}(\mathbf{s})\,, \tag{2.12}$$

where the unknown coefficients, $V_{\mathbf{b}}$, are known as effective cluster interactions (ECIs), and V_0 is a constant term representing the ECI for the "empty" cluster. The sum is over all cluster functions, where the number of sites in a cluster may range from 1 to all the sites in the material. When all possible clusters are included in the expansion, the expansion in Eq. (2.12) is exact. If there are identically symmetrical clusters within the lattice of cluster expansions, then the expression of cluster expansions can be further reduced to a more general equation due to symmetry,

$$F(\mathbf{s}) = V_0 + \sum_{\alpha} V_{\alpha} \sum_{\mathbf{b} \in \alpha} \Phi_{\mathbf{b}}(\mathbf{s}) \tag{2.13}$$

where α represents an orbit of symmetrically equivalent cluster functions. The property, $F(\mathbf{s})$, expressed as the cluster expansions in this thesis is formation energy. Usually, the value of an extensive property, such as formation energy, could be normalized to the value per unit of material (per unit cell). For such a property, Eq. (2.13) can be rewritten as,

$$\left\langle F(\mathbf{s}) \right\rangle = \left\langle V_0 \right\rangle + \sum_{\alpha} V_{\alpha} m_{\alpha} \left\langle \Phi_{\mathbf{b}}(\mathbf{s}) \right\rangle_{\alpha}, \tag{2.14}$$

where $\left\langle F(\mathbf{s}) \right\rangle$ is the average value of the property per unit formula and $\left\langle \Phi_{\mathbf{b}}(\mathbf{s}) \right\rangle_{\alpha}$ is the average value of all cluster functions in orbit α, $\mathbf{b}$ is a cluster function belonging to α ($\mathbf{b} \in \alpha$), and m_{α} is the number of cluster functions in orbit α per unit formula. However, we should be careful when the property, $F(\mathbf{s})$, is an intensive value (such as averaged *d*-band center, and fermi energy), which should not be normalized.

2.2.2 Bayesian approach to cluster expansions

In practice, the ECIs for clusters that contain a large number of sites or sites that are far apart from each other are usually negligible, allowing for the expansion to be truncated to a sum with a finite number of ECIs with little loss of accuracy. The remaining ECIs are then fit to a set of training data of energies, which I generated using density functional theory (DFT)[14] calculations. In low symmetry systems, such as extended surfaces and nanoparticles, there are typically far more distinct and significant ECIs than in a 3-dimensional bulk systems due to the loss of periodicity. For example, two congruent

clusters in bulk systems are symmetrically equivalent to each other; but two congruent clusters in the extended surfaces may be not symmetrically equivalent to each other. The definition of congruent clusters is: if there must be a way to map the sites of one cluster onto the sites of another that preserves all distance and angles between sites, then the two clusters are congruent clusters. As the simple 2-dimensional square lattice for an extended surface shows (Figure 2.2), clusters "**a**" and "**b**" are symmetrically equivalent to each other, but clusters "**a**" and "**c**" are not equivalent to each other (even though they are congruent) because of their different distances to the surface.

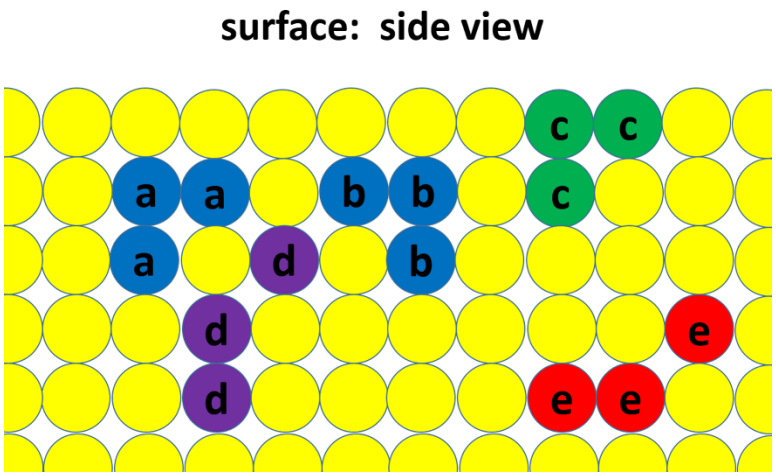

Figure 2.2. The side view of the surface on a simple square lattice: an illustration of the difference between symmetrical and congruent clusters. The triple cluster of sites marked with "**a**" is symmetrically equivalent to the one marked with "**b**"; but the cluster "**a**" is not equivalent to the cluster marked with "**c**". However, cluster "**a**" will be symmetrically equivalent to cluster "**c**" in a corresponding 3-dimensional bulk lattice. Cluster "**a**" and "**c**" are congruent, so as "**b**" and "**c**". Cluster "**d**" and cluster "**e**" are also congruent but not symmetrically equivalent.

Thus, because they have a larger number of significant distinct clusters, it is much more computationally expensive to fit the ECIs of cluster expansions built on low symmetrical systems (e.g., extended surfaces and nanoparticles) than 3-dimensinal bulk systems for a

given level of accuracy. Here, for cluster expansions built on low symmetric systems, I used a Bayesian approach developed by Mueller et al.[21] to fit the ECIs with low computational cost and high accuracy for a given set of training data, instead of least-squares fit for each selected group of cluster functions. I will give a brief summary of the application of Bayesian approach to cluster expansions based on the work of Mueller el al.[21] I also will compare the advantages of Bayesian approach with common used least-square fit method in this section.

Firstly, I would like to introduce the notations that are used in the Bayesian approach to cluster expansions.

(i) $\mathbf{v}$: the set of optimal values for ECIs, which is defined over all possible ECI values after truncation.

I express the training data as:

(ii) $\mathbf{y}$: a vector of output values, the ith element of $\mathbf{y}$ is the property value (formation energy) for the ith structure in the training set.

(iii) $\mathbf{X}$: a matrix of input values, the elements of X are given by $X_{i\alpha} = m_\alpha \left\langle \Phi(\mathbf{s}_i) \right\rangle_\alpha$. Here the subscript, i, corresponds to the ith element, and subscript, α, corresponds to the index for cluster, the αth cluster. $\left\langle \Phi(\mathbf{s}_i) \right\rangle_\alpha$ is defined in Eq. (2.14).

Then the probability density of optimal ECIs ($\mathbf{v}$) is the conditional probability distribution, $P(\mathbf{v}|\mathbf{X}, \mathbf{y})$, since the training data ($\mathbf{y}$ and $\mathbf{X}$) has been known for a given training set. The key to Bayesian approach is to use Bayes's theorem,[106] together with physical insights, to determine the ECIs ($\mathbf{v}$) that maximize $P(\mathbf{v}|\mathbf{X}, \mathbf{y})$. In the context of cluster expansion, Bayes' theorem can be expressed as

$$P(\mathbf{v}|\mathbf{X},\mathbf{y}) = \frac{P(\mathbf{y}|\mathbf{v},\mathbf{X})P(\mathbf{v}|\mathbf{X})}{P(\mathbf{y}|\mathbf{X})}. \tag{2.15}$$

The key to this application of Bayes' theorem is to build the prior probability distribution, $P(\mathbf{v}|\mathbf{X})$, which is an educated guess of the likelihood of ECI values before we have calculated property values for the training data. In the process of building $P(\mathbf{v}|\mathbf{X})$, two examples of physical insights incorporated into the nature of the ECIs are: 1) "the greater the number of sites in the cluster, and the greater the distance between sites in a cluster, the smaller the ECI value should be."[21] 2) "ECIs for similar clusters should have similar values."[21] Also, the covariance between two distinct clusters should be taken into account, especially for those pairs of similar clusters, such as congruent clusters demonstrated in Figure 2.2.

The prior chosen for Bayesian approach is a multivariate Gaussian prior distribution over possible ECI values. The inverse of the covariance matrix for the prior, Λ, was diagonal, with elements of orbit regularization parameter $\lambda_{\alpha\alpha}$ and coupled regularization parameter $\lambda_{\alpha\beta}$ given by

$$\lambda_{\alpha\alpha} = \begin{cases} 0 & \text{for } n_\alpha = 0 \\ \lambda_1 & \text{for } n_\alpha = 1 \\ \lambda_2 (1 + r_\alpha)^{\lambda_3} e^{\lambda_4 n_\alpha} & \text{for } n_\alpha > 1 \end{cases}, \tag{2.16}$$

$$\lambda_{\alpha\beta} = \begin{cases} 0 & \text{if } \alpha \text{ and } \beta \text{ are not congruent} \\ \lambda_5 \lambda_{\alpha\alpha} & \text{if } \alpha \text{ and } \beta \text{ are congruent} \end{cases}, \tag{2.17}$$

where n_α is the number of sites in cluster function α, r_α is the maximum distance between sites, and the parameters λ_1, λ_2, λ_3, λ_4, and λ_5 were determined by using a conjugate gradient algorithm to minimize the leave-one-out cross validation (LOO CV) score, an estimate of prediction error.[18] The details of generating $\lambda_{\alpha\alpha}$ and $\lambda_{\alpha\beta}$ according to specific cluster expansions built on different systems (could be 3-demensional bulk, extended surfaces, 1-dimensional nanowire, and nanoparticles) are provided in the work of Mueller et al.[21]

Moreover, I would like to highlight the advantages of Bayesian approach to fit cluster expansions against the commonly used standard least-squares fit approach. Firstly, for least-squares fit, it is necessary to manually select "important" clusters, and it is vulnerable to overfitting.[18] For Bayesian approach, it is actually machine learning algorithm that automatically determines the importance of clusters by fitting the values of ECIs (given selected prior shape of probability distributions in Eq. (2.16) and Eq. (2.17)), and it is robust again overfitting.[21] Secondly, least-square fit needs at least as many structures in the training set as the number of unknown ECIs to be fitted (In practice, usually roughly twice as many training structures are generated).[3, 5, 18, 107-108] Together with the fact that it is much more computationally expensive to DFT-calculate the property values of low-symmetric systems, such as surfaces and nanoparticles, than 3-dimensional bulk systems, it is prohibitively expensive to generate a sufficient training set for low-symmetric systems if lease-square fit is used. Bayesian approach, however, which allows for an arbitrarily larger number of ECIs to be fitted in the cluster expansions, regardless of the size of training set, can solve the problem.

2.3 Monte Carlo simulations

2.3.1 Metropolis Monte Carlo simulations

Based on an Ising model, magnetic properties of different types of magnetic materials can be modeled through Metropolis Monte Carlo simulations at a lattice.[109] In this thesis, the Pt/Ni/Mo-O systems, on which that I would like to investigate the structure-properties relationships, are also lattices, which are similar to an Ising model with fixed sites for a given lattice. Since cluster expansions are generalized Ising model, it is straightforward for me to choose Monte Carlo simulations based on cluster expansions Hamiltonian to advance my research on Pt_3Ni alloy catalysts.

For Pt/Ni/Mo-Oxygen lattices, each site can be occupied by Pt, Ni, Mo, O or Vacancy. The phase space of this system with N atoms can be described by the atomic coordinates for all sites, $\mathbf{r}^N = (\mathbf{r}_1, \mathbf{r}_2, \ldots, \mathbf{r}_N)$. Then according to ensemble theory, the thermodynamic average of an observable variable A for the system can be denoted as:

$$\langle A \rangle = \frac{\int A(\mathbf{r}^N)\rho(\mathbf{r}^N)d\mathbf{r}^N}{\int \rho(\mathbf{r}^N)d\mathbf{r}^N}, \tag{2.18}$$

where $\rho(\mathbf{r}^N)$ is the density distribution for phase space. Without loss of generality, in this subsection I assume that the density distribution follows a Boltzmann distribution: $\rho(\mathbf{r}^N) = \exp(-\frac{H(\mathbf{r}^N)}{kT})$. $H(\mathbf{r}^N)$ is the value of Hamiltonian for the system. The sum is over all phase space.

The Hamiltonian in Eq. (2.18) is the cluster expansion Hamiltonian (energy) for an interested system in the context of this thesis. With the help of cluster expansions, I can accurately and rapidly predict the energies (formation energies) of a given atomic order (configuration) of the Pt/Ni/Mo-Oxygen lattice. This benefit of cluster expansions makes it possible to calculate the thermodynamic averages (such as energy, site occupancy, vacancy formation energy, and so on) using Metropolis algorithm.[109] According to Metropolis algorithm, the system is randomly sampled according to its probability distribution of states:

$$P \propto \exp(-\frac{E(\mathbf{s})}{kT}), \tag{2.19}$$

where $\mathbf{s}$ stands for all site variables in lattice. $E(\mathbf{s})$ is the total energy that can be predicted by cluster expansions.

The simplified Metropolis algorithm (In this version of the algorithm, I assume that the probability density follows a Boltzmann distribution) is listed as follows:[110]

(i) Calculate the current energy of system, E_0, based on cluster expansion Hamiltonian of the current configuration.

(ii) Randomly create an event by generating a new configuration according to the limitations of a specific ensemble of the system, and calculate the new system energy, E_1.

(iii) Calculate the value of acceptance ratio: $r = \exp(-\frac{E_1 - E_0}{kT})$.

(iv) If the ratio $r > 1$, (The new configuration has a lower energy than the current one, which means the new one is energy favorable.), then accept the event, and the system is updated to the new configuration.

If $r \leq 1$, (The new configuration has a higher energy than the current one, which means the new one is not energy favorable.), then generate a uniformly distributed random variable ξ. If $\xi < r$, then accept the event and update the configuration; if $\xi \geq r$, deny the event, remain the system at the current configuration (In other words, the system is updated to its current configuration without any change).

Totally, the probability of acceptance will be:

$$P(\text{accept event}) = \min(1, \exp(-\frac{E_1 - E_0}{kT})), \tag{2.20}$$

The number of iterations of Monte Carlo simulations, n, should be large enough, so that the Metropolis algorithm can find the global minimum. After trying different values of n, I found that $n = (100 \sim 1000) \times N$, where N is the total number of sites within the unit cell of cluster expansions, gave me well-converged calculations. Thus I set n as $n = (100 \sim 1000) \times N$ for all Metropolis Monte Carlo simulations in this thesis. When calculating the ensemble average, it is necessary to include all iterations of Metropolis Monte Carlo simulations. For the iterations that the randomly generated configurations are not accepted, the energy should be set as the energy of the most recently accepted configuration (the "current configuration" defined in Metropolis algorithm above). For example, if there are n iterations and n random configurations are created, even though

only M of them are accepted, the ensemble average still will be averaged by n (some configurations will be counted multiple times):

$$\langle E \rangle = \frac{1}{n} \sum_{1}^{n} E_i \tag{2.21}$$

The way to generate a random event depends on the types of system ensembles. The canonical ensemble has constant values of N (number of sites), V (volume), and T (temperature). For the canonical ensemble, an event is created by randomly choosing two sites within the lattice and the two occupied species (The species can be vacancy) are swapped with each other. Grand canonical ensemble has constant values of μ (chemical potential), V (volume), and T (temperature). For grand canonical ensemble, a random event is created like this: one site is randomly selected, then a species will be randomly chosen from a set of possible species and distributed to this site. Moreover, I can define a "mix-ensemble" according to the special conditions of the interested system, which is a mixture ensemble having two or more than two ensembles for different phases of the system. This kind of mix-ensemble can be valuable to investigate the interface between two phases. For example, if I would like to investigate the oxygen coverage under the different oxygen partial pressure on the surface of Pt/Ni slabs with a fixed 75% Pt composition, I can build a mix-ensemble. Within this mix-ensemble, the Pt_3Ni surface slab will be canonical ensemble (Pt/Ni is the pair of species), and the surface monolayer of oxygen/vacancy will be grand canonical ensemble (O/vacancy is the pair of species).

2.3.2 Implementation of Monte Carlo simulations

In the subsection, I would like to highlight some strategies that I used for implementation of Monte Carlo simulations.

Firstly, after successfully building and fitting cluster expansion, the property (Here, the property is the formation energy) of interest can be accurately and rapidly predicted as a function of atomic order, which enables the Monte Carlo simulations on the Pt-Ni extended surfaces and nanoparticles. Knowing the characteristics of the equation of cluster expansions (Eq. (2.12)) can help us even speed up the Monte Carlo simulations further. In each step of Metropolis Monte Carlo simulations, each randomly created event only involves one site (where the current occupied species is replaced by another species in grand canonical ensemble) or two sites (where the occupied species in the two randomly selected sites are swapped with each other in canonical ensemble). Only clusters that contain the involved sites contribute to the change of the formation energy. Thus, it is much faster to directly calculate the formation energy change by only accounting for the involved clusters than calculating the formation energies of entire system before and after the random event triggered, then doing subtraction to get the energy difference. Let me take the prediction of oxygen binding energy based on cluster expansions of Pt/Ni surfaces as an example to mathematically demonstrate the previous argument.

In a binary cluster expansion (in which site variable may take values -1 or +1 so as the basis functions, discussed in section of 2.2), the energy of the slab is given by the following expression:

$$E = \sum_{clusters} V_{cluster} \prod_{i \in cluster} s_i \,. \tag{2.22}$$

Select a single site to be the oxygen binding site, which I will label site j. The energy can then be divided into two terms:

$$E = \sum_{NoOclusters} V_{NoOcluster} \prod_{i \in NoOcluster} s_i + \sum_{Oclusters} V_{Ocluster} \prod_{i \in Ocluster} s_i \,. \tag{2.23}$$

Here, $NoOclusters$ are the clusters that don't contain site j, and $Oclusters$ are clusters that do contain site j. The site variable for site j, s_j, has a value of +1 if a vacancy is present and -1 if an oxygen atom is present. I can therefore write energy expressions for a clean slab and for a slab with a single atomic oxygen adsorbed at the O site, s_j, as:

$$E_{cleanslab} = \sum_{NoOclusters} V_{NoOcluster} \prod_{i \in NoOcluster} s_i + \sum_{Oclusters} V_{Ocluster} \prod_{i \in Ocluster, i \neq j} s_i \,, \tag{2.24}$$

$$E_{Oslab} = \sum_{NoOclusters} V_{NoOcluster} \prod_{i \in NoOcluster} s_i - \sum_{Oclusters} V_{Ocluster} \prod_{i \in Ocluster, i \neq j} s_i \,. \tag{2.25}$$

So the oxygen binding energy (E_{Obind}) is given by:

$$E_{Obind} = E_{OSlab} - E_{cleanslab} = -2 \sum_{Oclusters} V_{Ocluster} \prod_{i \in Ocluster, i \neq j} s_i \,. \tag{2.26}$$

Thus, only the clusters that contain O binding site, s_j, contribute to the strength of predicted oxygen binding energy, E_{Obind}. Here, I want to point that there is a constant shift ($\mathrm{E_{DFT}(H_2) - E_{DFT}(H_2O)}$) between E_{Obind} in Eq. (2.26) and ΔE_O in Eq. (1.3) due to the different choices of reference states.

Secondly, Monte Carlo simulations are usually used to search for ground state by finding the global minimum of energy ($E(\mathbf{s})$ in Eq. (2.19)). I also can use Monte Carlo simulations to search for metastable structures by finding minimum of other properties, such as oxygen binding energy (ΔE_O) and computationally predicted ORR current ($\langle I \rangle$, which will be

defined in Chapter 3) as long as I replace the $E(\mathbf{s})$ with other properties (such as ΔE_O, $\langle I \rangle$, and so on) in Eq. (2.19). For example, in Chapter 3, I use Monte Carlo simulations to search for Pt_3Ni slab surfaces that have optimal predicted ORR average current, $\langle I \rangle$, under given constrains: fixed lattice, fixed Pt-skin (the first layer is pure Pt), and fixed overall Pt composition (75% Pt).

Thirdly, for the purpose of investigating the structure-property relationships on the Pt-Ni surfaces and nanoparticles, the information of the average site occupancy on each site is very useful when I want to know the predicted composition of each layer (or each site). For instance, if a certain site can be occupied by Pt, Ni, or Mo, then the average occupancy of Pt, Ni, or Mo on this site will be recorded as the Metropolis Monte Carlo simulations run through all iteration steps. With this average occupancy information, I can identify and visualize the atomic orders of surface structures under thermodynamically stable or metastable states at atomic level.

Fourthly, I want to mention the implementation of different sizes of Pt-Ni surfaces or Pt-Ni nanoparticles. For the Pt-Ni surfaces, the primitive cell is 1×1×1(111) slab, which can be extended in the plane parallel to the surface (2 dimensionally extendable). Some examples of the super cell of surfaces are 2×2×1(111), 6×6×1(111), and 12×12×1(111). For the nanoparticles, the primitive cell is a 3-dimensional fcc cell, which can be extended to super cell in all three spatial directions. And the boundary of nanoparticles is determined by the occupancy of vacancy in the sites of super cell. It is the reason that my cluster expansion built on nanoparticle is a function of nanoparticle size and shape.

2.4 Oxygen chemical potential

As discussed in subsection 1.2, I will use ΔE_O as a descriptor to investigate the ORR activity of Pt-Ni catalysts. It is critically important that DFT-calculated energies of structures with adsorbed oxygen (e.g. $E_{DFT}(\text{slab+*O})$ in Eq. (1.3)) are accurate. However, the fact is well known that DFT can have problems getting the relative energy of molecular oxygen (O_2(g)) correct compared with experimental data when the generalized gradient approximation (GGA)[111] or local density approximation (LDA)[14] is used.[112-114] Thus, a correction term of O_2(g) is needed for DFT-calculated structures containing adsorbed oxygen. In this section, I calculate this correction terms in the form of reference chemical potential of O_2(g), $\mu_{P_0,T}(O_2)$, as follows.

The chemical potential of molecular oxygen as a function of partial pressure P was calculated using the ideal gas approximation:

$$\mu_{P,T}(O_2) = \mu_{P_0,T}(O_2) + k_B T \ln\left(\frac{P}{P_0}\right), \tag{2.27}$$

where $\mu_{P_0,T}(O_2)$ is a reference chemical potential. To determine an effective value for $\mu_{P_0,T}(O_2)$, I used a method similar to that of Wang et al.[115], in which the effective reference potential for O_2 is fit to experimental data. The reference chemical potential for O_2 was calculated by averaging the following expression over the seven binary oxides shown in Figure 2.3:

$$\frac{2}{y}\left[E_{DFT}\left(M_xO_y\right)-E_{DFT}\left(M_x\right)-\Delta G_{P_0,T}\left(M_xO_y\right)\right], \tag{2.28}$$

where E_{DFT} indicates a DFT-calculated energy and $\Delta G_{P_0,T}\left(M_xO_y\right)$ is the experimental Gibbs free energy of formation under standard conditions. All DFT calculations were done using the RPBE functional, and the experimental enthalpy, entropy, and free energies under standard conditions were obtained from the NIST-JANAF tables.[116] The reference chemical potential for O_2, including the entropy contribution of molecular O_2, was calculated to be $\mu_{P_0,T}=1.376\,eV$, which is the difference between the intercepts of the linear fit of DFT-calculated formation energy and the experimental Gibbs free energy of formation (Figure 2.3).

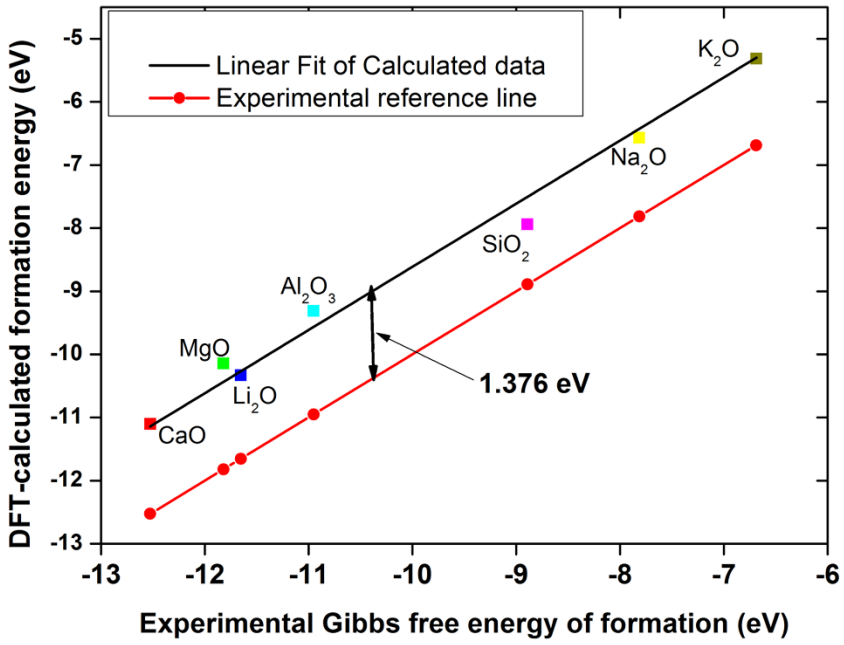

Figure 2.3. DFT-calculated formation energy of non-transitional metal oxides (per O_2 in the reaction) in the GGA approximation as a function of experimental Gibbs free energy of formation. The red line is the experimental reference line, and the solid black line is the best linear fit for the DFT-calculated data of non-transitional metals.

Chapter 3

Cluster expansion approach on Pt/Ni extended surfaces

3.1 Introduction of Pt_3Ni catalysts for ORR

As introduced in Chapter 1, the proton exchange membrane fuel cells (PEMFC) are a promising technology to enable reduced consumption of fossil fuels, but the economic viability of these fuel cells is limited by the sluggish kinetics of the oxygen reduction reaction (ORR) at the cathode. Pt and Pt-based binary alloys are among the most successful catalysts for this reaction. Their catalytic properties have been investigated extensively by experimental[34-35, 38, 43, 45, 65, 117] and computational[46-51] methods. Recent experimental and theoretical research has shown that Pt_3Ni alloys have a much higher ORR activity than pure Pt.[50, 52-54]

Despite their high activity and reduced cost, the practical use of Pt_3Ni catalysts is limited

by their durability under cell operating conditions. Ni atoms located at the near-surface layers of catalysts are not stable in acid medium and tend to dissolve into solution, leaving the Pt atoms behind to form a Pt-skeleton structure.[48, 65, 118] Pt–skin surfaces are thought to stabilize the alloy catalysts in the acid environment. According to the work of Wang et al.[61], a multilayer Pt-skin structure is relatively stable compared to Pt-skeleton surfaces formed from Ni dissolution from the surface and sub-surface layers. It is therefore possible to enhance the stability of $Pt_3Ni(111)$ alloys by modifying their surface structure, but to rationally design new surfaces it is necessary to consider how such modifications may affect catalytic activity. Similarly, it is important to understand how surface segregation and structure are driven by the chemical environment.

In previous computational studies of ORR activity on Pt-Ni surfaces, researchers have constructed hypothetical alloy surfaces by varying the Pt compositions of each atomic layer within small unit cells (usually 2×2(111)). Examples of these surfaces include a surface that retains bulk Pt_3Ni stoichiometry with pure Pt in the first layer, 50% Ni and 50% Pt in the second layer and 25% Ni and 75% Pt in the remaining layers;[48, 50, 119-122] a surface with a monolayer Pt skin on a Pt_3Ni substrate;[51, 123-125] a surface with a monolayer Pt skin on a Ni substrate;[126] and a surface with subsurface Ni (PtNiPt).[51, 124, 127-129] Experimentally, atomic-scale Pt_3Ni near-surface structures are difficult to fully characterize due to sub-surface disorder, off-stoichiometry, and the response of surface structures to different electrochemical environments. Thus it is not clear that the simple model surfaces having been evaluated computationally are representative of real-life catalysts.

To better understand the interplay between surface structure, chemical environment, and catalytic activity on $Pt_3Ni(111)$ surfaces, I have built a detailed computational model that

is able to rapidly and accurately calculate the energies of $Pt_3Ni(111)$ surfaces with up to a monolayer of adsorbed oxygen atoms as a function of atomic order. The foundation of my model is the cluster expansion approach, which allows us to rapidly screen through possible atomic structures on larger extended surfaces (such as 12×12(111) unit cells) that have not been computationally investigated. The accuracy of these calculations is close to that of density functional theory (DFT),[14, 97] with dramatically reduced computational expense. With this approach, I am able to determine the thermodynamically stable near-surface structures at different temperatures and chemical potentials (or near-surface compositions) of Ni, Pt, and adsorbed O. Moreover, I am able to investigate how the atomic order of $Pt_3Ni(111)$ surfaces affects the binding energies of adsorbed oxygen, which has been shown to be an useful descriptor of the ORR activity of the surface.[55-56] Taking this relationship into account, my model enables the rational design of alloy surfaces with optimal ORR activity.

3.2 Building cluster expansions for extended surfaces

To predict the interaction between near-surface atomic order and adsorbed species (*O and *OH) on the surface of Pt_3Ni catalysts, I generated a cluster expansion for the $Pt_3Ni(111)$ 2-dimensonal extended surfaces with up to a monolayer of adsorbed atomic oxygen.

3.2.1 Details of DFT calculations

All density functional theory (DFT) calculations were performed with the Vienna Ab initio Simulation Package (VASP),[15-16, 98-100] in which the Kohn-Sham equations are solved by self-consistent algorithms. The Ni, Pt_pv_GW, and O_GW PBE projector-augmented wave (PAW)[101] potentials provided with VASP were used to improve the calculation efficiency, and VASP was run with high precision. The Brillouin zone was sampled with an 12×12×1 Monkhorst-Pack[130] k-point mesh for my 2×2 (111) cell calculations and scaled appropriately for larger unit cells. The revised Perdew-Burke-Ernzerhof (RPBE)[102-103] exchange-correlation functional was used for all calculations. Spin polarization was taken into account in the calculations and the Methfessel–Paxton method[104] of order 2 was employed to determine electron occupancies with a smearing parameter of 0.2 eV. The convergence criteria for the electronic self-consistent iteration and the ionic relaxation loop were set to be 10^{-4} eV and 10^{-3} eV, respectively.

3.2.2 Slab convergence

The first step of building the cluster expansions for Pt_3Ni extended surface is to build a model structure to mimic the surface of Pt_3Ni catalysts. Since the surface is a two-dimensional system, a 2×2 (111) unit cell is employed as slab model. As illustrated in Figure 3.1 and Figure 3.2, the Pt/Ni(111) surfaces were represented by slabs with the lattice constant fixed to that of bulk Pt_3Ni, which I calculated to be 3.90 Å. In order to make the surface structures well converged to reproduce the surface properties, I did some convergence tests of DFT calculations to optimize the slab thickness and spacing between two slabs. Firstly, I fixed the slab thickness as 6 layers of metal atoms, and increased spacing between slabs from 6 Å to 100 Å, then calculated the surface energies of Pt_3Ni surface structures based on Eq. (3.1),

$$E_{surf} = \frac{E_{slab}^{DFT} - \frac{N_{slab}}{N_{bulk}} * E_{bulk}^{DFT}}{2 * A}, \tag{3.1}$$

where E_{slab}^{DFT} is the DFT energy of per unit cell of Pt_3Ni slab, E_{bulk}^{DFT} is the energy of per unit cell of the Pt_3Ni bulk crystal, N_{slab} is the number of atoms per unit cell of the slab, N_{bulk} is the number of atoms per unit cell of the bulk crystal, and A is the surface area of the slab. For each slab, I have two surfaces and they are of the same type, which is reflected by the number 2 in the denominator.

The criterion for the convergence of surface energies of slab structures is set to 1.0 meV/Å^2. The 6-layer slab with spacing equal to 20 Å is shown in Figure 3.1(b). From Table

3.1, we can see that spacing convergence has been reached at a distance of less than 12 Å. After making a compromise between having enough spacing to add adsorbates and reducing computational expense (because larger spacing means larger simulation cells and higher computational expense), I choose 20 Å, which is equivalent to 9 atomic layers, as the spacing between two slabs.

For the convergence of slab thickness, after getting spacing between slabs converged, I set the spacing as 20 Å, and increased slab thickness from 3 to 20 layers of atoms to optimize it. The 20 Å – vacuum slabs with 3-layer, 6-layer, 9-layer, and 12-layer are shown in Figure 3.1. As illustrated in Table 3.2, slab thickness higher than 6 layers will give us well converged surface energies.

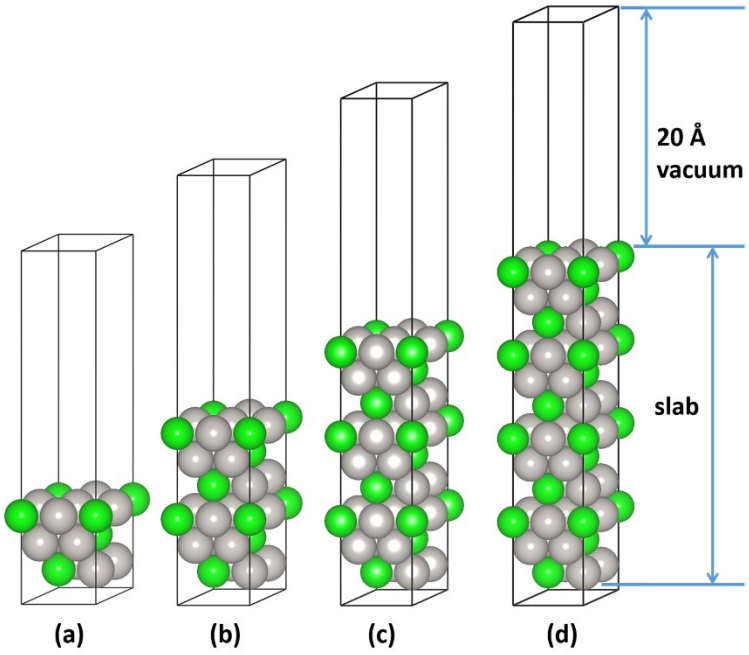

Figure 3.1. Pt_3Ni slab models used for slab and spacing convergence test of periodic DFT calculations, which are created from bulk Pt_3Ni alloys with the same 75% Pt composition for each layer. The structures are composed of a varying-layer slab and a 20 Å vacuum spacing. (a) 3-layer slab; (b) 6-layer slab; (c) 9-layer slab; (d) 12-layer slab. Gray and green spheres represent the Pt and Ni atoms, respectively. Atomic-scale structural images were generated using VESTA.[131]

Table 3.1. Calculated surface energies for slabs with 6-layer slab and increasing vacuum spacing.

Spacing between slabs	slab	energy	surface energy
Å	layer	eV	meV/Å^2
6	6	-138.058	647.14945
12	6	-138.05646	647.34195
18	6	-138.05656	647.32945
20	6	-138.05652	647.33445
25	6	-138.05633	647.3582
40	6	-138.05689	647.2882
60	6	-138.05703	647.2707
80	6	-138.05646	647.3420
100	6	-138.05726	647.24195

Table 3.2. Calculated surface energies for slabs with 20 Å vacuum spacing and increasing slab thickness.

Spacing between slabs	slab	energy	surface energy
Å	layer	eV	meV/Å^2
20	3	-66.270616	668.37273
20	6	-138.05652	647.33445
20	9	-209.67306	647.46668
20	12	-281.28567	648.09015
20	16	-352.90019	648.47488
20	20	-424.516	648.69835

As slabs thicker than 6-layer can give us well-convergence surface energy. If I have taken into account experimental evidence indicating that the Pt composition of the outmost 3 layers for the $Pt_3Ni(111)$ surface differs from that of the bulk material,[53] it is reasonable to choose a slab thickness of 9 layers. The use of nine layers allows for two surface regions of 3 layers each with a "bulk" region of three layers separating the two. Thus, unit cells consisting of a 9-layer slab and a 9 equivalent layers of vacuum spacing (about 20 Å)

between slabs were employed for all the slab models for cluster expansions of Pt_3Ni extended surfaces, as shown in Figure 3.2.

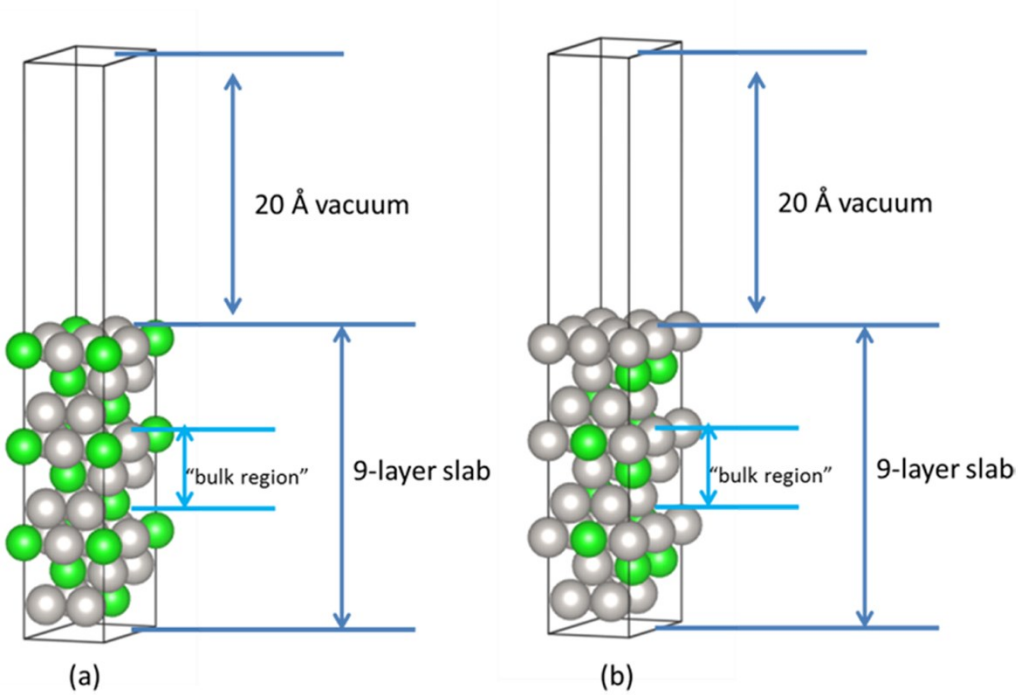

Figure 3.2. Slab model used for periodic DFT calculations. The structure is composed of a 9-layer slab and a 20 Å vacuum spacing. (a) A sample structure created from bulk Pt_3Ni alloys with the same Pt composition for each layer; (b) A first layer Pt-skin structure with 50% Pt in second layer and 75% Pt in the third, fourth and fifth layers. Gray and green spheres represent the Pt and Ni atoms, respectively.

3.2.3 Details of building cluster expansions

The cluster expansion of 9-layer Pt/Ni-Vacancy/Oxygen slab contains two groups of sites (Figure 3.3). The first group contains the sites for Pt/Ni atoms, where $s_j = 1$ for Pt, and $s_j = -1$ for Ni; another group contains the sites for vacancy/O, where $s_j = 1$ for a vacancy, and $s_j = -1$ for O.

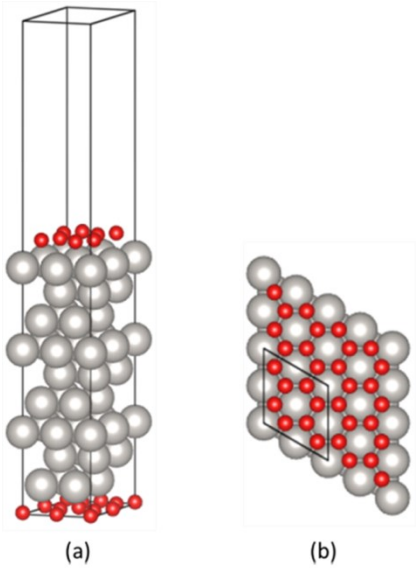

Figure 3.3. Pt/Ni(111) surface model with an adsorbed oxygen monolayer for cluster expansions. (a) side view of a 2×2 (111) unit cell; (b) top view of a 4×4 (111) unit cell. The gray spheres can be occupied by either Pt or Ni, and the red spheres in the hollow sites (fcc and hcp) on the surface can be occupied by either vacancy or oxygen.

The training set used to fit the cluster expansion consisted of an initial set of 50 structures selected to sample configuration space in a way to minimize the variance in the predicted property values, as described in Mueller et al.[20-21] The remaining structures were added every time the energy of a different structure, such as a predicted ground-state structure,

was calculated with DFT, resulting in 260 total structures in the training set. The range of Pt composition with respect to the summation of Pt atoms and Ni atoms for all structures in the training set is between 50% Pt and 100% Pt (pure Pt slab). Within the total 260 structures, there are 113 Pt-Ni slab without atomic oxygen coverage (clean slabs), 3 slabs with 1/32 ML oxygen coverage, 2 slabs with 1/24 ML oxygen coverage, 4 slab with 1/14ML oxygen coverage, 12 slabs with 1/12 ML oxygen coverage, 6 slab with 1/10 ML oxygen coverage, 76 slabs with 1/8 ML oxygen coverage, 6 slabs with 1/6 ML oxygen coverage, 2 slabs with 1/5 ML oxygen coverage, 16 slab with 1/4 ML oxygen coverage, 5 slabs with 1/3 ML oxygen coverage, 8 slabs with 0.375 ML oxygen coverage, 2 slabs with 0.4 ML oxygen coverage, and 5 slabs with 0.5 ML oxygen coverage.

Pt/Ni-Oxygen slabs that experienced significant reconstruction upon relaxation, defined as a Pt/Ni atom traveling more than 75% the nearest-neighbor distance from its initial site or the formation of Oxygen-Oxygen bonds on the Pt/Ni surfaces, were excluded. The excluded slabs were those that have two adsorbed atomic oxygens on nearest-neighboring hcp and fcc sites on Pt/Ni slab surfaces, which will result in the formation of Oxygen-Oxygen bond and the adsorbates are not atomic oxygen anymore. To reduce the prediction error of the cluster expansion, the pure Pt slab was included twice in the training set.[20]

The input training data of the cluster expansions is formation energy of training set slabs, $FE_{DFT}\left(Pt_xNi_yO_z\right)$, instead of energy, $E_{DFT}\left(Pt_xNi_yO_z\right)$. So the cluster expansion Hamiltonian is formation energy of Pt/Ni-Oxygen slabs. The formation energy is defined as:

$$\begin{aligned} FE_{DFT}\left(Pt_xNi_yO_z\right) = & E_{DFT}\left(Pt_xNi_yO_z\right) - x*E_{DFT}\left(bulk\left(Pt\right)\right) \\ & - y*E_{DFT}\left(bulk\left(Ni\right)\right) - \frac{z}{2}*E_{DFT}\left(O_2\left(g\right)\right) \end{aligned}, \tag{3.2}$$

where the subscribe DFT means the values are calculated from DFT. $E_{DFT}\left(Pt_xNi_yO_z\right)$ is the DFT-calculated slab energy; $E_{DFT}\left(\text{bulk}\left(Pt\right)\right)$ and $E_{DFT}\left(\text{bulk}\left(Ni\right)\right)$ are DFT-calculated energies for pure Pt and pure Ni in a bulk fcc crystal, respectively; and $E_{DFT}\left(O_2\left(g\right)\right)$ is the DFT-calculated energy for gas-phase molecule oxygen (O_2(g)). $E_{DFT}\left(O_2\left(g\right)\right)$ is corrected by the reference chemical potential for O_2(g), $\mu_{P_0,T} = 1.376\ eV$, which is defined and calculated based on Eq. (2.28) in Section 2.4.

Due to the loss of periodicity in one dimension, there are typically far more distinct, significant ECIs in a slab than in a bulk material. For example, on a bulk fcc lattice all nearest-neighbor 2-body (pair) clusters of sites are symmetrically equivalent and share a common ECI value. However in a slab a nearest-neighbor pair cluster of sites three layers below the surface is symmetrically distinct from one that is four layers below the surface. Separate ECI values must be determined for each of these clusters and all other symmetrically distinct clusters in the slab. To fit the ECI values for the slab cluster expansion with low computational cost, I have used a Bayesian method in which a prior probability distribution is defined over possible ECI values, and the shape of this prior is optimized by minimizing the leave-one-out cross validation error.[13, 22, 37] This method is particularly advantageous for surface cluster expansions, as the prior probability distribution can be used to express the prior expectation that the ECIs for congruent clusters (e.g. nearest-neighbor pairs that are three or four layers below the surface) should be similar, even if the clusters are not symmetrically equivalent. This approach significantly improves the predictive accuracy of the cluster expansion for a given training set size, reducing the

amount of training data that must be generated to reach a desired level of accuracy.[21, 69] Details of fitting ECIs of the cluster expansion on extended surfaces are as follows.

The cluster expansion included the empty cluster, the one-body (point) cluster, all 2-body clusters up to the 31st-nearest neighbor, all 3-body clusters up to the third-nearest neighbor, and all 4-body clusters up to the third-nearest neighbor, for a total of 329 symmetrically distinct cluster functions. The ECIs for these cluster functions were fit to the DFT-calculated formation energies of training set slabs using the Bayesian approach with a multivariate Gaussian prior distribution.[21] Among other advantages, this approach allows for more distinct ECIs to be included in the cluster expansion than there are structures in the training set, with computational cost and complexity nearly identical to that of a standard least-squares fit. The inverse of the covariance matrix for the prior distribution, Λ, is defined in Eq. (2.16) and Eq. (2.17). The parameters of λ_1, λ_2, λ_3, λ_4, and λ_5 were determined by using a conjugate gradient algorithm to minimize the leave-one-out cross validation score, an estimate of prediction error.[18] The final values for these parameters were 3.681×10^{-5}, 1.243×10^{-4}, 0.895, 2.939, and 0.423 respectively. The resulting cluster expansion had a root mean square leave-one-out cross validation (RMS LOO CV) error of 2.8 meV per atom.

3.3 Importance of ordering effects

Provided that the oxygen binding energy (ΔE_O, defined in Eq. (1.3)) is a widely used descriptor for ORR activity,[48-49, 55-56] predictions of which enable us to build a direct bridge between surface structures and catalytic activity of Pt-Ni catalysts. The oxygen binding energy and hence the catalytic activity – on metallic surfaces is commonly attributed to three effects: the effect of the bulk lattice parameter (the strain effect), the effect of alloying on the electronic structure of the active site (the ligand effect), and the effect of local atomic order near the active site (the ensemble effect).[132] Within a cluster expansion, the ensemble and ligand effects can be interpreted as the contributions from short-range (i.e. nearest-neighbor) and longer-range interactions, respectively. For simplicity I will refer to the effects due to all local interactions, including long-range, short-range, and many-body, as "ordering effects". These are distinguished from strain effects and "composition effects", which refer to the composition of the catalytic material.

I first consider the relative importance of strain effects and ordering/composition effects in determining the oxygen binding energy on Pt_3Ni. To do this, I have evaluated the oxygen binding energies on four different surfaces: Pt(111) with the calculated bulk Pt lattice parameter (Pt), Pt(111) with the calculated bulk Pt_3Ni lattice parameter (Pt/3.90), Pt_3Ni(111) with the calculated bulk Pt lattice parameter (Pt_3Ni/3.99), and Pt_3Ni(111) with the calculated bulk Pt_3Ni lattice parameter (Pt_3Ni). For the Pt_3Ni surfaces, I used a 2x2 unit cell with pure Pt in the first layer and 50% Pt in the second layer (Figure 3.2(b)), similar to the experimentally observed composition profile.[55] On each of these surfaces, I calculated

ΔE_O at a coverage of 1/4 monolayer (ML) on all symmetrically distinct fcc sites to evaluate how the underlying bulk chemistry and lattice parameters affect the predicted ORR activity. For each surface, the average value of ΔE_O and the minimum calculated value of ΔE_O (corresponding to the site on which oxygen adsorbs most strongly) are shown in Table 3.3.

Table 3.3. Oxygen binding energy changes relative to Pt, at a coverage of 1/4 ML.

surfaces	ΔE_O changes (strongest binding energy) / eV	$\langle \Delta E_O \rangle$ average changes / eV
Pt	0	0
Pt/3.90	0.180	0.180
$Pt_{27}Ni_9$/3.99	0.033	0.144
$Pt_{27}Ni_9$	0.291	0.433

From Pt (with the bulk Pt lattice parameter) to $Pt_{27}Ni_9$ (with the bulk Pt_3Ni lattice parameter), the average oxygen binding energy weakens by 0.433 eV, with contributions from both strain and ordering/composition effects. To distinguish the strain effects from the ordering/composition effects, I consider two different paths for transforming a Pt surface into a Pt_3Ni surface. In the first path I first apply a strain to the Pt surface to match the Pt_3Ni lattice parameter (strain effects), and then I replace selected Pt atoms with Ni atoms to create the surface structure shown in Figure 3.2(b) (ordering/composition effects). In the first step, the oxygen binding energy is reduced by about 0.180 eV, and in the second step the oxygen binding energy is reduced by 0.253 eV. I also consider the alternative path, in which first selected Pt atoms are replaced with Ni atoms to create the surface structure shown in Figure 3.2(b) (ordering/composition effects), and then the Pt surface is strained to match the Pt_3Ni lattice parameter (strain effects). In the first step in this path, the average oxygen binding energy is reduced by 0.144 eV, and in the second step the average oxygen binding energy is reduced by 0.289 eV.

These outcomes indicate that the contribution from the strain effect strongly depends on the composition and ordering of Pt/Ni(111) alloy surfaces, and vice versa. Thus it is hard to separate the strain and composition/ordering effects through direct comparison of oxygen binding energies. To better understand how local atomic order affects the binding energies of adsorbed oxygen atoms for Pt_3Ni, I directly analyze the effective cluster interactions (ECIs) in the cluster expansion.

In cluster expansions, the predicted oxygen binding energy is determined by the clusters containing the oxygen binding site (see Section 2.3 in Chapter 2). Examining the ECIs for clusters that contain oxygen binding sites can provide insight into how local atomic order affects the oxygen binding energy. In Figure 3.4, I show the significant contributions to oxygen binding energy coming from pair (2-body) clusters that contain one oxygen site and one metal site. For both fcc and hcp sites in the first layer of the surface, oxygen preferentially binds to nickel atom in the nearest-neighbor sites and platinum atoms in the next-nearest-neighbor sites. For the second layer, the differences between the hcp sites and fcc sites become more apparent. Oxygen bound at an hcp site prefers to be directly above a nickel atom in the second layer. For oxygen bound on an fcc site, the occupancy of the second-layer sites nearest to the adsorbed oxygen atom has little effect on the average oxygen binding energy. The more significant contribution to oxygen binding energy comes from the next-nearest second-layer sites. From the perspective of an oxygen atom adsorbed on an fcc site, these sites are nearly directly behind the nearest-neighbor sites on the surface, and on average the presence of platinum at these sites increases the oxygen binding energy (or equivalently, decreases ΔE_O).

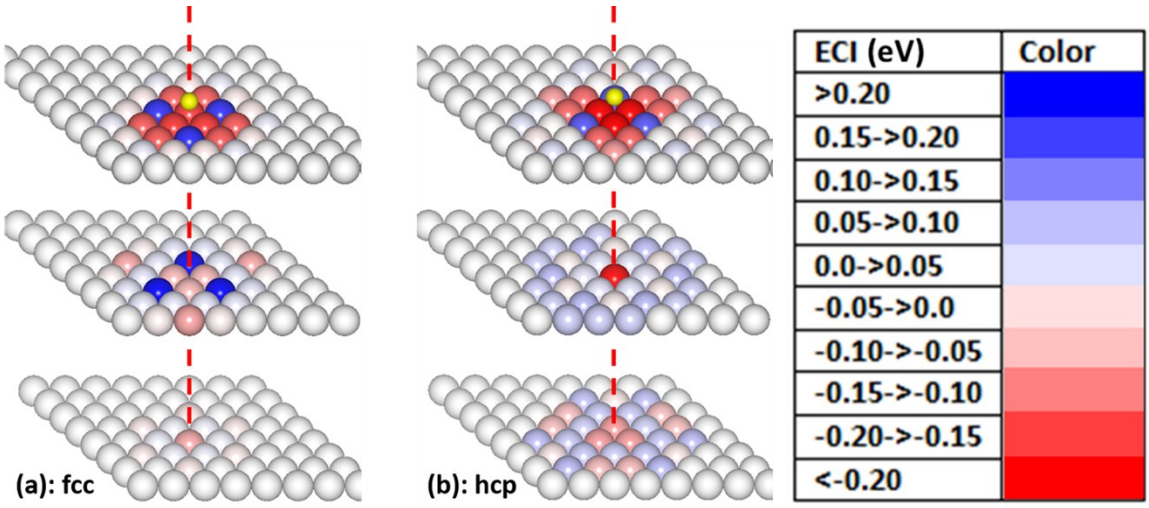

Figure 3.4. Effective cluster interactions (ECIs) map for pair clusters containing one oxygen binding site (yellow sphere) and one metal site within the outmost three layers of Pt/Ni(111) surface. The oxygen binding site is (a) fcc (b) hcp. For the Pt/Ni - vacancy/O system, the site variable value for O and Ni is -1, and for vacancy and Pt it is +1. Blue indicates a positive ECI (stronger oxygen binding when Pt is present), and red indicates a negative ECI (stronger oxygen binding when Ni is present).

To understand how local atomic order affects the oxygen binding energies, including many-body contributions, I used the cluster expansions in Metropolis Monte Carlo simulations[109, 133] to search for the local atomic order around a surface fcc site that results in the maximal and minimal oxygen binding energies. These simulations were run on 6×6(111) unit cells with 1/36 ML coverage of oxygen in a canonical ensemble at the stoichiometric composition of Pt_3Ni. I introduced a constraint that the first layer of the Pt_3Ni slab must be pure Pt skin because Pt-skin structures have been found to have an enhanced catalytic properties and stability.[48, 61, 65, 118] The middle layer of the 9-layer slab was fixed to be Pt_3Ni to mimic the existence of bulk Pt_3Ni underlying the surfaces.

The Monte Carlo simulations reveal that with the slab composition, lattice parameter, and the structures of the first and fifth layers held fixed, ΔE_O can range from a minimum of 153 meV above that of Pt to a maximum of 706 meV above that of Pt. Thus, variations in sub-surface atomic order can affect oxygen binding energies by more than 0.5 eV, which

can have significant effects on the catalytic properties of the surface. In the surface structure on which ΔE_O is lowest (Figure 3.5(a)), the adsorption site is above a triangle of Ni atoms in the second layer. These Ni atoms are surrounded by Pt atoms in the second layer. In the third layer, the site directly beneath the adsorbed oxygen contains a Ni atom surrounded by six Pt atoms. For the surface structure that maximizes ΔE_O, the opposite situation happens. The three sites in the second layer below the adsorption site contain Pt, and in the third layer the site directly below the adsorption site contains a Pt atom surrounded by six Ni atoms (Figure 3.5(b)).

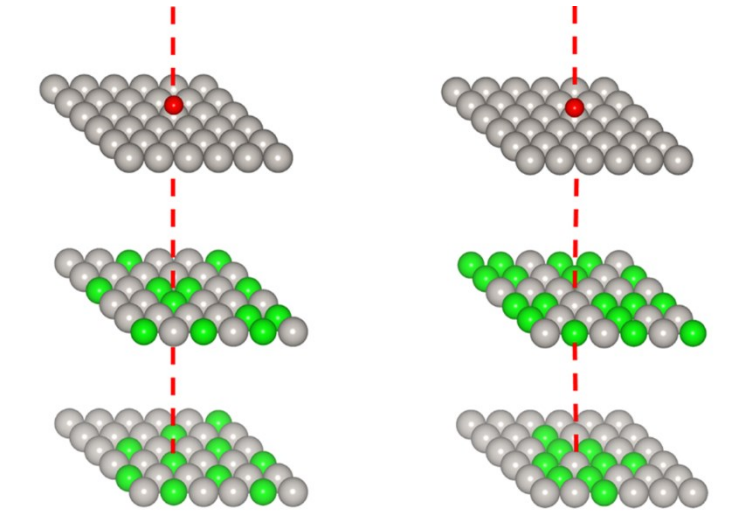

Figure 3.5. The local atomic orders of the top three layers of 6×6(111) Pt-skin surfaces with optimal oxygen binding energies for a stoichiometric Pt_3Ni surface. (a) The surface that minimizes ΔE_O; (b) The surface that maximizes ΔE_O. Oxygen binding energies are relative to that of a fcc site on a pure Pt(111) surface. Gray, green, and red spheres represent the Pt, Ni, and oxygen atoms, respectively.

3.4 Surface Structures

3.4.1 Equilibrium surfaces

The equilibrium atomic structure of an alloy surface will often differ from that of the bulk material. For example, differences in the surface energies of the constituent elements can drive the preferential segregation of one element to the surface. In addition, the equilibrium composition of the near-surface region of an alloy may have different stoichiometry from the underlying bulk material.

To predict the equilibrium near-surface structure for $Pt_3Ni(111)$, I modeled it in a grand canonical ensemble, as an open system that is in equilibrium with a Pt_3Ni bulk reservoir and can exchange Pt and Ni atoms, as well as adsorbed oxygen atoms, with its environment. In this way I can predict how the equilibrium composition, surface coverage, and atomic order of the surface slab respond to the chemical environment. The equilibrium structure is determined by the temperature, the partial pressure of oxygen, and the chemical potential difference between Pt and Ni. For simplicity, I define this chemical potential difference as:

$$\Delta\mu \equiv \mu(Pt) - \mu(Ni). \tag{3.3}$$

Within this model I used Monte Carlo simulations based on the cluster expansion Hamiltonian to search for equilibrium structures of stoichiometric and off-stoichiometric $Pt_3Ni(111)$ surfaces. These calculations were run on 12×12 unit cells on the (111) surface.

According to Pt-Ni phase diagrams,[134-136] at low temperatures bulk Pt_3Ni can be in equilibrium with bulk pure Pt or bulk PtNi. Using ground state density functional theory

calculations and a convex hull construction (Figure 3.6), I calculate that Pt_3Ni is stable when the value of $\Delta\mu$ is between 0.125 eV and 0.294 eV. In this chemical potential window, the Monte Carlo algorithm identified three off-stoichiometric ground state near-surface structures, each of which can be reduced to a 2×2 unit cells on the (111) surface. The chemical stability windows for each of these near-surface structures is provided in Table 3.4, where the value of $\Delta\mu$ at which two slabs with compositions $Pt_{(27-x)}Ni_{(9+x)}$ and $Pt_{(27+y)}Ni_{(9-y)}$ are in equilibrium is calculated as follows:

$$\Delta\mu = \frac{E_{DFT}(Pt_{(27+y)}Ni_{(9-y)}) - E_{DFT}(Pt_{(27-x)}Ni_{(9+x)})}{x+y}, \tag{3.4}$$

where E_{DFT} indicates a DFT-calculated energy.

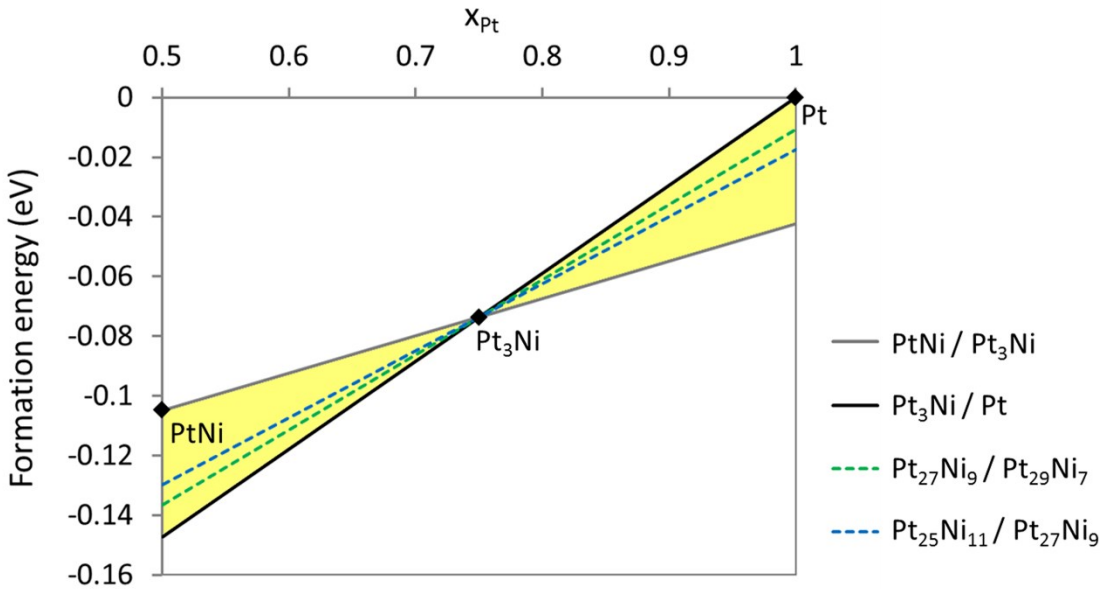

Figure 3.6. A Pt-Ni convex hull construction indicating the stability of the relevant phases. x_{Pt} is the number fraction of Pt in the bulk material, and only the right half of the diagram is shown. The diamond points indicate the DFT-calculated formation energies of three bulk phases. The values of $\Delta\mu$ at which various phases are in equilibrium are given by the slopes of the lines in the phase diagram. The shaded region between the solid grey line and the solid black line indicates the range in which bulk Pt_3Ni is stable. The dashed lines in this range indicate the phase boundaries between different Pt_3Ni ground state surface structures.

Table 3.4. The windows of $\Delta\mu$ (chemical potential difference between Pt and Ni) for bulk Pt/Ni alloys and $Pt_3Ni(111)$ ground state surface structures at 0K. The compositions of the surfaces are those of a nine-layer (2x2) slab.

pair structures in equilibrium		$\Delta\mu$ / eV	
		minimum	maximum
bulk Pt/Ni alloy	PtNi	N/A	0.125
	Pt_3Ni	0.125	0.294
	pure Pt	0.294	∞
Pt_3Ni (111) surfaces	$Pt_{25}Ni_{11}$	0.125	0.224
	$Pt_{27}Ni_9$	0.224	0.252
	$Pt_{29}Ni_7$	0.252	0.294

Within the chemical potential window at which ground state Pt_3Ni is stable, three near-surface structures are predicted to be thermodynamically stable ground states (Figure 3.7). I label these structures $Pt_{29}Ni_7$, $Pt_{27}Ni_9$, and $Pt_{25}Ni_{11}$ based on the composition of the 2×2 slab. In particular I note that the $Pt_{29}Ni_7$ structure (Pt-skin on a Pt_3Ni substrate)[51, 123] and the $Pt_{27}Ni_9$ structure (Pt-skin with 75% Ni in the second layer)[48, 50, 119-121] are similar to model structures evaluated in previous computational work. The chemical stability window of $Pt_{27}Ni_9$, representing a stoichiometric surface, is the narrowest of the three structures. These structures all have a monolayer Pt skin, in agreement with experimental evidence that Pt atoms in Pt/Ni(111) alloys tend to segregate to the outmost atomic layer of surface.[48, 53, 61, 65, 118, 137] It is of interest that according to these results, it is possible for the $Pt_3Ni(111)$ surface to be thermodynamically stable in a chemical environment that leaves the second layer either Ni-rich or Ni-poor relative to the stoichiometric Pt_3Ni surface. However at low temperatures, I predict that a chemical environment that strips all Ni from the second layer of a clean Pt_3Ni surface will make the underlying bulk material unstable.

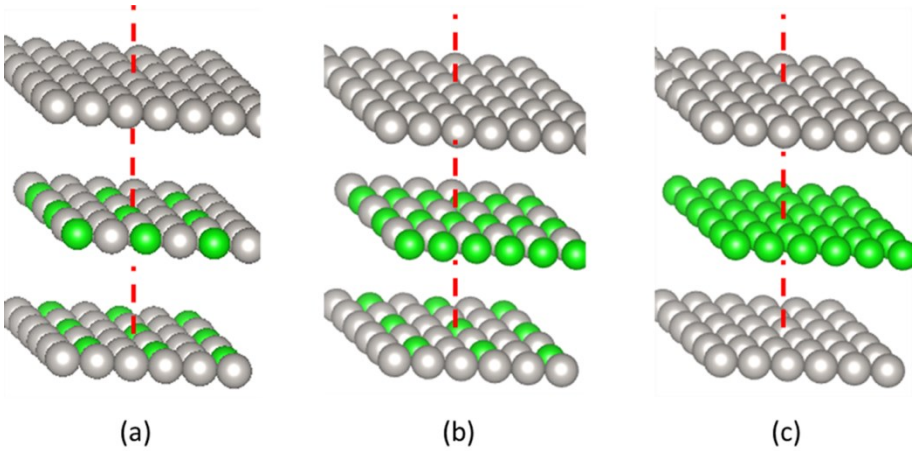

Figure 3.7. The top three layers of three equilibrium surfaces that are in equilibrium with bulk Pt_3Ni. Their fourth and fifth layers are equivalent to Figure 3.2(b) with 75% Pt composition. Gray and green spheres represent the Pt and Ni atoms, respectively. (a) The $Pt_{29}Ni_7$ structure; (b) The $Pt_{27}Ni_9$ structure; (c) The $Pt_{25}Ni_{11}$ structure.

At finite temperatures, configurational disorder appears in the atomic structure of the near-surface layers, allowing for a continuous range of compositions in thermodynamic equilibrium (Figure 3.8). As an example of one of these structures, I have used the cluster expansion to predict the near-surface structure of the highly active $Pt_3Ni(111)$ surface that was experimentally characterized by Stamenkovic et al.[53] The experimentally-determined composition profile of this surface was 100% Pt in the first layer, 48% Pt in the second layer, 87% Pt in the third layer, and 75% Pt in layers below the third layer. On average, the surface layers are more Pt rich than the Pt_3Ni bulk. To determine the equilibrium atomic structure of surfaces at this composition, I created symmetric nine-layer slabs with the same average composition (77.2 % Pt) as would be expected based on the experimental results. Using 12×12 unit cells, I ran canonical (fixed-composition of $Pt_{1000}Ni_{296}$) Monte Carlo simulations from 0 to 1600 K and recorded the average composition of each layer in the slab. The results are shown in Figure 3.9(a).

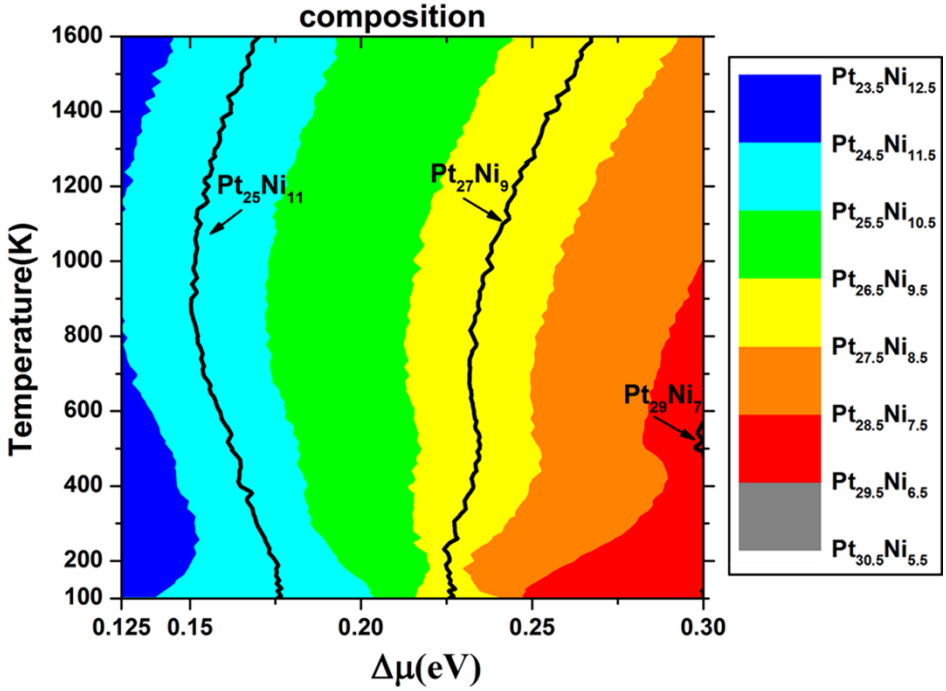

Figure 3.8. The equilibrium compositions of 9-layer Pt-Ni slabs as a function of $\Delta\mu \equiv \mu(Pt) - \mu(Ni)$ and temperature.

The composition profile in Figure 3.9(a) shows interesting behavior with temperature. At high temperatures, as would be expected, the compositions of all of the layers begin to approach the average composition of the slab (77.2 % Pt). At low temperatures, they resemble that of the $Pt_{27}Ni_9$ ground state structure (Figure 3.7(b)), with the excess Pt in the second layer, as would be expected based on the $Pt_{29}Ni_7$ ground state structure (Figure 3.7(a)). At temperatures of around 400K or 780K, the simulated result (Figure 3.9(b)) has a composition profile that is in excellent agreement with the composition profile observed by Stamenkovic et al.[53] At room temperature, the surface may be kinetically trapped in one of these metastable higher-temperature surface structures.

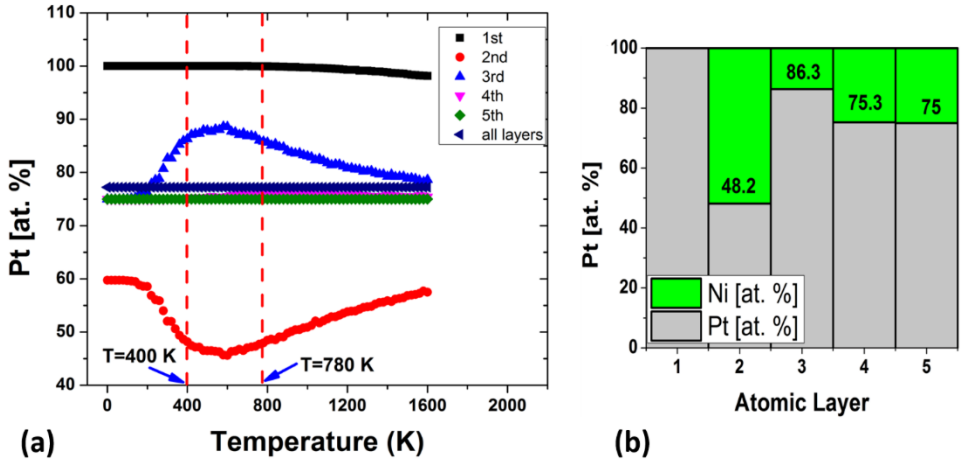

Figure 3.9. (a): The composition profile as a function of temperature based on cluster expansion on the 12×12 surfaces with fixed composition of 77.2 % Pt ($Pt_{1000}Ni_{296}$). (b): The composition profile corresponding to temperature at 400K in Figure (a).

A snapshot of a surface structure of $Pt_{1000}Ni_{296}$ at 400 K is shown in Figure 3.10(a). I predict that at this temperature, the first layer is pure Pt and the second layer is disordered, with increasing atomic order in subsequent layers. The gas-phase oxygen binding energy at every fcc site with 1/144 ML coverage was calculated using the cluster expansion. To compare these energies with ΔE_O at Pt(111) surface with 1/4 ML coverage, a constant shift of 18.8 meV per adsorbed atomic oxygen was added to ΔE_O calculated at 1/144 ML coverage. This constant shift was calculated by taking the difference between ΔE_O on the pure Pt(111) surface at 1/4 ML coverage and ΔE_O on the pure Pt(111) surface at 1/144 ML coverage as calculated using the cluster expansion. The same shift was found for the three ground state Pt-Ni(111) alloy surfaces in Table 3.4, suggesting that the difference between ΔE_O at 1/4 monolayer coverage and ΔE_O at 1/144 monolayer coverage is predominantly due to O-O interactions on the surface. The pair interactions shown in Figure 3.4, along with many-body interactions, lead to a wide variety of oxygen binding energies (ΔE_O) on the surface of this Pt-skin structure, as shown in Figure 3.10(b). In this snapshot, variation

in local atomic order in the second and third layers leads to the values of ΔE_O that span a range of 340 meV on different fcc surface sites (Figure 3.10(b)). The average distribution of oxygen binding energies across different surface sites, as calculated using canonical Monte Carlo simulations, is shown in Figure 3.10(c).

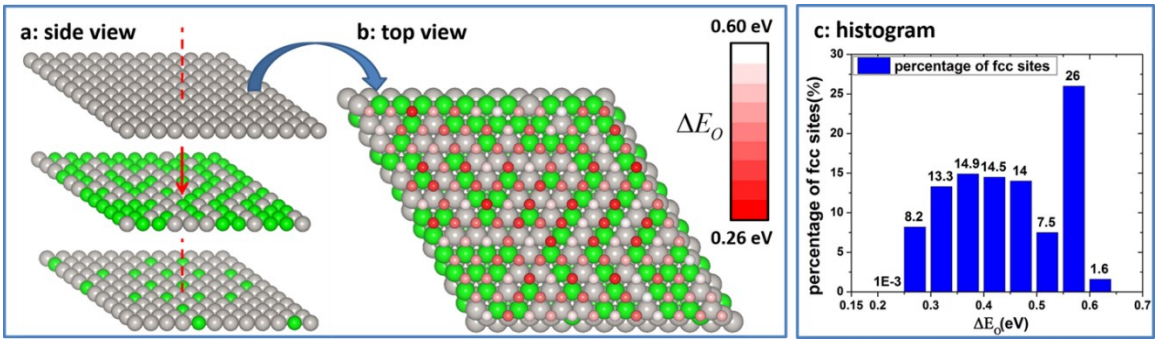

Figure 3.10. Side view and top view of snapshot structure with 12×12 (111) unit cell at temperature = 400 K, and histogram of oxygen binding energies. This slab structure has composition of $Pt_{1000}Ni_{296}$. (a) The side view of first, second and third layers. (b) The top view of the second layer, showing the gas-phase oxygen binding energy (ΔE_O) at every fcc site with 1/144 ML coverage. The Pt-skin first layer is removed in order to have a clear view of the second layer. Large gray and green spheres represent the Pt and Ni atoms, respectively. The small spheres in (b) represent the oxygen atoms, where redder spheres indicate stronger binding between oxygen and the surface. (c) The histogram of oxygen binding energies (ΔE_O) on the $Pt_{1000}Ni_{296}$ surface calculated using canonical Monte Carlo simulations. The x-axis is ΔE_O, and the y-axis is percentage of fcc sites for which ΔE_O falls into the range of each bar. The value of ΔE_O in (b) and (c) is relative to that of a Pt(111) surface with 1/4 ML coverage.

3.4.2 Effect of oxygen adsorption

To model the effect of exposure of a $Pt_3Ni(111)$ surface to an oxidizing environment a series of Monte Carlo simulations with 12×12(111) unit cells were run at different oxygen chemical potentials at 298 K. Oxygen chemical potentials were related to oxygen partial pressures using the following expression (defined in Eq. (2.27)):

$$\mu_{O_2}(T, p_{O_2}) = \mu_{O_2}(T, p^0) + kT \ln(\frac{p_{O_2}}{p^0}), \tag{3.5}$$

where the reference value, $\mu_{O_2}(T, p^0)$, is fit to experimental data as described in subsection 2.4. Composition profiles of the near-surface structure as a function of O_2 partial pressure and $\Delta\mu$ ($\Delta\mu \equiv \mu(Pt) - \mu(Ni)$) are given in Figure 3.11 and Figure 3.12 under different constraints.

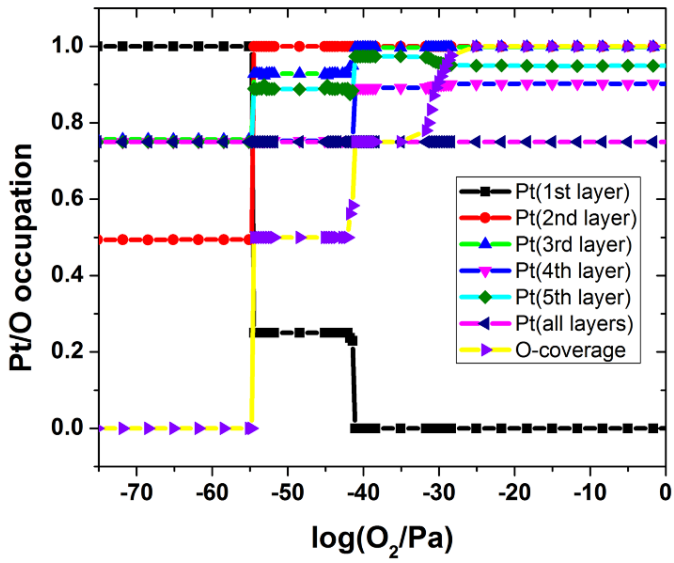

Figure 3.11. The composition profile of Pt-Ni-O system under fixed Pt composition with 75% Pt at 298K. The x-axis is the logarithm of O_2 partial pressure and the y-axis is Pt/O occupation, i.e. the Pt compositions in the $Pt_3Ni(111)$ layers and oxygen coverage on the $Pt_3Ni(111)$ surface.

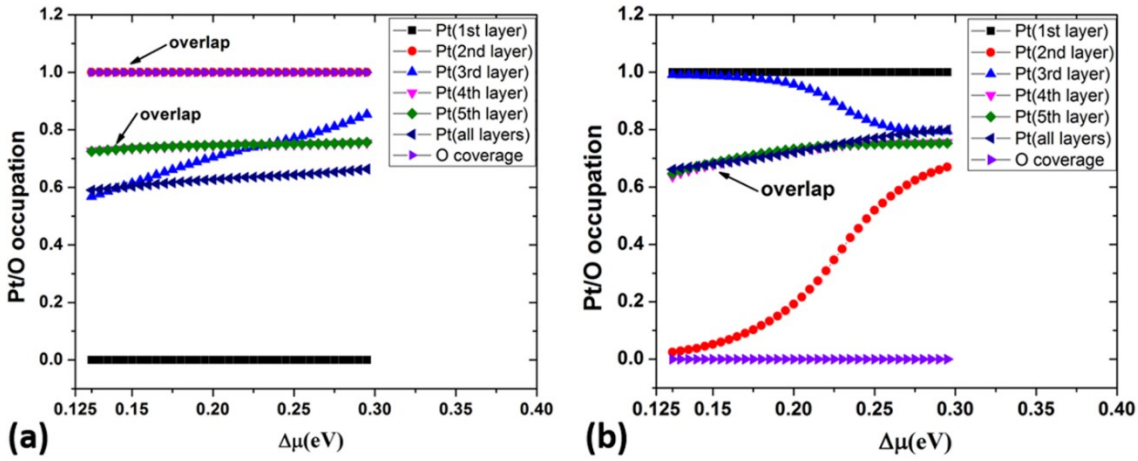

Figure 3.12. The composition profile of the Pt-Ni-O system under fixed O_2 partial pressure at 298 K. (a) $p_{O_2} = 0.21\ atm$ at 298 K; (b) $p_{O_2} = 0.0\ atm$ at 298 K. The x-axis is $\Delta\mu \equiv \mu(Pt) - \mu(Ni)$ and the y-axis shows the Pt composition for Pt/Ni(111) layers and the oxygen coverage on the surface. In (a), the data points for the second layer and oxygen coverage overlap each other, as do the points for the compositions of the fourth and fifth layers. In (b), the data points for the fourth layer and fifth layer overlap.

For a stoichiometric Pt_3Ni slab, oxygen coverage will increase from 0 to 1.0 ML when the O_2 partial pressure increases. The surface with zero oxygen coverage has a Pt-skin structure, and a monolayer of surface coverage pulls Ni atoms from inner layers to the outer layer, resulting in pure Ni in the outmost layer (Figure 3.11). There are two intermediate phases, with oxygen coverage of 0.5 ML and 0.75 ML as shown in Figure 3.13. For the surface with 0.5ML oxygen coverage (Figure 3.13(a)), half of the oxygen atoms occupy fcc sites and the other half occupies hcp sites; also, Ni atoms are pulled from sub-surface layers to the first layer ending up with 75% Ni in the first layer. For the surface with 0.75ML coverage (Figure 3.13(b)), all of oxygen atoms occupy fcc sites. This surface has 100% Ni in the first layer and 100% Pt in the second layer. I note that at high oxygen coverages, oxygen adsorbates can drive the surface reconstruction on Ni(111) surface or the formation of oxide phases.[138] Because I do not take into account possible surface

reconstructions or the formation of new phases that don't conform to the bulk fcc lattice, there may be alternative surface phases at high oxygen coverage that are more stable than those I predict.

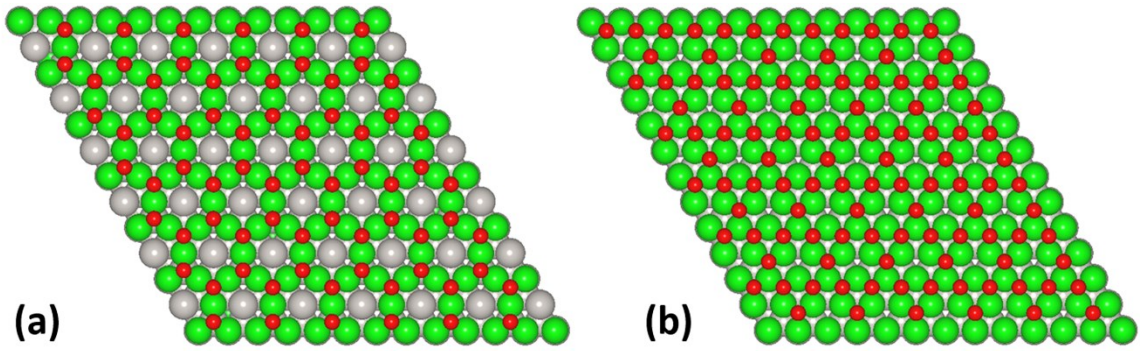

Figure 3.13. Top view of 12×12(111) surfaces with 0.5ML (a) and 0.75ML (b) oxygen coverages. Gray, green and red spheres represent the Pt, Ni and oxygen atoms, respectively.

Figure 3.12 shows how the equilibrium surface structures of the Pt-Ni-O system depend on $\Delta\mu$ when the chemical potential of O_2 is fixed and within the chemical potential window where bulk Pt_3Ni is stable at 0 K. Specifically, when the O_2 partial pressure is 0.21 atm, as shown in Figure 3.12 (a), the oxygen coverage is 1.0 ML. As $\Delta\mu$ increases, the Pt compositions of first, second, fourth and fifth layers barely change, and the Pt composition of third layer increases slowly. Figure 3.12 (b) shows the situation of zero oxygen coverage when O_2 partial pressure is zero. As $\Delta\mu$ increases, the Pt composition of the first layer remains at 100%, and that of second, fourth and fifth layers increases. The third layer becomes less Pt-rich even as the overall near-surface region becomes less Ni-rich, due to interactions between the third layer and the decreasingly Ni-rich second layer. These results illustrate the interplay between surface segregation and alloying in Pt-Ni surfaces.

The composition of the outermost layer is primarily determined by the chemical environment (Ni-rich in oxidizing conditions, Pt-rich in vacuum). Off-stoichiometry is accommodated in the sub-surface layers through the formation of alternating Ni-rich and Pt-rich layers, consistent with experimental observations.[53]

Provided electrochemical oxygen reduction reaction (ORR) was carried out at room temperature, Pt and Ni atoms of experimentally prepared Pt-skin surfaces[53, 61] may reach the equilibrium states (Ni-rich surfaces) very slowly after surface exposure to an oxidizing environment (shown in Figure 3.11 and Figure 3.12(a)). This may lead to the Pt/Ni surfaces kinetically trapped in thermodynamically metastable Pt-skin (or almost Pt-skin) surface structures in oxidizing conditions. Thus, with the limitation of the outmost layer fixed as Pt-skin, it is worth investigating how the near surface structures will correspond to the oxygen partial pressure (oxygen coverage) on the extended surfaces. The results from Monte Carlo simulations are shown in Figure 3.14. Under grand canonical ensemble (Figure 3.14(a)), I found that as the oxygen coverage increases from 0 to 1 ML, the Pt composition in the second layer increases from 63.3% Pt to 100.0% Pt, and that in the third, fourth and fifth layers remain 75% Pt. Under mix ensemble with fixed Pt composition with 75% Pt (Figure 3.14(b)), as the oxygen coverage increases, the Pt composition in the second layer increases from 49.3% Pt to 92.2% Pt, that in third layer decreases from 75.7% Pt to 48.4% Pt, that in fourth layer decreases from 75.0% Pt to 59.4% Pt, and that in fifth layer remains 75% Pt. In totally, Figure 3.14 shows that strong oxygen binding energy (ΔE_O) will pull Pt atoms in the inner layers to the second layer on the kinetically trapped Pt-skin Pt_3Ni surfaces, resulting in Pt-rich in the second layer that helps improve the ORR activity.[53]

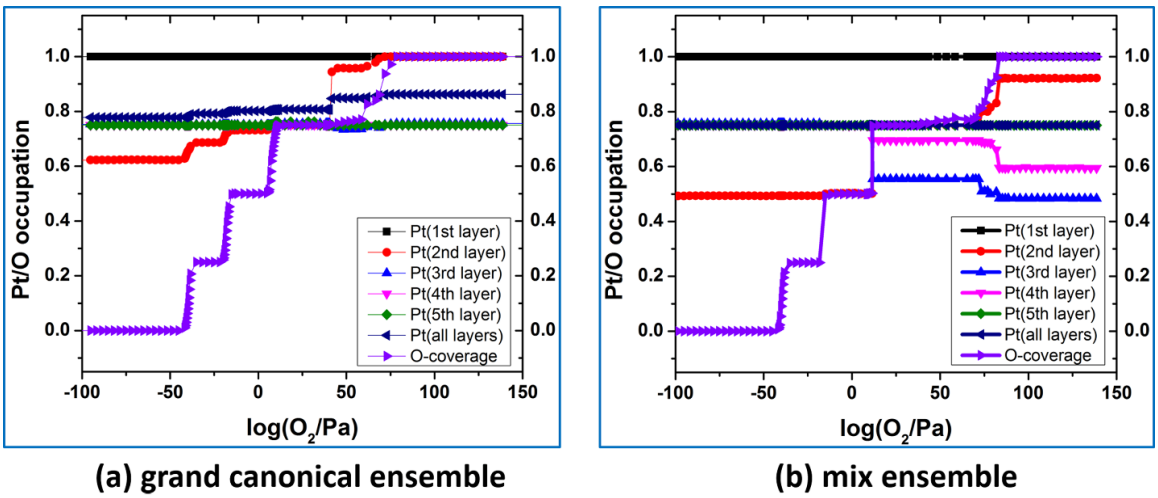

Figure 3.14. Composition profile of extended surfaces (Pt−Ni−O system) under (a) grand canonical ensemble and (b) mix ensemble with the first layer fixed as Pt-skin structure at 298 K. For (a) grand canonical ensemble: both Pt/Ni and Vacancy/O groups are grand canonical ensemble with $\Delta\mu = 0.24\ eV$; for (b) mix ensemble: Pt/Ni group is canonical ensemble under fixed Pt composition with 75% Pt, and Vacancy/O group is grand canonical ensemble. The x-axis is the logarithm of O_2 partial pressure and the y-axis is Pt/O occupation, that is, the Pt compositions in the Pt/Ni(111) layers and oxygen coverage on the Pt/Ni(111) extended surface.

3.5 Catalytic activity

At oxygen reduction potentials around 0.9 V, the oxygen reduction reaction (ORR) on fcc (111) surfaces is widely believed to occur via the associative mechanism composed of the following steps:[56-57]

In the anode:

$$H_2 \rightarrow 2H^* \rightarrow 2H^+ + 2e^- \tag{3.6}$$

In the cathode:

$$O_2(g) + 4(H^+ + e^-) \leftrightarrow *OOH + 3(H^+ + e^-) \tag{3.7}$$

$$*OOH + 3(H^+ + e^-) \rightarrow *O + 2(H^+ + e^-) + H_2O(l) \tag{3.8}$$

$$*O + 2(H^+ + e^-) + H_2O(l) \rightarrow *OH + (H^+ + e^-) + H_2O(l) \tag{3.9}$$

$$*OH + (H^+ + e^-) + H_2O(l) \rightarrow 2H_2O(l) \tag{3.10}$$

Under this mechanism, ΔE_O is a suitable descriptor of ORR activity because it can be linearly related to the binding energies of all the intermediates of the ORR,[139-140] including *OOH, *O, and *OH. Through these linear relationships, it is possible to construct a "volcano plot" that relates ΔE_O to the negative of the activation barrier for the reaction, a measure of catalytic activity. (For the purpose of succinctness and keeping with convention, I will refer to this measure simply as "activity".) The basic shape of the volcano plot for the ORR on fcc (111) surfaces has been established through both calculations and comparisons with experiment on a variety of different surfaces.[48-49, 55-56]

Here I built the volcano plot (relationship) based on the work of Karlberg et al.[56], and I will briefly demonstrate how the free energy change for each step is determined. As shown in the work of Rossmeisl et al.[140], there exist linear relationships between the binding energies of all intermediates. The change in free energies for the reactions in associative mechanism can be expressed as a linear function of ΔE_O as follows,

$$\Delta E_{OOH} = 0.53 * \Delta E_O + 3.18\, e\mathrm{V} \tag{3.11}$$

$$\Delta E_{OH} = 0.50 * \Delta E_O + 0.05\, e\mathrm{V} \tag{3.12}$$

Here, ΔE_O is the reaction energy of $H_2O + * \rightarrow *O + H_2$, defined in Eq. (1.3). Also, in order to include the effect of surrounding water, the above energies should be corrected with shift corresponding to interaction energy between water layers and adsorbates, $\Delta E_{\mathrm{water}}$. For all Pt/Ni(111) surfaces in this chapter, I used the shift of the work of Karlberg et. al.[56], where $\Delta E_{\mathrm{water}}(\mathrm{OOH}) = -0.23$ eV, $\Delta E_{\mathrm{water}}(\mathrm{O}) = 0$ and $\Delta E_{\mathrm{water}}(\mathrm{OH}) = -0.6$ eV.

At potential of 0.9 V, OH is stabilized by ~0.1 eV because of relative high potential. Based on the method of building volcano plot,[56] the free energy changes for four intermediate reaction steps of ORR (shown in Eq. (3.7), Eq. (3.8), Eq. (3.9), and Eq. (3.10)) are expressed as:

$$\Delta G_{A1} = \Delta G_{OOH} - \Delta G_{O_2} + eU = 0.53\Delta G_O - 1.56 + eU \tag{3.13}$$

$$\Delta G_{A2} = \Delta G_O - \Delta G_{OOH} + eU = 0.47\Delta G_O - 3.32 + eU \tag{3.14}$$

$$\Delta G_{A3} = \Delta G_{OH} - \Delta G_O + eU = -0.5\Delta G_O - 0.35 + eU \tag{3.15}$$

$$\Delta G_{A4} = \Delta G_{H_2O} - \Delta G_{OH} + eU = -0.5\Delta G_O + 0.3 + eU \tag{3.16}$$

And under the definition of activity in the work of Nørskov et al.[55], the activity is given by:

$$activity = \min(-\Delta G_{A1}, -\Delta G_{A2}, -\Delta G_{A3}, -\Delta G_{A4}). \quad (3.17)$$

Substituting Eq. (3.13), Eq. (3.14), Eq. (3.15), and Eq. (3.16) into Eq. (3.17), I obtained the activity expression at an applied potential of U=0.9 V,

$$activity = \min(-0.297 + 0.5*(\Delta E_O - 1.806), -0.297 + 0.53*(1.806 - \Delta E_O)), \quad (3.18)$$

where ΔE_O is calculated in vacuum at a coverage of quarter monolayer (0.25ML).

There is a constant shift of -0.09 eV for the oxygen binding energy on the pure Pt(111) surface between my DFT calculations and the results of Karlberg et al.[56] and Nørskov et al.[55] For the purpose of consistency, I shift the maximal position in Eq. (3.18) to the left by 0.09 eV, which means that the volcano plot I use is defined by

$$activity = \min(-0.297 + 0.5*(\Delta E_O - 1.716), -0.297 + 0.53*(1.716 - \Delta E_O)). \quad (3.19)$$

The peak position is $\Delta E_O = 1.716$ eV. The volcano plot based on Eq. (3.19) is shown in Figure 3.15.

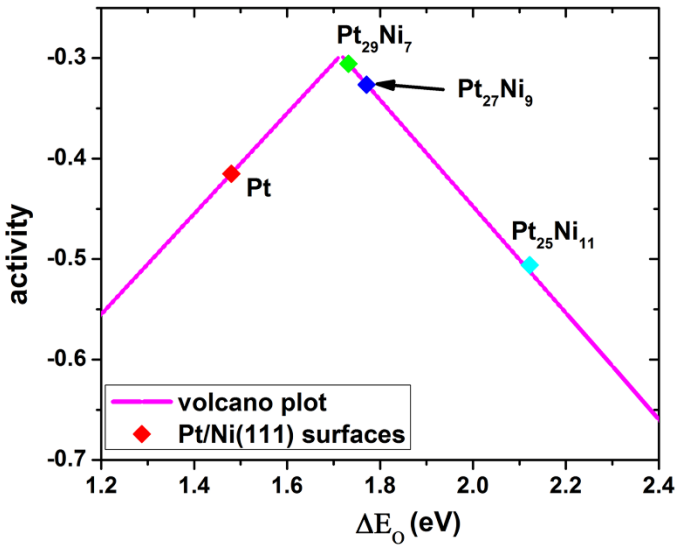

Figure 3.15. A volcano plot at an applied potential of 0.9 V based on Eq. (3.19) where the peak is $\Delta E_O = 1.716\ eV$. The predicted activities of Pt(111), $Pt_{29}Ni_7$, $Pt_{27}Ni_9$, and $Pt_{25}Ni_{11}$ are included. The values of ΔE_O used in this plot are the minimum values on each surface (indicating the most strongly bound oxygen) at 1/4 ML oxygen coverage.

I have used Eq. (3.19) to estimate the catalytic activity of the different ground state $Pt_3Ni(111)$ surfaces described in the previous sections. For the Pt(111), $Pt_{29}Ni_7$, $Pt_{27}Ni_9$, and $Pt_{25}Ni_{11}$ surfaces, DFT was used to calculate the value of ΔE_O for oxygen adsorbed on the site at which it is most strongly bound at a coverage of 1/4ML. For these surfaces, ΔE_O values are 1.48 eV, 1.73 eV, 1.77 eV and 2.12 eV respectively, and their activities as calculated using Eq. (3.19) are plotted on the volcano plot in Figure 3.15. These results are consistent with previously generated volcano plots,[48-49] in that $Pt_{27}Ni_9$ (in the form of Pt_3Ni) is slightly to the right of the peak with higher activity than Pt(111).

At finite temperatures, I use a similar analysis to estimate the catalytic activity of disordered surfaces. As the measure of activity shown in Eq. (3.19) is the negative of the activation barrier for the reaction, it can be related to the ORR current I through:[55]

$$I = I_0 \exp\left(\frac{activity}{kT}\right), \tag{3.20}$$

where I_0 is some constant, k is Boltzmann's constant, and T is temperature. By this definition, I can calculate the relative extent to which each site on the surface can be expected to contribute to the ORR current. For example, in the snapshot surface of thermodynamically stable $Pt_{1000}Ni_{296}$ shown in Figure 3.10, the ratio of I for the most active site (with $\Delta E_O = 0.26\ eV$ referenced to Pt(111)) to I for the least active site (with $\Delta E_O = 0.60\ eV$ referenced to Pt(111)) at 300 K is 1179, indicating that catalytic activity can vary significantly by a factor of 1000 across the surface due to the underlying disorder in the second and (to a lesser extent) third layers. (Unless otherwise noted, all currents are calculated at 300 K). The Figure 3.16 demonstrates the importance of sub-surface atomic order to determine the site-specific ORR activity in volcano plot.

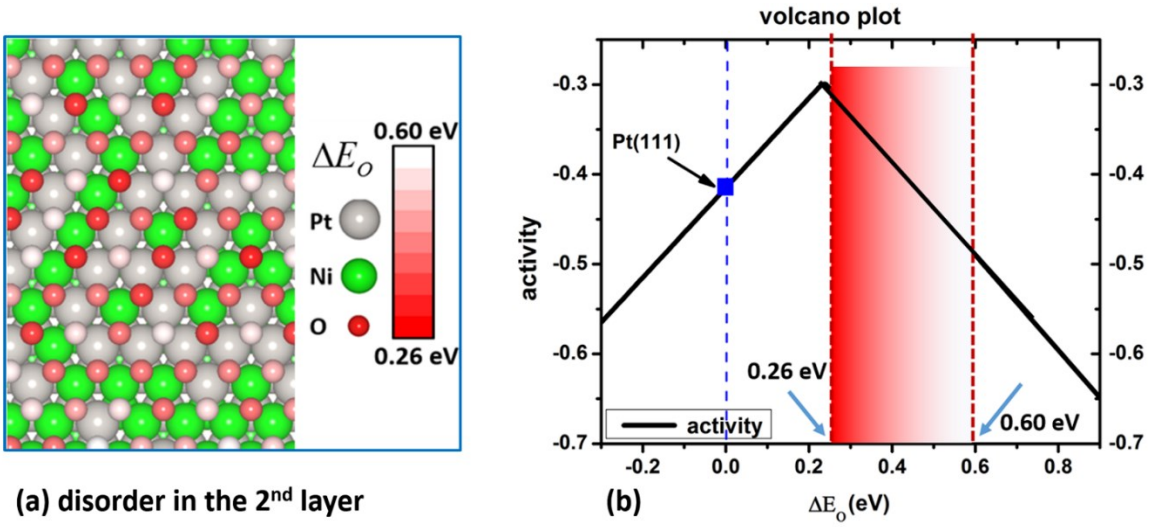

Figure 3.16. The dramatic effect of local atomic order on its corresponding site-specific ORR activity. (a) disorder in the second layer: the screenshot of snapshot surface of thermodynamically stable $Pt_{1000}Ni_{296}$ in Figure 3.10, and (b) the volcano plot shows the sensitivity of ORR activity within the range of ΔE_O in Figure (a), which is highlighted by the red-shaded area.

Using only the binding energy for the site on which oxygen binds most strongly, the volcano plot (Figure 3.15) indicates that the $Pt_3Ni(111)$ surface (here is in the form of $Pt_{27}Ni_9$ in Figure 3.7(b)) has 34 times higher ORR current than pure Pt(111). In comparison, Stamenkovic et al. measure a current that is only about 10 times greater than Pt on their off-stoichiometric $Pt_3Ni(111)$ surface.[53] This discrepancy may be partially explained by considering that when the specific activity is experimentally measured, oxygen reduction could occur on any site. To account for the variety of different possible adsorption sites on these surfaces I introduce the definitions of the average current over all oxygen binding sites on the catalytic surface, $\langle I \rangle$:

$$\langle I \rangle = \frac{\sum_{j=1}^{N} I_j}{N}. \tag{3.21}$$

Since oxygen preferentially adsorbs on fcc sites on Pt/Ni(111) surfaces, I calculate the average current ($\langle I \rangle$) over all fcc sites.

Using Eq. (3.20) and Eq. (3.21), the average current of the ground state $Pt_{27}Ni_9(111)$ surface is predicted to be 15.6 times to that of pure Pt(111) surface at 300 K, which is closer to the Stamenkovic et al.'s experimental result that the ORR was enhanced by factor of 10 compared with Pt(111).[53] Similarly, the average currents for the $Pt_{25}Ni_{11}$ surface and the $Pt_{29}Ni_7$ are calculated to be 1.7E-2 and 52.3 times that of pure Pt(111) respectively. By this measure, the Pt-rich $Pt_{29}Ni_7$ surface (Figure 3.7(a)) is predicted to have the highest catalytic activity. This suggests that the catalytic activity of Pt_3Ni can be increased by synthesizing the surface in a chemical environment in which bulk Pt_3Ni with a Ni-deficient surface is

thermodynamically stable (Figure 3.6).

For better comparison with experiment, I have used Monte Carlo simulations to calculate the average current for surfaces matching the experimental composition.[53] The Monte Carlo simulations were run in a canonical ensemble, sampling different Pt-Ni atomic arrangements while holding the composition of the slab fixed. The simulations were run on 12×12(111) Pt/Ni(111) supercells with composition $Pt_{1000}Ni_{296}$ (77.2% Pt). At each step in the Monte Carlo simulations, the gas-phase oxygen binding energy of every fcc site at 1/144 ML coverage was calculated using the cluster expansion. To use these energies in the volcano plot based on 1/4 ML coverage, a constant shift of 18.8 meV per adsorbed atomic oxygen was added to ΔE_O calculated at 1/144 monolayer coverage as mentioned in previous section. Using the shifted ΔE_O in the volcano plot shown in Figure 3.15, I calculated the estimated activity at each site, and site-specific currents (I) were calculated using Eq. (3.20). The average current across all sites was calculated at each step in the Monte Carlo simulation according to Eq. (3.21).

At the temperature of 400K or 780K where the composition profile is consistent with the work of Stamenkovic et al.,[53] the predicted average current is 7.8 times that of pure Pt at 400K and 6.1 times that of pure Pt at 780K (Figure 3.17). These values are close to the factor of 10 enhancement observed experimentally.[53] Although the composition profile is similar at each temperature, some of the difference in the average current is likely driven by the greater atomic disorder at 780K.

The calculations plotted in Figure 3.17 suggest that the higher specific activity is achievable from a Pt_3Ni surface that is either more ordered (in equilibrium at lower temperatures) or more disordered (in equilibrium at higher temperatures). However

achieving either of these in practice may prove difficult. At lower temperatures, the surface may be kinetically trapped in a disordered state and transform very slowly into the more highly active well-ordered surface structures. At higher temperatures, significant amounts of Ni start to appear on the Pt_3Ni surface (Figure 3.9), which may make the catalyst vulnerable to performance degradation due to Ni dissolution. Simulations on a surface that is constrained to have a Pt skin (Figure 3.17) indicate that some, but not all, of the increase in activity at higher temperatures is due to the presences of surface Ni (Figure 3.9).

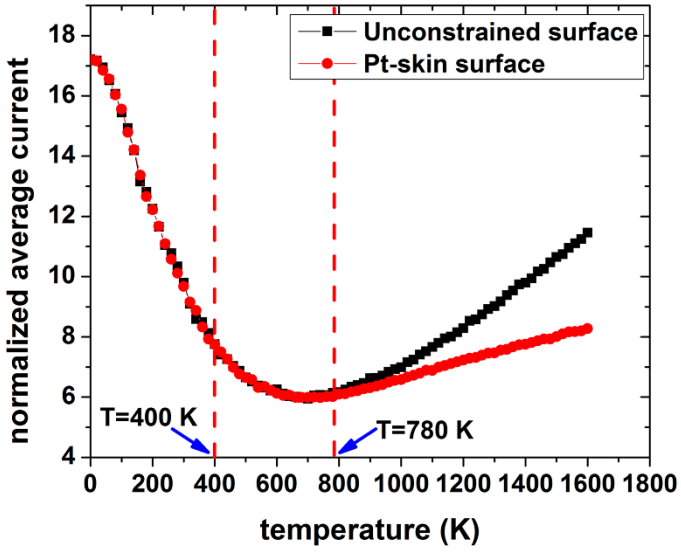

Figure 3.17. Average currents predicted based on volcano plot in Figure 3.15 and cluster expansions on the 12×12(111) surfaces with fixed composition $Pt_{1000}Ni_{296}$. "Pt-skin surface" means that the first layer of the slab is pure Pt, and the "Unconstrained surface" means that Ni atoms can segregate to outmost layer at high temperature as shown in Figure 3.9(a). All the average current values are normalized to that of a pure Pt(111) surface.

Since the equilibrium surfaces can be tuned by setting different chemical potentials and temperatures as discussed in Section 3.3, it is instructive to construct a diagram of average currents as a function of $\Delta\mu \equiv \mu(Pt) - \mu(Ni)$ and temperature. I have constructed such diagrams by running Monte Carlo simulations in a grand canonical ensemble on 12×12(111)

Pt/Ni(111) surfaces in the chemical potential window where bulk Pt_3Ni is stable at 0 K (Table 3.4). Through this process I am able to estimate the activities of different $Pt_3Ni(111)$ surfaces as a function of the chemical potential and temperature at which the surface is in equilibrium. The results are shown in Figure 3.18. To enable comparison with surface stoichiometry, the corresponding surface stoichiometry plot is shown in Figure 3.8. The average current of ORR reaches the maximum in the right bottom area of diagram, which corresponds to the ground state $Pt_{29}Ni_7$ surface at a temperature of 0K (Figure 3.7(a)).

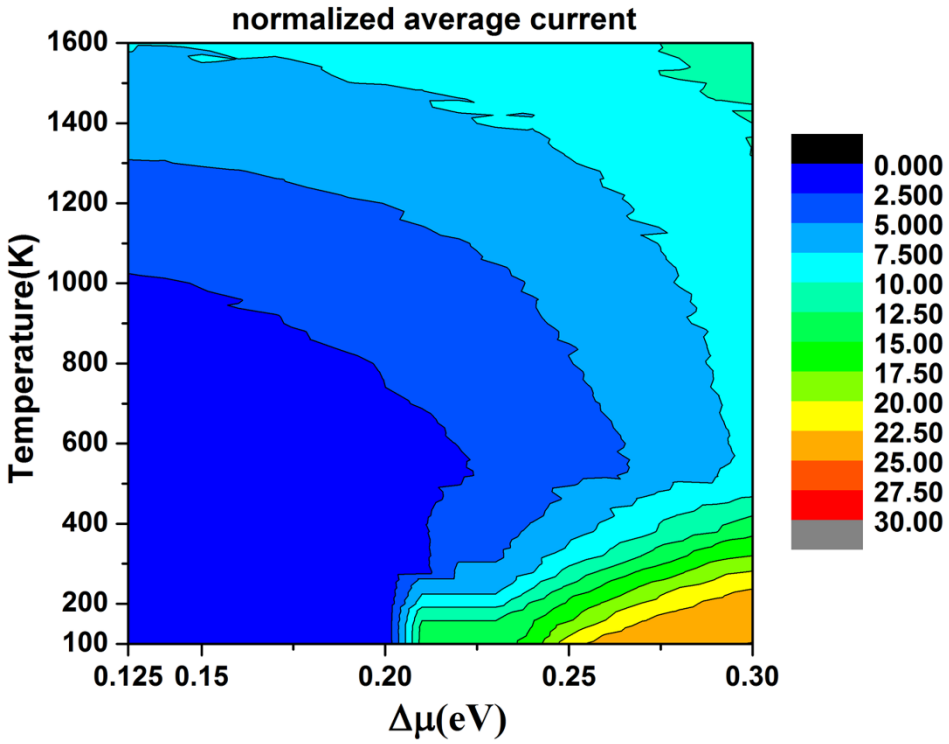

Figure 3.18. The calculated average current as a function of $\mu \equiv \mu(Pt) - \mu(Ni)$ and temperature. The corresponding surface structures can be found in Figure 3.8. The average currents on the 12×12(111) Pt/Ni(111) surfaces were predicted using on the volcano plot in Figure 3.15. All the average current values are normalized to that of a pure Pt(111) surface.

3.6 Rational design of Pt-Ni extended surfaces

Up to this point I have considered Pt/Ni(111) surfaces that are thermodynamically stable in different conditions. However in practice the surface of a catalyst may be metastable, making it important to evaluate the inverse question: if I could control the surface structure of a Pt_3Ni (111) catalyst, which structures would have optimal ORR activity? In this section, I explore principles for the rational design of surface structures with high ORR activity.

I have used Monte Carlo simulations based on the cluster expansions to search for the slab structures that maximize and minimize the average currents defined in Eq. (3.21). These simulations were run on the surfaces of 12×12(111) unit cells with 1/144 ML coverage of oxygen under a canonical ensemble with fixed composition of Pt_3Ni. ΔE_O at 1/144 ML coverage was corrected to that at 1/4 ML coverage by adding a constant shift of 18.8 meV as mentioned in the previous section. I also introduced a constraint that the first layer of the Pt_3Ni slab must be pure Pt skin because Pt-skin structures have been found to have an enhanced catalytic properties and stability.[48, 61, 65, 118] The middle layer of the 9-layer slab was fixed to be Pt_3Ni to mimic the existence of bulk Pt_3Ni underlying the surfaces.

The 12×12(111) surfaces identified to have maximal and minimal average currents can be reduced to 2x2(111) unit cells (Figure 3.19). Monte Carlo simulations on 2×2(111) unit cells identified the same two structures. The calculated average currents for these surfaces, as well as four others discussed in this chapter, are listed in Table 3.5. Although the surfaces listed in Table 3.5 were discovered using the cluster expansion, the oxygen binding energies

used to calculate the average currents were calculated directly using density functional theory (DFT). I have also included in this table the average current for the "ideal surface", a hypothetical surface on which the oxygen binding energies at all fcc sites are at the peak of volcano plot.

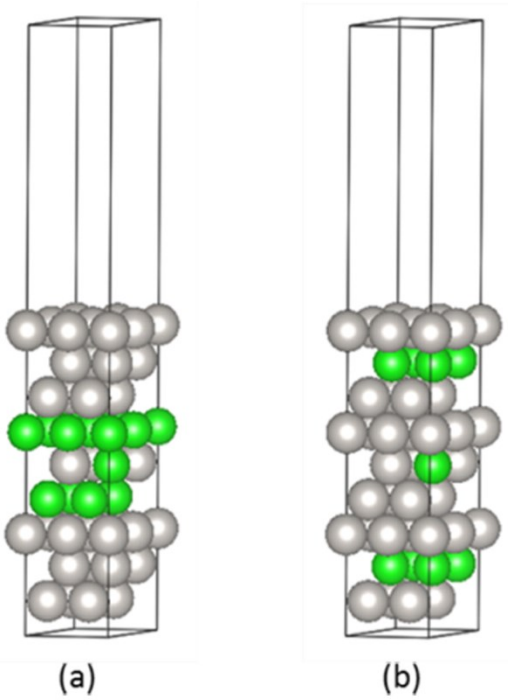

Figure 3.19. Stoichiometric Pt_3Ni (111) surfaces predicted to have maximum and minimum average currents. (a) 2×2(111) surface having pure Ni in the fourth layer with maximized average current, named $Pt_{27}Ni_9$-maxAvgCurrent, which has a three-layer Pt-skin; (b) 2×2(111) surface having pure Ni in the second layer with minimized average current, named $Pt_{27}Ni_9$-minAvgCurrent, which has a one-layer Pt-skin. Gray and green spheres represent the Pt and Ni atoms, respectively.

Table 3.5 Average currents, $\langle I \rangle$, which are normalized to that of a pure Pt(111) surface, and average oxygen binding energies for seven Pt/Ni(111) surfaces.

surface	average ΔE_O/eV	average current $\langle I \rangle$
ideal surface	1.716	96.0
Pt(111)	1.48	1.00
$Pt_{29}Ni_7$	1.80	52.3
$Pt_{25}Ni_{11}$	2.14	1.7E-2
$Pt_{27}Ni_9$-maxAvgCurrent	1.70	66.5
$Pt_{27}Ni_9$-minAvgCurrent	2.09	3.9E-2
$Pt_{27}Ni_9$	1.92	15.6

The surface that maximizes the average current, $Pt_{27}Ni_9$-maxAvgCurrent, has three-layer Pt-skin, and pure Ni in the fourth layer (Figure 3.19(a)). The average current of this surface is 66.5 times that of pure Pt(111), and 4.3 times that of the stoichiometric ground state $Pt_{27}Ni_9$ surface shown in Figure 3.7(b). The $Pt_{27}Ni_9$-maxAvgCurrent surface has an average current that is about 69% that of the "ideal surface", which indicates that its predicted ORR activity is nearly optimal. On the other hand, the surface that minimizes the average current has no Ni in the first, third and fourth layers but pure Ni in the second layer (Figure 3.19(b)). Its predicted average current is 3.9E-2 times that of pure Pt(111).

Although the composition, lattice parameter, and outermost surface layer of the best and worst surfaces are identical, the calculated average current of the best surface is 1700 times that of the worst. The first and third layers are pure Pt for both two structures, and the fifth layer is Pt_3Ni. The only difference between the two surfaces is that the lowest average current occurs with pure Ni in the second layer and pure Pt in the fourth layer, whereas the highest average current occurs when these two sub-surface layers are swapped. This result suggests that by tuning the sub-surface atomic order, with fixed lattice constant and composition, it is possible to modify the specific activity for the ORR by three orders of magnitude.

It is worth considering these results in the context of stability. As discussed in the work of Wang et al.,[35] Ni atoms close to the surface (and Ni atoms that are all next to each other) are vulnerable to dissolution, and Ni atoms within Pt-Ni alloy surfaces can be stabilized through the use of a multi-layer Pt skin on the surface. I predict that for an extended Pt_3Ni surface, the same multi-layer Pt skin surfaces (as shown in Figure 3.19(a)) that prevent

nickel dissolution may enhance the ORR activity. However these surfaces are likely to be thermodynamically unstable.

3.7 Summary and discussion

Pt-Ni alloys have the potential to significantly decrease the cost of ORR catalysts through a combination of increased specific activity with decreased Pt content. My calculations for a prototypical system, the extended $Pt_3Ni(111)$ surface, paint a complicated picture of the structure, activity, and stability of Pt-Ni surfaces. Key findings based on the cluster expansion built on 2-dimensinal extended surfaces in this chapter are as follows.[92]

For thermodynamically stable Pt-Ni surfaces, firstly, I found that the window of $\Delta\mu \equiv \mu(Pt) - \mu(Ni)$, where bulk Pt_3Ni is stable is between 0.125 and 0.294 eV (Figure 3.6). Within this window, for a 9-layer slab (2×2(111) super cell), three equilibrium surfaces are identified: $Pt_{29}Ni_7$, $Pt_{27}Ni_9$, and $Pt_{25}Ni_{11}$ with the second-layer Ni composition of 50 %, 75 % and 100 %, respectively. Secondly, I predict that a variety of surface structures, most of which are off-stoichiometric, are thermodynamically stable in different chemical environments. As a validation of these predictions, the composition profile of 12×12(111) slab with overall composition of $Pt_{1000}Ni_{296}$ predicted by my calculations (Figure 3.9) is 100% Pt, 48.2% Pt, 86.3% Pt, 75.3% Pt, and 75% compositions in the outmost, second, third, fourth, and fifth layers respectively, which is in excellent agreement with experiment (layer-by-layer).[53]

Although I predict that the surface of the catalytically active material likely has a Pt skin, in agreement with experiment, I also predict significant substitutional disorder in the second (and to a lesser extent third) layer of the surface. Because of this sub-surface disorder, the oxygen binding energies on different fcc sites on the same surface are

predicted to vary by more than 300 meV, resulting in about three orders of magnitude difference in contribution of each site to the experimentally observed specific activity. For the thermodynamically stable Pt_3Ni surface, the predicted specific activity (calculated by averaging over all sites) is 7.8 times than that of pure Pt(111)(Figure 3.17), which is close to the experimentally-observed value of 10 times.[53]

My model suggests that there is still room for improvement upon the excellent catalytic activity demonstrated by Stamenkovic et al.[53] Among surfaces that are thermodynamically stable at some combination of temperature, $\mu(Ni)$, and $\mu(Pt)$, a well-ordered Pt-rich surface is predicted to have the highest catalytic activity (Figure 3.18). The specific activity of this surface, relative to pure Pt, is predicted to be about five times that of the Pt_3Ni surface characterized by Stamenkovic et al.[53]

For thermodynamically unstable Pt-Ni surfaces, firstly, as shown in Figure 3.14, with the outmost layer fixed as Pt-skin structure, under both grand canonical ensemble and mix ensemble, the Pt atoms in the inner layers of Pt-Ni slabs are pull to the second layer as the coverage of oxygen on the surface increases. This tells us that the oxygen adsorption on the metastable Pt_3Ni surfaces with Pt-skin may lead to second layer to be Pt-rich, which will likely improve the activity of Pt_3Ni surfaces according to Figure 3.9 and Figure 3.17.

For the oxygen binding energy, with fixed lattice constant, fixed Pt-skin, and overall compositions of extended surfaces (75 % Pt), the difference of local Pt/Ni atomic order can give us a difference of oxygen binding energy of 553 meV between the maximal and minimal ΔE_O, which corresponding to the 1700 times of site-specific computational current in ORR (Figure 3.19 and Table 3.5). Among all Pt_3Ni surfaces, I predict that it is possible to achieve a nearly seven-fold improvement in specific activity over the best-performing

Pt(111)-skin surfaces[53], which would be close to the peak of the volcano plot (Figure 3.19(a)). This highly active surface has the added benefit in that the three outermost layers are pure Pt, suggesting that it would be particularly stable against nickel dissolution. However I note that the trends in activity of surfaces near the peak of the volcano plot are sensitive to the exact position of the peak.

In summary, in this chapter, I predict that at the surface composition used in reference 53, it would be possible to achieve a higher specific activity by having a more well-ordered Pt_3Ni surface (in equilibrium at lower temperatures) or a more disordered Pt_3Ni surface (in equilibrium at higher temperatures). Unfortunately, Ni segregation at high temperatures and kinetic trapping in a disordered state at lower temperatures may make it difficult to realize these theoretical gains in activity in practice.

I have demonstrated that the cluster expansion approach, widely used for bulk materials, can provide valuable insights into heterogeneous catalysis and facilitate rational catalysts design in the extended surfaces. Also, the explicit inclusion of training structures with monolayer of oxygen/vacancy group (Figure 3.3) on the extended surfaces allows us to accurately and rapidly predict the oxygen binding energy, which enables the search of metastable surfaces with optimal ORR activity via Metropolis Monte Carlo simulations. Moreover, the use of Bayesian cluster expansions makes the generation of highly accurate surface models feasible with a practical number of training structures.

Chapter 4

Cluster expansion approach on Pt/Ni/Mo nanoparticles

4.1 Introduction of Pt-Ni octahedral nanoparticles

The sluggish kinetics of the oxygen reduction reaction (ORR) on Pt and Pt-based alloy catalysts and low catalyst durability are major limitations for the use of these catalysts in proton-exchange membrane (PEM) fuel cells. The catalytic properties of Pt and Pt-based alloy catalysts have been investigated extensively by experimental[34-35, 38, 43, 45] and computational[46-51] methods, and it has been demonstrated that Pt_3Ni alloys have a much higher ORR activity than pure Pt.[50, 52-53] However Pt-Ni catalysts suffer from degradation under fuel cell operating conditions due to the dissolution of Ni atoms.[54, 59-60] It has recently been shown that the stability of Pt-Ni nanoparticles can be improved by doping with a third element. Mo-doped octahedral Pt_3Ni nanoparticles (Mo-Pt_3Ni/C) were reported to have much greater stability than undoped particles, with 81 times higher specific activity and 73

times higher mass activity than commercial Pt/C catalysts.[54] Recently, Beermann et al.[60] reported that Rh-doped Pt-Ni octahedral nanoparticles have improved shape stability compared with Pt-Ni octahedral nanoparticles. It is also possible to take advantage of the preferential dissolution of Ni from Pt-Ni nanoparticles to synthesize new nanocatalysts with high surface area. can be synthesized with Pt-rich edges and Ni-rich facets,[58-59, 141] and the dissolution of Ni from facets of these nanoparticles can leave behind concave octahedra[59] or nanoframes[58] with enhanced catalytic activity.

Despite the considerable interest in Pt-Ni nanoparticles, their structure and stability at the atomic scale are not fully understood, in part because of the limitations of experimental methods and computational models. Density functional theory (DFT)[14-16] has demonstrated predictive accuracy for a variety of materials problems,[142] but it is prohibitively expensive to directly use DFT calculations to calculate the properties of a large number of nanoparticles at experimentally relevant sizes (about between 4 – 20 nm[54, 59-61, 63-68]). An alternate approach is to use cluster expansions[1] parameterized by density functional (DFT) calculations to model nanoparticles. The resulting cluster expansions typically have accuracy close to that of DFT (within about 5 meV / atom) and are capable of evaluating the energies of millions of nanoparticle structures per minute. This approach has been used to model internal atomic arrangements in alloy nanoparticles with fixed shape and diameters of no more than about 2 nm.[27-28, 69-71] We have previously demonstrated that it is possible to extend the cluster expansion approach to predict the shapes and properties of larger single-component[26] and alloy[54] particles by training cluster expansions on the DFT-calculated energies of small (~1 – 2 nm) particles. This approach, described in more detail in the Methods section, makes it possible to quickly and accurately predict the energies of

multi-nanometer alloy nanoparticles as a function of shape, size, composition, and internal atomic order. In this chapter, I present the use of this method in a quaternary Pt-Ni-Mo-Vacancy cluster expansion to investigate the atomic structure and stability of Pt-Ni nanoparticles and determine the likely reasons for the exceptional stability of Mo-doped particles.[54]

4.2 Building cluster expansions for nanoparticles

4.2.1 Details of DFT Calculations

Density functional theory (DFT) calculations[14, 97] were done using the Vienna Ab-initio Software Package (VASP)[102-103] with the revised Perdew-Burke-Eznerhof (RPBE) exchange-correlation functional.[93-95] All DFT calculations were run with spin-polarization enabled. The Mo_pv, Ni, Pt_pv_GW, O_GW, and H_GW PBE projector-augmented wave (PAW)[101] potentials provided with VASP were used, and VASP was run with high precision. A single *k*-point at the center of the Brillouin zone was used for each nanoparticles. For bulk materials, a 16×16×16 k-point grid was used for an fcc unit cell, and the k-point grid was scaled appropriately for larger cells. Second-order Methfessel-Paxton smearing[104] with a width of 0.2 eV was used to set partial occupancies. Real-space projectors were used to evaluate the non-local part of the PAW potential. The convergence criteria for the electronic self-consistent iteration and the ionic relaxation loop were set to be 0.1 meV and 1 meV per unit cell, respectively.

4.2.2 Cluster expansion for nanoparticles in vacuum

Although cluster expansions have been used previously to model the shapes[26, 143] or internal atomic arrangements[27, 69, 71, 144] in nanoparticles separately, to my knowledge, the use of a single cluster expansion to predict the energies of nanoparticles as a function of shape, size, and internal atomic order was firstly introduced in our work of Huang et al.[54] I briefly summarize this approach of the cluster expansion here. A quaternary cluster expansion was generated on an fcc lattice in which each site could be occupied by molybdenum (Mo), nickel (Ni), platinum (Pt), or a vacancy. Site variable values of 0, 1, 2, and 3 respectively were assigned to these species. A discrete cosine basis was used to generate the cluster functions, where the b^{th} basis function of the site variable s is given by

$$\Theta_b = \begin{cases} 1 & \text{for b = 0} \\ \sqrt{2}\cos(\pi b(2\text{s} + 1) / 8) & \text{for b > 0} \end{cases}, \tag{4.1}$$

for $b \in \{0,1,2,3\}$.

A training set with 243 structures were created for the purpose of fitting ECIs of cluster expansion through Bayesian approach.[21] The strategy of creating the training set are provided as follows. To create the initial 136 structures used for the training data, a "dummy" cluster expansion was generated, consisting only of nearest-neighbor pair clusters, with effective cluster interactions (ECI) chosen in a way that assigned a value of -1 eV to atom-

atom interactions (regardless of the species involved) and no energy to other interactions. These cluster expansions were used in Monte Carlo simulations at 2000 – 4500 K to generate random snapshots of nanoparticles. Two different sets of random nanoparticles were created. The first set of nanoparticles contained only Ni and Pt, where the numbers of Pt and Ni atoms were independently and randomly selected from a uniform distribution over all integers from 0 to 100. The second set of nanoparticles contained Mo, Ni, and Pt, where the numbers of Mo, Ni, and Pt atoms were independently and randomly selected from uniform distributions over integers from 0 to 10, 0 to 50, and 0 to 150 respectively. All nanoparticles were generated under the constraint that there had to be more than 100 total atoms in the nanoparticle, as the inclusion of smaller particles was found to lead to cluster expansions with poor predictive accuracy for multi-nanometer nanoparticles (potentially due to quantum size effects). Nanoparticles that experienced significant reconstruction upon relaxation, defined as an atom traveling more than 75% the nearest-neighbor distance from its initial site, were excluded. These particles accounted for about 20% of the random structures generated. All nanoparticles were contained in a cubic cell with a lattice parameter of 28.8 Å, which is actually an 8×8×8 super cell with respect to the unrelaxed conventional fcc unit cell. The resulting set of random nanoparticles included 74 Ni-Pt nanoparticles and 62 Mo-Ni-Pt nanoparticles. In addition to these structures, the training data consisted of the pure elements Mo, Ni, and Pt in a bulk fcc crystal, vacuum (a lattice containing only vacant sites), and various low-energy structures predicted over the course of this research, for a total of 243 unique structures. To reduce the prediction error of the cluster expansion, the pure elements and vacuum were included twice in the training set.[76] For the total number of training structures (243), there are 159 Pt-Ni-Mo

nanoparticles, 76 Pt-Ni nanoparticles, 3 Pt-Mo nanoparticles, 1 pure Pt nanoparticle, 1 Pt bulk, 1 Ni bulk, 1 Mo bulk and 1 vacuum structure. The effective cluster interactions (ECIs) of the cluster expansion were fit to the DFT-calculated formation energies of fully relaxed nanoparticles relative to these reference states (bulk fcc Mo, Ni and Pt).[109]

In practice, the ECIs for clusters that contain a large number of sites or sites that are far apart are usually negligible, allowing for the expansion to be truncated to a sum with a finite number of ECIs with little loss of accuracy. In this chapter for Pt-Ni and Pt-Ni-Mo nanoparticles, the cluster expansion was truncated to include the empty cluster, the one-body (point) cluster, all 2-body clusters up to the fourteenth-nearest neighbor, all 3-body clusters up to the fifth-nearest neighbor, all 4-body clusters up to the third-nearest neighbor, and all 5-, and 6-body clusters up to the second-nearest neighbor, for a total of 1356 symmetrically distinct cluster functions. The ECIs for these cluster functions were fit to the training data using the Bayesian approach[21] with a multivariate Gaussian prior distribution.[13] The inverse of the covariance matrix for the prior, Λ, was diagonal, with elements given by the orbit regularization parameter $\lambda_{\alpha\alpha}$ and coupled regularization parameter $\lambda_{\alpha\beta}$ defined in Eq. (2.16) and Eq. (2.17). The parameters λ_1, λ_2, λ_3, and λ_4 were determined by using a conjugate gradient algorithm to minimize the root mean square leave-one-out cross validation (RMS LOOCV) score, an estimate of prediction error.[18] The final values for these parameters were 1.000×10^{-8}, 9.424×10^{-12}, 4.421, and 3.048 respectively. The resulting cluster expansion had a RMS LOOCV error of 3.9 meV per atom relative to DFT calculations.

4.2.3 Cluster expansion for nanoparticles in oxidizing conditions

For the extended surfaces as I demonstrate in Chapter 3, I am able to simulate oxidizing conditions by adding a monolayer of oxygen/vacancy sites on the top of slab so as to build a cluster expansion that enables the prediction of oxygen binding energies (ΔE_O) on Pt-Ni alloy surfaces.[92] However, in this chapter such an approach is not straightforward for the cluster expansions built on nanoparticles, in which the size and shape of the nanoparticle surface (and hence the list of possible adsorption sites) can change. Thus, cluster expansions built on clean nanoparticles in vacuum conditions are unable to predict the change in nanoparticle structure and properties as a function of applied potential or oxygen chemical potential. But for an ORR catalyst, it is necessary to take into account the likely presence of oxidizing adsorbates on the surface. The effect of the adsorbates depends primarily on the type and chemical potential of adsorbates, the local atomic structure near the adsorption site, and the applied potential. For this reason, I have adopted a simpler approximation to estimate the effect of an oxidizing environment for the nanoparticles. Here, in this subsection, I demonstrate my approach to build cluster expansion on nanoparticles in oxidizing conditions as follows.

To investigate the structural behaviors of the experimentally-observed nanoparticles (with size of 4.2 nm in edge length) in oxidizing conditions, I extended the cluster expansion model to include a site-specific and metal-specific correction term to each surface site occupied by a Pt/Ni/Mo atom. These correction terms are calculated by accounting for the change of free energy of the nanoparticle due to the possible presence of adsorbed oxygen

atoms (*O) or hydroxyl groups (*OH) on the surface of small $Pt_{178}Ni_{41}Mo_6$ nanoparticles (Figure 4.1). Even though these 225-atom nanoparticles (~2 nm in diameter, as shown in Figure 4.1) are much smaller than the experimentally-observed nanoparticles (4 – 20 nm), but they retain key structural features of the synthesized Mo-doped Pt_3Ni nanoparticles in reference 54 and are small enough to be modeled using density functional theory (DFT) calculations. These correction terms depend on the surface site position, the occupied metal element, and the applied potential (or oxygen chemical potential). For the site dependence, I separate all of the surface sites of nanoparticles into six distinguished types as shown in Figure 4.2. I set the applied potential as 0.95 V, which is widely used in recent experimental measurement of ORR activity.[54, 58, 61, 145-147] I then used DFT to calculate the free energy change of nanoparticles due to the adsorption of *O and *OH on the six different types of sites of the 225-atom nanoparticles (Figure 4.2(a)) when each surface site is occupied by a Pt, Ni, or Mo atom.

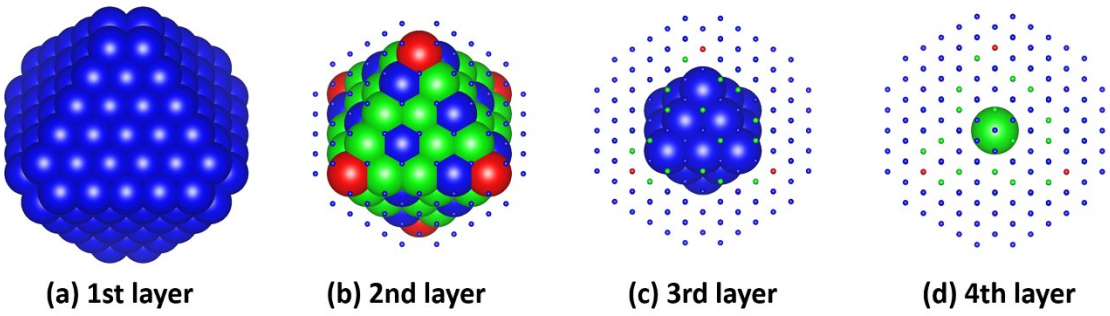

Figure 4.1. Ground state structure of $Pt_{178}Ni_{41}Mo_6$ nanoparticle predicted by the cluster expansion in vacuum using a simulated annealing algorithm that simultaneously optimized the particle shape and internal atomic order. The (a) first, (b) second, (c) third, and (d) fourth layers. Blue spheres represent Pt, green represent Ni, and red represent Mo. Small spheres represent the positions of atoms in the outer layers. Replacing all six Mo atoms on the sub-surface vertex sites with Ni atoms gives the $Pt_{178}Ni_{47}$ nanoparticle referenced in the text.

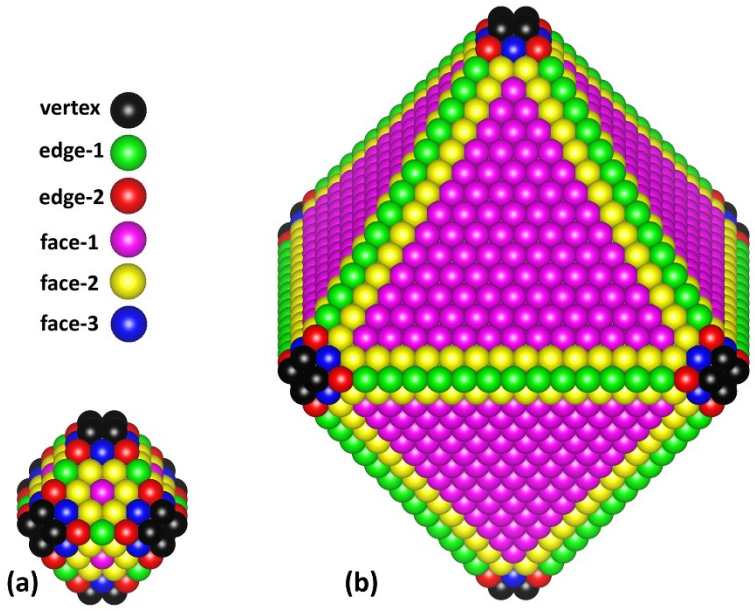

Figure 4.2. The six different types of surface sites by their distinguished positions on (a) a 225-atom nanoparticle and (b) a 4.2-nm nanoparticle with 4573 atoms. The separation of surface sites is as follows: (1) vertex: a vertex site; (2) edge-1: an edge site that is not a nearest neighbor to a vertex site; (3) edge-2: an edge site that is a nearest neighbor to a vertex site; (4) face-1: a (111) facet site that is neither a nearest neighbor to an edge site nor to a vertex site; (5) face-2: a (111) facet site that is a nearest neighbor to an edge site but not to a vertex site; (6) face-3: a (111) facet site that is a nearest neighbor to both an edge site and a vertex site. All sites on nanoparticles can be occupied by Pt, Ni or Mo atoms. The six different colors represent six types of sites: black, green, red, pink, yellow, and blue represent vertex, edge-1, edge-2, face-1, face-2, and face-3 surface sites, respectively.

In both of the work of Huang et al.[54] and the work of Liu et al.[148], Mo on the surface of nanoparticles exhibits mainly Mo(VI) and Mo(IV) oxidation states. Thus, I calculated the free energy change of Mo with two adsorbed atomic oxygen (2*O) and Mo with three adsorbed atomic oxygen atoms (3*O). Then I chose the adsorbate with the lower free energy change as the adsorbate for surface Mo. For surface Pt/Ni atoms, I chose the lower of the free energies for *O and *OH.

I used the computational hydrogen electrode (CHE) model[55] to determine the free energy values for *O and *OH for Pt/Ni, and 2*O and 3*O for Mo. The free energies are referenced to the corresponding clean nanoparticles in vacuum (without adsorbates) and H_2O (gas-phase H_2O at 0.035 bar is chosen as the reference state since gas-phase H_2O at this pressure is in equilibrium with H_2O(l) at 300 K[149]). The details of free energy calculations of *O, 2*O, 3*O, and *OH are as follows.

The four reactions correspond to *O, 2*O, 3*O, and *OH are:

$$*O + 2(H^+ + e^-) \rightarrow H_2O \tag{4.2}$$

$$2*O + 4(H^+ + e^-) \rightarrow 2H_2O \tag{4.3}$$

$$3*O + 6(H^+ + e^-) \rightarrow 3H_2O \tag{4.4}$$

$$*OH + (H^+ + e^-) \rightarrow H_2O \tag{4.5}$$

Under the CHE model, let us take 3*O as an example to show the calculation of $\Delta G(3*\mathrm{O})$ on one surface Mo atom:

$$\begin{aligned}&\Delta G[3*\mathrm{O} + 6(\mathrm{H}^+ + \mathrm{e}^-) \rightarrow 3\mathrm{H_2O}] \\ &= \Delta E[3*\mathrm{O} + 6(\mathrm{H}^+ + \mathrm{e}^-) \rightarrow 3\mathrm{H_2O}] + (\Delta ZPE - T\Delta S)[3*\mathrm{O} + 6(\mathrm{H}^+ + \mathrm{e}^-) \rightarrow 3\mathrm{H_2O}] - 6\mathrm{e}U,\end{aligned} \tag{4.6}$$

where $\Delta E[3*\mathrm{O} + 6(\mathrm{H}^+ + \mathrm{e}^-) \rightarrow 3\mathrm{H_2O}]$ is the reaction energy, calculated by DFT, and ΔZPE is the difference in zero-point energies due to reaction, ΔS is the change in entropy, and U is the value of applied potential. The values of ΔZPE and $T\Delta S$ are shown in Table

4.1. The expression of $\Delta E[3*O+6(H^{+}+e^{-})\rightarrow 3H_2O]$ is as follows:

$$\begin{aligned}&\Delta E[3*O+6(H^{+}+e^{-})\rightarrow 3H_2O]\\&=E_{DFT}(3*O)+3E_{DFT}(H_2(g))-E_{DFT}(*)-3E_{DFT}(H_2O),\end{aligned} \tag{4.7}$$

where $E_{DFT}(3*O)$ is the DFT energy of nanoparticle with three oxygen atoms adsorbed on a surface Mo atom, $E_{DFT}(*)$ is the DFT energy of corresponding clean nanoparticle, $E_{DFT}(H_2(g))$ is the energy of gas-phase hydrogen, and the $E_{DFT}(H_2O)$ is the energy of a water molecule. The DFT calculations of adsorbed *O, 2*O, 3*O and *OH on the surface of nanoparticles are done in vacuum. In order to take the effects of solvation at the water-solid interface into account, I include solvation correction values for *O (zero eV) and *OH (-0.6 eV, stabilized due to exposure to liquid water).[56]

Table 4.1. The entropy and zero-point energy contributions to the free energy, which are from the work of Norskov et al.[55] The gas-phase values are from Physical Chemistry[150], and the values for *OH and *O are from DFT calculations on Cu(111) surface in the work of Kandoi et al.[151] For the state of H_2O, gas-phase H_2O at 0.035 bar is chosen as the reference state since gas-phase H_2O at this pressure is in equilibrium with H_2O(l) at 300 K.[149]

	TS (eV)	*ZPE* (eV)	*ZPE-TS* (eV)	$\Delta ZPE - T\Delta S$ (eV) (referenced to H_2O)
H_2O	0.67	0.56	-0.11	0
*OH+1/2H_2	0.20	0.44	0.24	0.35
*O+H_2	0.41	0.34	-0.06	0.05

One critical factor about the adsorption energy is that for the same surfaces site, the change of free energy upon adsorption will vary according to the local atomic order near the adsorption site. Considering this factor, it is meaningful and important for us to quantify the variance of the free energy change on the same surface site type, but with different neighboring atomic orders. In this chapter, for each Pt/Ni/Mo surface site type on the 225-atom nanoparticle (Figure 4.2(a)), I used DFT to calculate adsorption energies and free energy changes due to the presence of adsorbates ($\Delta G(*\mathrm{OH}/3*\mathrm{O})$) on three different local atomic configurations. For example, the three different atomic configurations I used for the surface face-1 site type (Figure 4.2(a) with pink color) when it is occupied by Ni atom are shown in Figure 4.3.

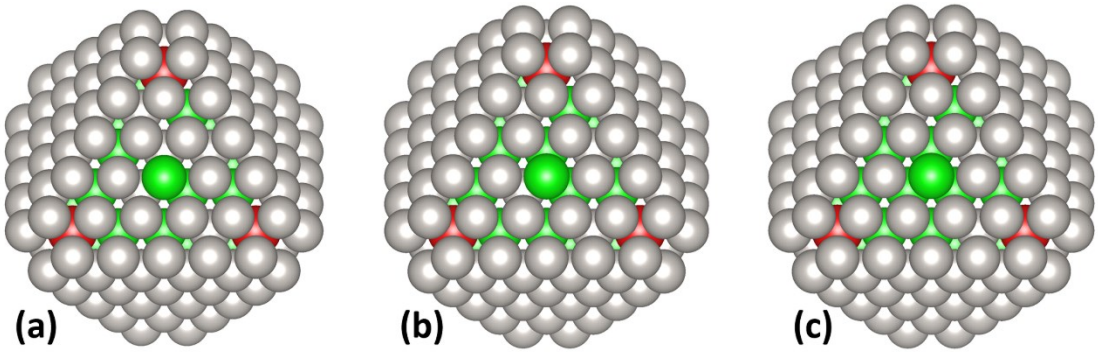

Figure 4.3. The three different atomic configurations near the surface face-1 Ni site, which is defined in Figure 4.2 (a) with pink color. For the surface Ni atom, its three nearest-neighbor atoms in the second layer of nanoparticles are different. (a) There are one Ni atom and two Pt atoms; (b) there are two Ni atoms and one Pt atom; and (c) there are three Ni atoms.

With all of the above discussion taken into account, at an applied potential of 0.95 V ($U = 0.95\ V$), the free energy changes on surface due to 2*O and 3*O adsorbed on a Mo atom are calculated based on Eq. (4.6), and similarly for Pt and Ni due to adsorbed *O and

*OH. According to DFT calculations, for all Mo surface sites, 3*O has a lower free energy than 2*O, so we chose 3*O as the adsorbate on Mo surface atom. For all Pt and Ni surface sites, *OH has a lower free energy than *O, so I chose *OH as the adsorbate on Pt/Ni surface atom. Thus, to approximate the effect of oxidizing conditions, I assume that each surface Mo atom is bound to three oxygen atoms (3O) and each surface Ni or Pt atom is bound to a single hydroxyl group (OH).

Although the exact change in the free energy of a surface atom in the presence of adsorbed O/OH ($\Delta G(\text{*OH}/3\text{*O})$) depends on the atomic structure in the neighborhood of the adsorption site, I found that approximate values for $\Delta G(\text{*OH}/3\text{*O})$ could be determined by considering whether the adsorbate was bound to one of six types of sites: 1) a vertex site, 2) an edge site not next to a vertex site, 3) an edge site next to a vertex site, 4) a face site next to only face sites, 5) a face site next to only edge sites and face sites, or 6) a face site next to an vertex site. Every site on the surface of the nanoparticles I studied falls into one of these six types (Figure S2). For each site type, the spread of calculated $\Delta G(\text{*OH}/3\text{*O})$ values and error bar are shown in Figure 4.4. The calculated averages and standard deviations of $\Delta G(\text{*OH})$ for Pt and Ni surface atoms, and those of $\Delta G(3\text{*O})$ for Mo surface atoms are listed in Table 4.2. The standard deviation of $\Delta G(\text{*OH}/3\text{*O})$ at each type of site ranges from a minimum of 13 meV to a maximum of 134 meV with an average of 74 meV over all metals and site types (Table 4.2). This value gives a rough estimate of the magnitude of the error (relative to DFT calculations) that is introduced by this method, in addition to the estimated error of 3.9 meV per atom due to the cluster expansion in vacuum. Thus I approximate the effects of an oxidizing environment on the

structure and properties of an alloy nanocatalyst by applying to each surface site an energetic correction term that depends only on the type of site and the element present at the site. I denote the corresponding correction terms as $\Delta G(3^*O)$ for Mo and $\Delta G(^*OH)$ for Pt and Ni.

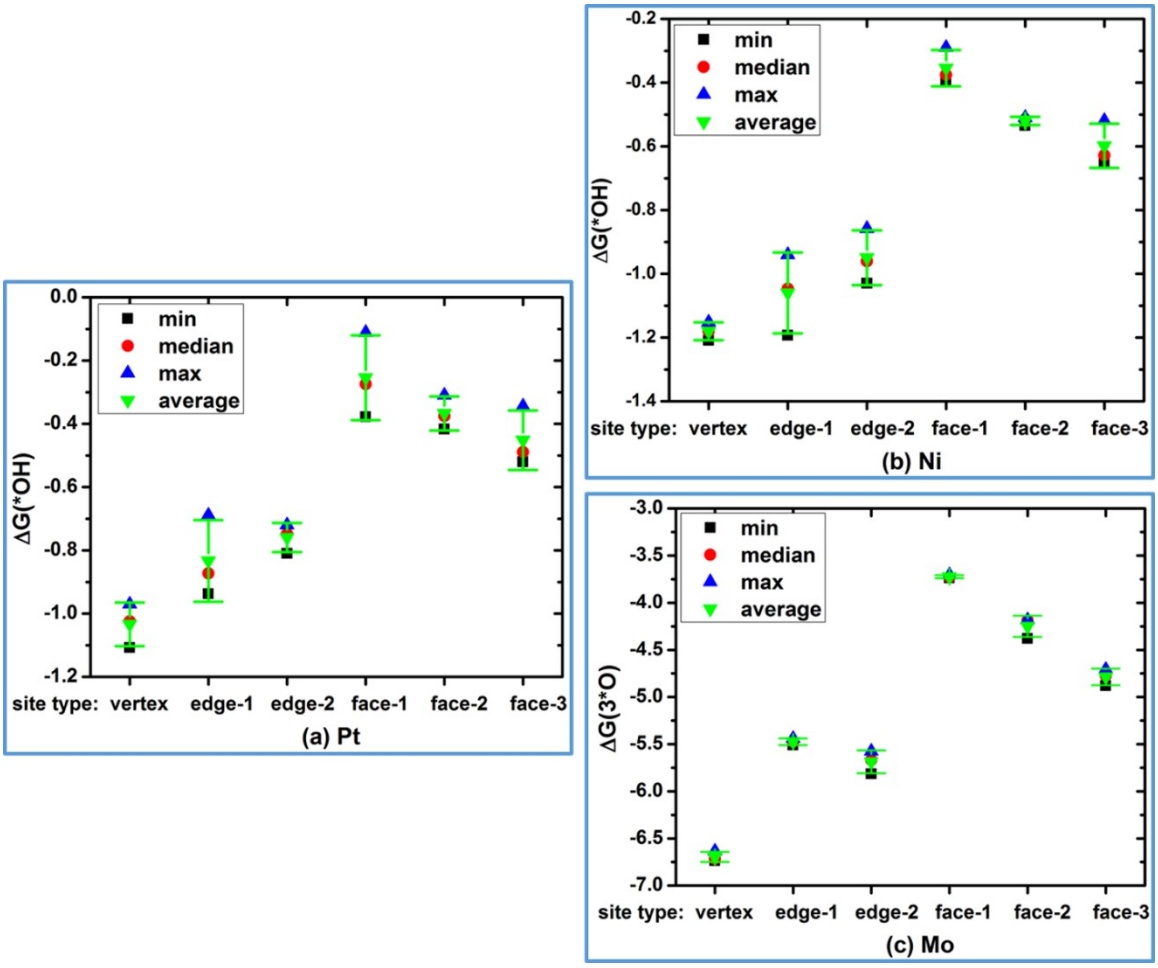

Figure 4.4. In oxidizing conditions (at an applied potential of 0.95 V), the DFT-calculated changes of free energies for all six types of surface sites defined in Figure 4.2 occupied by Pt/Ni/Mo atom due to adsorption of *OH on (a) Pt, (b) Ni, and adsorption of 3*O on (c) Mo. Error bars refer to the standard deviation of $\Delta G(^*OH/3^*O)$ values of three different local atomic configurations for each site type.

Table 4.2. The averages and standard deviations of ΔG(*OH/3*O) on surface Pt/Ni/Mo atoms. Here, stdev means the standard deviation. The average of all eighteen values of standard deviations is 74 meV.

surface site	ΔG(*OH) on Pt/eV		ΔG(*OH) on Ni/eV		ΔG(3*O) on Mo/eV	
	average	stdev	average	stdev	average	stdev
vertex	-1.034	0.069	-1.180	0.028	-6.695	0.053
edge-1	-0.833	0.129	-1.060	0.127	-5.475	0.035
edge-2	-0.759	0.046	-0.949	0.086	-5.687	0.120
face-1	-0.254	0.134	-0.354	0.057	-3.723	0.016
face-2	-0.367	0.054	-0.520	0.013	-4.250	0.113
face-3	-0.451	0.094	-0.598	0.069	-4.787	0.087

For Mo atoms at vertex sites, it is necessary to consider the situations in which two Mo atoms are on diagonal (Figure 4.5 (a)) or adjacent vertex sites (Figure 4.5 (b)). There are penalty terms for these two situations because of the strongly repulsive interactions between the oxygen atoms adsorbed on the Mo, which are energetically unfavorable. DFT calculations determined that the penalty terms are 0.725 eV for two Mo atoms on diagonal vertex sites, and 1.885 eV for two Mo atoms on adjacent vertex sites. The magnitude of the penalty for Mo atoms on adjacent vertex sites effectively precludes this configuration from occurring at the temperatures considered in this chapter. I note that it was not necessary to calculate a similar penalty for Mo atoms on adjacent edge sites, as that configuration almost never appeared in Monte Carlo simulations.

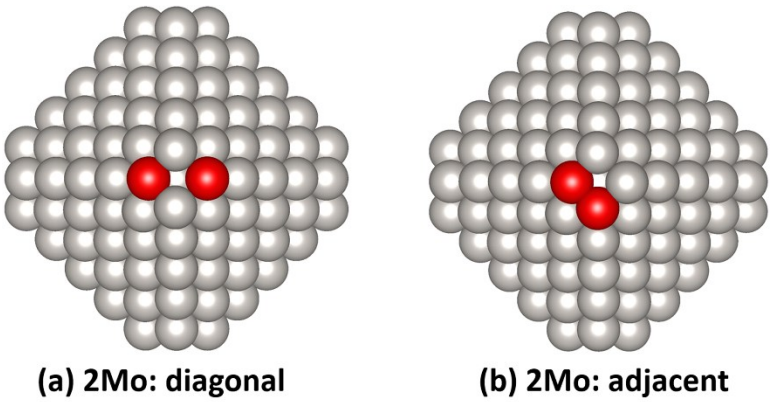

Figure 4.5. Two Mo atoms at (a) diagonal and (b) adjacent vertex sites. Red spheres represent Mo. Grey spheres can be occupied by Pt or Ni atom.

4.3 Surface structures and stability of Pt-Ni nanoparticles

Because the (111) surface is the most catalytically active surface and octahedral nanoparticles with high (111) surface area have been shown to have high catalytic activity,[54] in the following sections I focus on particles that are nearly perfect octahedra, consistent with those synthesized in reference 59 and 54. Provided that the six vertex atoms on perfect octahedra are particularly unstable due to their low coordination, I removed these atoms and performed Monte Carlo simulations on slightly truncated octahedral nanoparticles (e.g. Figure 4.2 and Figure 4.6).

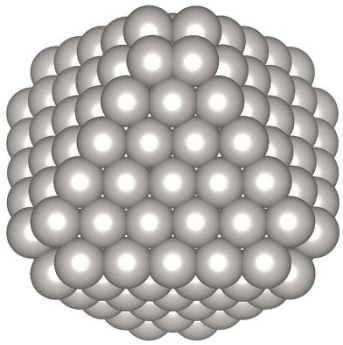

Figure 4.6. The shape of the prototypical 225-atom nanoparticle with six vertex atoms removed (only one atom at each end of particle edge is removed). Grey spheres can be occupied by Pt, Ni or Mo atoms.

The equilibrium structures of an alloy nanoparticle depend not only on its overall composition and chemical environment, but on its size as well.[152-154] To identify how size affects the structures of nanoparticles at a fixed composition, a series of Monte Carlo simulations[109], using a cluster expansion Hamiltonian, were run on slightly truncated

octahedral Pt_3Ni nanoparticles with different sizes. The simulations were run at 443 K, which is the temperature at which the Pt3Ni and Mo-Pt3Ni nanoparticles were annealed in reference 54 and is close to the annealing temperature of 393 K in reference 59. As shown in Figure 4.7, across all particle sizes, the outermost layer is predicted to be nearly 100% Pt, resulting in an excess of Ni throughout the rest of the particle. This excess Ni primarily resides in the second layer, fourth layer, and the layers deeper than the fifth layer. At small particle sizes, the third and fifth layers have excess Pt, likely due to the excess Ni in the second and fourth layers and the relative favorability of Pt-Ni nearest-neighbor bonds.

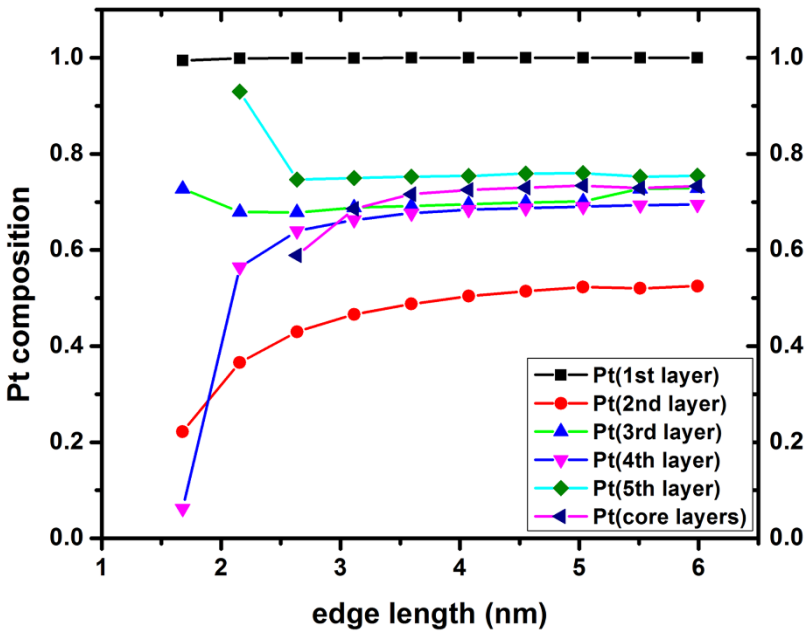

Figure 4.7. Layer-by-layer composition profile for octahedral Pt_3Ni nanoparticles with varying edge length at 443 K. "Core layers" represent all layers deeper than the fifth layer.

As the size of the nanoparticles increases, the composition profile for each layer is nearly converged at a size of around 4 nm in edge length (Figure 4.7), which is approximately the size of the Ni-Pt and Mo-Ni-Pt particles studied by Huang et al.[54] To enable comparison

with experimental results and limit the effects of particle size on the composition profile, I have used truncated 4573-atom nanoparticles with edge lengths of approximately 4 nm as prototypical particles for more in-depth study in Monte Carlo simulations. The shape of these particles is shown in Figure 4.2(b) and Figure 4.8, which is a snapshot structure of Pt_3Ni ($Pt_{3398}Ni_{1175}$) nanoparticles at 443 K in vacuum.

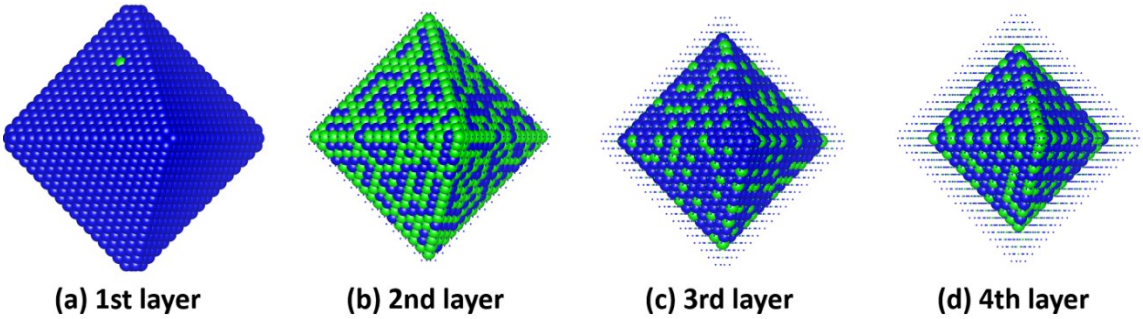

Figure 4.8. The (a) first, (b) second, (c) third, and (d) fourth layers of a representative Pt_3Ni nanoparticle ($Pt_{3398}Ni_{1175}$) taken from a Monte Carlo simulation at 443 K. Blue spheres represent Pt and green represent Ni. Small spheres represent the positions of atoms in the outer layers.

The best-performing Pt-Ni catalysts have a Pt-skin structure, in which the outermost layer is pure Pt.[53] However as a particle becomes more Ni-rich, it can be expected that the Pt skin will be lost. I have calculated the layer-by-layer composition of the prototypical 4573-atom nearly octahedral nanoparticles as a function of the overall particle composition (Figure 4.9). The equilibrium atomic order of Pt-Ni nanoparticles depends on the overall particle composition. I predict that in equilibrium at both 443 K and room temperature (298 K) the nanoparticle core transitions from a layered $L1_0$ structure near a composition of PtNi to a cubic $L1_2$ structure near a composition of Pt_3Ni, with the transition occurring

near a composition of Pt_3Ni_2 (Figure 4.9 and Figure 4.10). This is in excellent agreement with previous experimental[135, 155] and computational[135, 156] results on bulk Pt-Ni alloys. I note that the transition from the tetragonal $L1_0$ core to the cubic $L1_2$ core with increasing Pt content may affect the catalytic properties of the nanoparticle, which I do not investigate here. Atomic disorder increases with increasing temperature and increasing distance from the particle center (Figure 4.8 and Figure 4.10), consistent with my results on an extended Pt_3Ni (111) surface.[92] I predict that the equilibrium nanoparticle surface is effectively Pt skin, defined here as having a surface composition of more than 99.8% Pt, at 443 K (room temperature) until the overall Pt composition drops below about 60% (55%) in vacuum and 80% (75%) in oxidizing conditions (Figure 4.9). In oxidizing conditions, I predict that significant Ni content (greater than 0.2%) starts to appear for more Pt-rich particles due to the oxygen-induced segregation of Ni to the particle surface. For best comparison with experimental results, I have chosen to perform more in-depth analysis on nanoparticles with compositions of $Pt_{3398}Ni_{1175}$ and $Pt_{3357}Ni_{1143}Mo_{73}$, closely matching the compositions of the synthesized nanoparticles.[54] For simplicity, I will refer to these compositions as Pt_3Ni and Mo-Pt_3Ni.

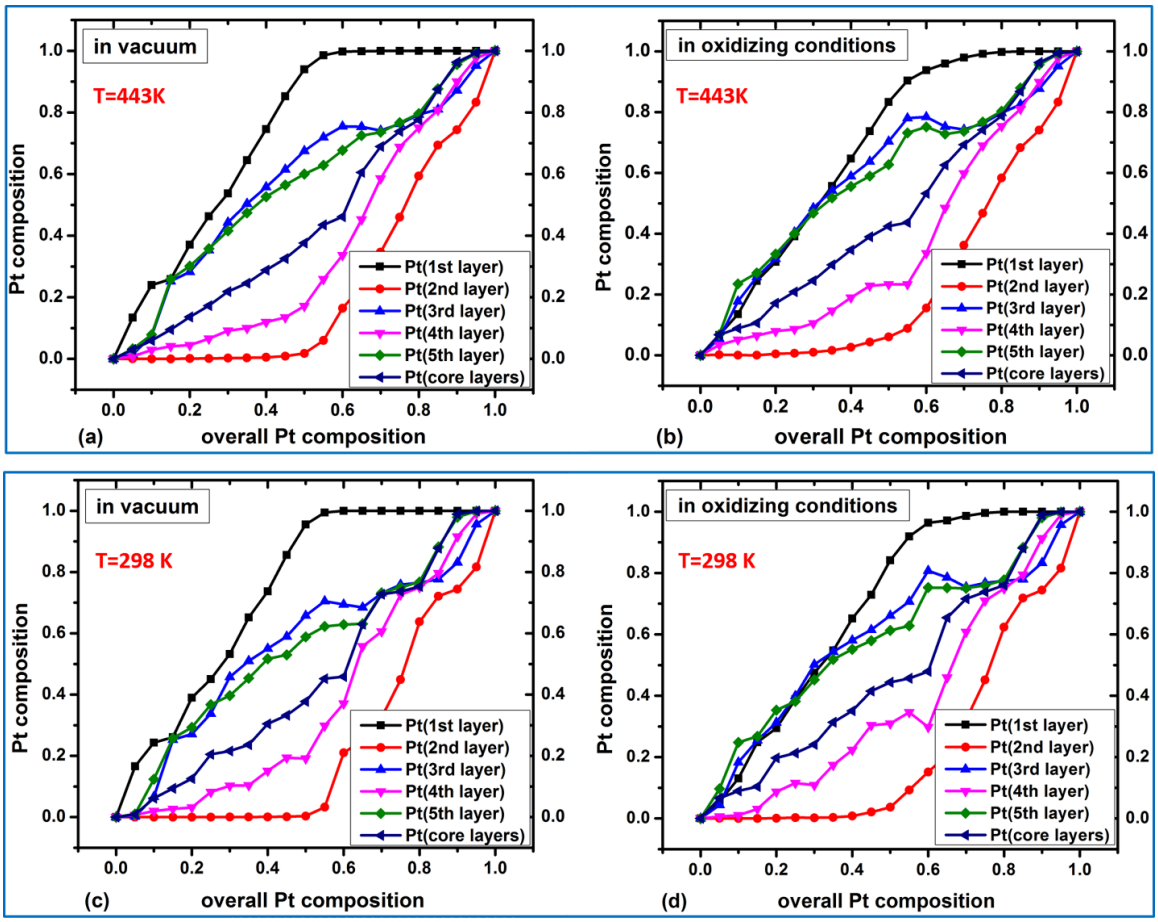

Figure 4.9. Layer-by-layer composition profile for octahedral Pt-Ni nanoparticles with varying Pt content in vacuum at (a) 443 K and (c) 298 K, and in oxidizing conditions at (b) 443 K and (d) 298 K. "Core layers" represent all layers deeper than the fifth layer. The sharp fluctuations around a composition of Pt_3Ni_2 indicate the transition from an $L1_0$-like core to an $L1_2$-like core. Additional evidence for this transition can be seen in Figure 4.8 and Figure 4.10.

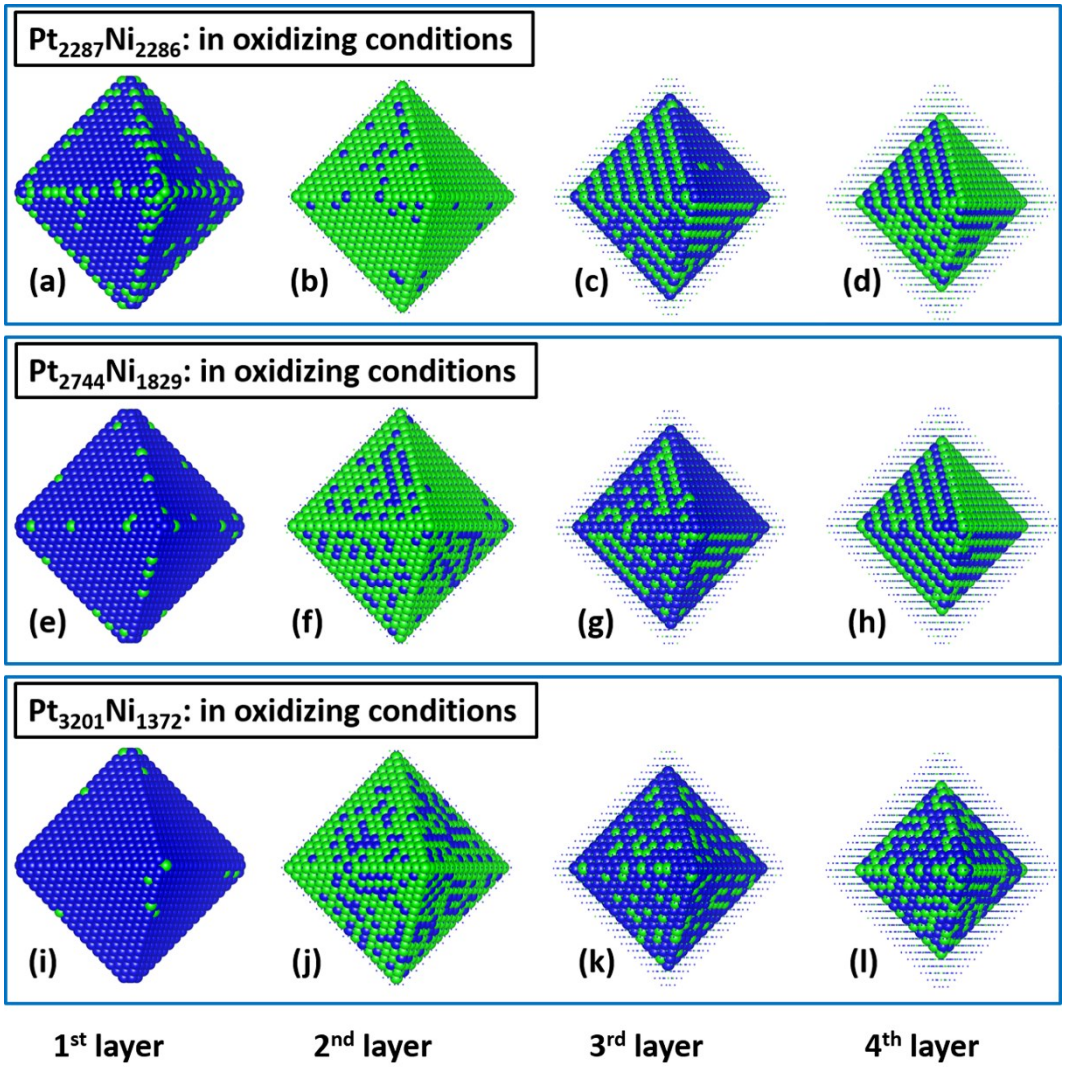

Figure 4.10. At 298 K, taken from a Monte Carlo simulation in oxidizing conditions, the (a) first, (b) second, (c) third, and (d) fourth layers of a representative $Pt_{0.5}Ni_{0.5}$ ($Pt_{2287}Ni_{2286}$) nanoparticle, the (e) first, (f) second, (g) third, and (h) fourth layers of a representative $Pt_{0.6}Ni_{0.4}$ ($Pt_{2744}Ni_{1827}$) nanoparticle, and the (i) first, (j) second, (k) third, and (l) fourth layers of a representative $Pt_{0.7}Ni_{0.3}$ ($Pt_{3201}Ni_{1372}$) nanoparticle. Blue spheres represent Pt and green represent Ni. Small spheres represent the positions of atoms in the outer layers. The transition from an $L1_0$-like core structure to an $L1_2$-like core structure is apparent. Additional evidence of this transition is provided in Figure 4.8.

I have also investigated the effects of temperature on atomic order in Pt-Ni nanoparticles.

For the 4.2 nm Pt_3Ni ($Pt_{3398}Ni_{1175}$) nanoparticles in vacuum, the composition profile for

each layer, calculated by simulated annealing from 1500 K to 0 K, is shown in Figure 4.11(a). The temperature-dependent composition profile has features that are consistent with my results on an extended (111) surface.[92] At low temperatures the nanoparticle has a Pt skin, with increasing Ni concentration on the outermost layer as temperature increases. The Pt concentration reaches a minimum in the second layer and reaches a maximum in the third layer at about 300 K. A similar fluctuation was observed in simulation of extended surfaces. The details of Pt/Ni compositions for each layer at T= 443 K are summarized in Table 4.3 and Table 4.4. Compared with the experimental work of Stamenkovic et al.[53] and my previous computational work[92] on extended Pt_3Ni surfaces, Pt_3Ni nanoparticles have a higher Ni composition in the second, third, and fourth layers. This is partially because the Pt_3Ni surfaces studied in references 53 and 92 were slightly Pt-rich, and the nanoparticles studied here are slightly Pt-poor. However it is also due to the fact that in a nanoparticle there are more sites in the surface layer (the outermost layer) than in any other layers, resulting in a larger percentage of Pt atoms segregating to the Pt-skin surface. The higher Ni compositions in the sub-surface of nanoparticles may partially explain why Pt3Ni nanoparticles have lower ORR activity and stability than the extended surfaces.[53-54, 59, 61, 63, 66, 68]

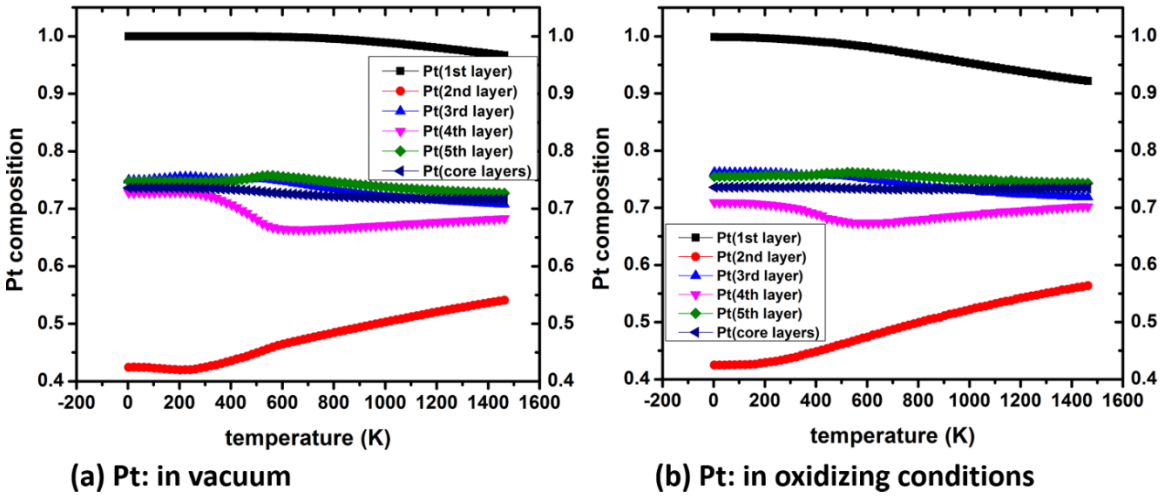

Figure 4.11. The cluster expansion predicted composition profile of Pt_3Ni nanoparticles ($Pt_{3398}Ni_{1175}$) for Pt (a) in vacuum (b) in oxidizing conditions as a function of temperature. "Core layers" represents all layers deeper than the fifth layer.

Table 4.3. Pt composition for each layer of Pt_3Ni ($Pt_{3398}Ni_{1175}$) and Mo-Pt_3Ni ($Pt_{3357}Ni_{1143}Mo_{73}$) nanoparticles at T=443K, both in vacuum and oxidizing conditions.

layers	Pt composition (%)			
	in vacuum		in oxidizing conditions	
	Pt_3Ni nanoparticles ($Pt_{3398}Ni_{1175}$)	Mo-Pt_3Ni nanoparticles ($Pt_{3357}Ni_{1143}Mo_{73}$)	Pt_3Ni nanoparticles ($Pt_{3398}Ni_{1175}$)	Mo-Pt_3Ni nanoparticles ($Pt_{3357}Ni_{1143}Mo_{73}$)
Pt (1^{st} layer)	99.97	99.98	98.9	94.1
Pt (2^{nd} layer)	44.3	45.4	45.4	47.4
Pt (3^{rd} layer)	75.2	73.3	75.7	75.6
Pt (4^{th} layer)	69.4	65.3	68.2	68.5
Pt (5^{th} layer)	75.1	73.5	76.0	76.0
Pt(core layers)	73.8	70.6	73.5	73.7
Pt (all layers)	74.3	73.4	74.3	73.4

Table 4.4. Ni composition for each layer of Pt_3Ni ($Pt_{3398}Ni_{1175}$) and Mo-Pt_3Ni ($Pt_{3357}Ni_{1143}Mo_{73}$) nanoparticles at T=443K, both in vacuum and oxidizing conditions.

layers	Ni composition (%)			
	in vacuum		in oxidizing conditions	
	Pt_3Ni nanoparticles ($Pt_{3398}Ni_{1175}$)	Mo-Pt_3Ni nanoparticles ($Pt_{3357}Ni_{1143}Mo_{73}$)	Pt_3Ni nanoparticles ($Pt_{3398}Ni_{1175}$)	Mo-Pt_3Ni nanoparticles ($Pt_{3357}Ni_{1143}Mo_{73}$)
Ni(1^{st} layer)	0.03	0.02	1.1	0.3
Ni(2^{nd} layer)	55.7	48.8	54.6	52.6
Ni(3^{rd} layer)	24.8	26.0	24.3	24.4
Ni(4^{th} layer)	30.6	34.4	31.8	31.5
Ni(5^{th} layer)	24.9	25.7	24.0	24.0
Ni(core layers)	26.2	28.2	26.5	26.3
Ni(all layers)	25.7	25.0	25.7	25.0

The cluster expansion was used to predict the atomic structures of nanoparticles under cell operating conditions by adding the correction for free energy changes due to the adsorption of oxygen and hydroxyl groups on the surface. At an applied potential of 0.95 V in aqueous solution (which I will refer to as "oxidizing conditions"), the composition profile for Pt_3Ni ($Pt_{3398}Ni_{1175}$) nanoparticles as a function of temperature is shown in Figure 4.11(b). At all temperatures the surface becomes more Ni-rich compared to the particles in vacuum, indicating that the presence of oxidizing species on the surface drives the segregation of Ni to the surface. The additional Ni content of the surface layer results in a more Pt-rich second layer.

To better understand the stability of Pt-Ni nanoparticles, I have calculated nanoparticle surface vacancy formation energies. When an atom dissolves from the nanoparticle surface, a surface vacancy is left behind. The formation energies of these vacancies determine how vulnerable surface atoms are to dissolution and indicate how mobile that atom might be on the particle surface. Here I calculate vacancy formation energies using

bulk crystals as a reference, so that at surface site i on the particle, the vacancy formation energy VFE_i is:

$$VFE_i = E(\text{NP with a vacancy at site i}) + \text{E(bulk)} - E(\text{NP}), \quad (4.8)$$

where $E(\text{NP})$ is the energy of nanoparticle, $E(\text{NP with a vacancy at site i})$ is the energy of nanoparticle with a vacancy at site i, and $E(\text{bulk})$ is the DFT-calculated energy per atom for the bulk fcc phase of the element that occupies site i. Larger values of VFE_i mean that more energy is required to form a surface vacancy. DFT calculations of vacancy formation energies of Pt/Ni ($VFE(Pt/Ni)$) on $Pt_{178}Ni_{47}$ nanoparticles (Figure 4.1) agree with the predictions based on the cluster expansion with a mean absolute error of 126 meV per site (Table 4.5).

Table 4.5. In vacuum, comparison between the DFT-calculated and cluster expansion-predicted vacancy formation energies (VFE) for surface Pt/Ni atoms for $Pt_{178}Ni_{47}$ nanoparticles generated by replacing all Mo atoms in $Pt_{178}Ni_{41}Mo_6$ nanoparticles (Figure 4.1) by Ni. We only calculated one individual site for each type defined in Figure 4.2. The mean absolute error is 126 meV per site.

$Pt_{178}Ni_{47}$ nanoparticles (in vacuum)	VFE(Ni) / eV		VFE(Pt) / eV	
	DFT	cluster expansion	DFT	cluster expansion
vertex	0.088	-0.001	0.033	0.0
edge-1	0.691	0.561	0.809	0.587
edge-2	0.576	0.418	0.650	0.449
face-1	1.106	0.951	1.316	1.193
face-2	0.903	0.732	1.049	0.889
face-3	0.542	0.498	0.481	0.510

Table 4.6. In vacuum, comparison between the DFT-calculated and cluster expansion-predicted vacancy formation energies (VFE) of surface Pt/Ni atoms for $Pt_{178}Ni_{41}Mo_6$ nanoparticles (Figure 4.1). I only calculated one individual site for each type defined in Figure 4.2. The mean absolute error is 143 meV per site.

$Pt_{178}Ni_{41}Mo_6$ nanoparticles (in vacuum)	VFE(Ni) / eV		VFE(Pt) / eV	
	DFT	cluster expansion	DFT	cluster expansion
vertex	0.162	0.162	0.080	0.292
edge-1	0.702	0.539	0.837	0.611
edge-2	0.515	0.384	0.608	0.482
face-1	1.046	0.943	1.239	1.195
face-2	0.884	0.680	1.035	0.848
face-3	0.522	0.631	0.536	0.746

I have used Monte Carlo simulations to calculate the average vacancy formation energy for each element at each surface site at a temperature of 443 K for Pt_3Ni ($Pt_{3398}Ni_{1175}$) nanoparticles. For all Pt/Ni surface sites, the predicted vacancy formation energy is positive, indicating that it is not thermodynamically favorable for Pt and Ni atoms in the nanoparticle to dissolve into a solution that is in equilibrium with elemental fcc Pt or Ni crystals (as shown in Figure 4.12(a) and (b)). However it still might be favorable for Pt and/or Ni atoms to dissolve to form other compounds such as Pt-Ni alloys or Ni-oxides. In vacuum, both Pt and Ni atoms dissolve most readily from vertex sites followed by edge sites, and it is least favorable for them to dissolve from sites on the (111) facet. In addition, my calculations indicate that the surface concentration of Ni is higher on edge and vertex

sites than on facet sites (Figure 4.13(a)). This would indicate that the leaching of Ni from the surface likely starts from vertex/edge sites (or similarly low-coordinated sites), leading to more spherical-shaped nanoparticles.

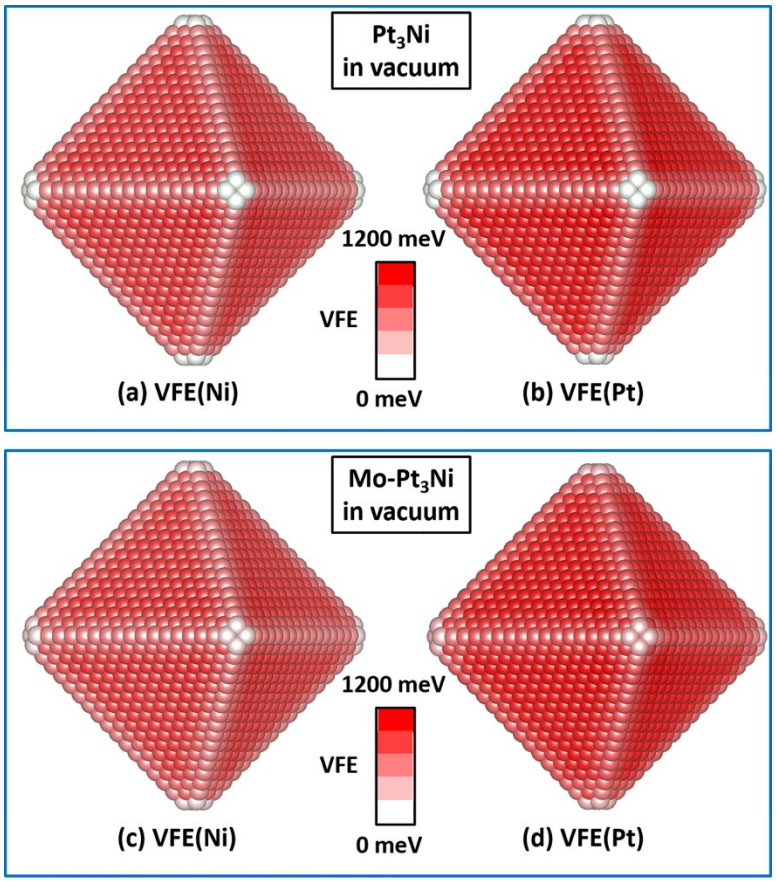

Figure 4.12. In vacuum at 443K, the average surface vacancy formation energies for (a) Ni and (b) Pt for Pt_3Ni ($Pt_{3398}Ni_{1175}$) nanoparticles, and (c) Ni and (d) Pt for Mo-Pt_3Ni ($Pt_{3357}Ni_{1143}Mo_{73}$) nanoparticles. The redder the sphere, the larger the VFE (indicating a lower tendency to dissolve). Red spheres represent *VEE*=1.2 eV, and white spheres represent *VFE*=0 eV.

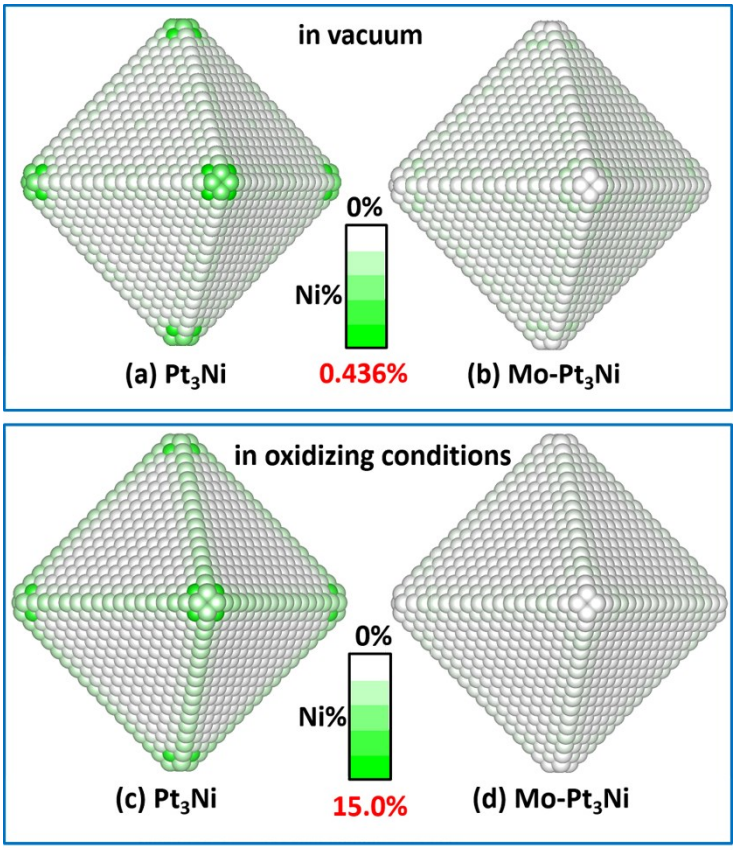

Figure 4.13. At 443K, the average Ni site occupancies in the surface layer of (a) Pt_3Ni ($Pt_{3398}Ni_{1175}$) and (b) Mo-Pt_3Ni ($Pt_{3357}Ni_{1143}Mo_{73}$) nanoparticles in vacuum; and those of (c) Pt_3Ni ($Pt_{3398}Ni_{1175}$) and (d) Mo-Pt_3Ni ($Pt_{3357}Ni_{1143}Mo_{73}$) nanoparticles in oxidizing conditions. Darker green spheres indicate higher Ni content, and white spheres represent zero Ni content. Different color scales are used for vacuum and oxidizing conditions. The minimum, maximum, and average values on each surface are provided in Table 4.7 below.

Table 4.7. The minimum, maximum, and average values of the average Ni site occupancies on each surface site of Pt_3Ni ($Pt_{3398}Ni_{1175}$) and Mo-Pt_3Ni ($Pt_{3357}Ni_{1143}Mo_{73}$) nanoparticles at T=443K, both in vacuum and oxidizing conditions.

values	Ni site occupancy (%)			
	in vacuum		in oxidizing conditions	
	Pt_3Ni nanoparticles ($Pt_{3398}Ni_{1175}$)	Mo-Pt_3Ni nanoparticles ($Pt_{3357}Ni_{1143}Mo_{73}$)	Pt_3Ni nanoparticles ($Pt_{3398}Ni_{1175}$)	Mo-Pt_3Ni nanoparticles ($Pt_{3357}Ni_{1143}Mo_{73}$)
minimum	2.05E-04	1.53E-03	0.02	0.04
maximum	0.436	7.78E-02	13.04	1.11
average	0.0324	0.0185	1.06	0.27

In oxidizing conditions, I estimate the vacancy formation energy by applying an energetic correction that accounts for adsorbed OH on surface Pt/Ni atoms. The correction, $\Delta G(*\mathrm{OH})$, is calculated as described in the Section 4.2. I apply this correction only to the particle that contains no vacancies, under the assumption that adsorbed OH does not stabilize the sub-surface atoms once a vacancy is formed. Thus

$$VFE_i(\text{oxidizing}) = VFE_i(\text{vacuum}) - \Delta G(*\mathrm{OH}), \tag{4.9}$$

where $VFE_i(\text{vacuum})$ is VFE_i defined in Eq. (4.8).

In oxidizing conditions, I calculate a remarkable reversal (Figure 4.14): Vacancy formation energies on edge sites are larger than those on facet sites by an amount of ~400 meV for Ni (Figure 4.14 (a)), and ~200 meV for Pt (Figure 4.14 (b)). These results are supported by DFT calculations on the prototypical 225-atom ($Pt_{178}Ni_{47}$) nanoparticle (Table 4.8). This indicates that edge sites of Pt3Ni octahedral nanoparticles can be more resistant to dissolution than facet sites because they are protected by an oxidized surface. This is consistent with my previous computational results[54], which indicated that it is much more energetically favorable for oxygen to adsorb near edge sites than in the center of a facet, and with the experimental observation of a small signal for oxidized Pt in Ni-Pt and Mo-Ni-Pt nanoparticles.[54, 148] My calculations indicate that the relative gain in edge site stability upon oxidation is more than enough to compensate for relative instability of edge sites due to their low coordination number (Figure 4.15). This suggests another possible explanation for the concave octahedra observed by Cui et al.[59] The formation of a protective oxide layer near the edge sites may lead to more rapid dissolution from the sites

near the center of the particle facets than edge sites. However, I note that even in oxidizing conditions the vacancy formation energies on vertex sites are smaller than those on facet sites by an amount of ~90 meV for Ni and ~ 300 meV for Pt, indicating that Pt/Ni atoms on vertex sites are the most vulnerable to dissolution (Figure 4.14). These results suggest that there is a competition between dissolution from facet sites and dissolution from vertex sites that affects the shape evolution of Pt-Ni nanoparticles in oxidizing conditions.

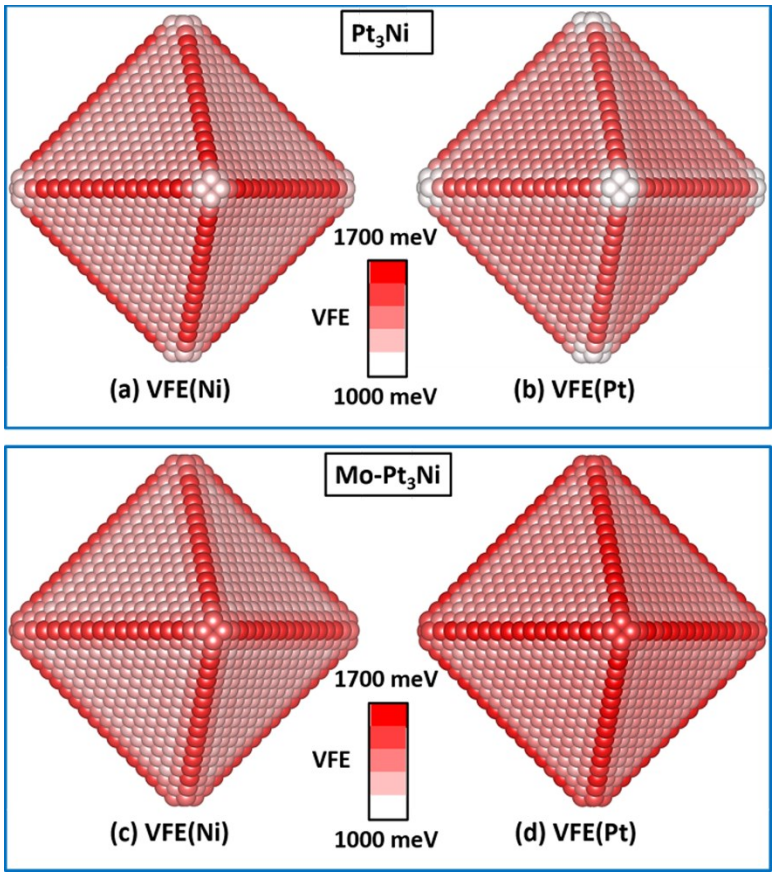

Figure 4.14. In oxidizing conditions at 443K, the average surface vacancy formation energies for (a) Ni and (b) Pt for Pt_3Ni ($Pt_{3398}Ni_{1175}$) nanoparticles, and (c) Ni and (d) Pt for Mo-Pt_3Ni ($Pt_{3357}Ni_{1143}Mo_{73}$) nanoparticles. The redder the sphere, the larger the vacancy formation energy (lower tendency to dissolve). Red spheres represent VFE=1.7 eV, and white spheres represent VFE=1.0 eV.

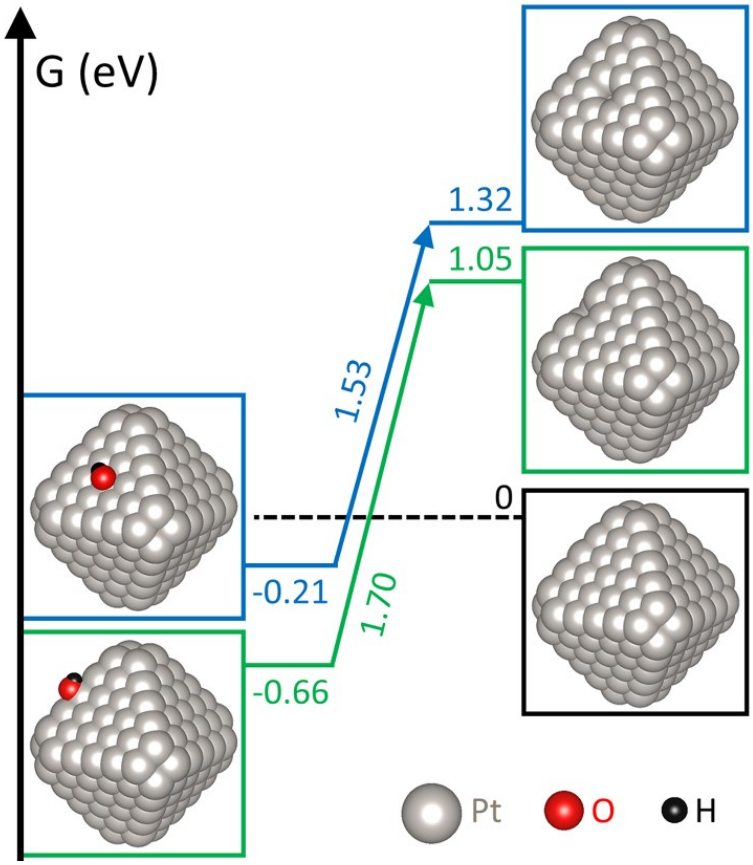

Figure 4.15. The DFT-calculated vacancy formation energies for Pt-OH on an edge-1 (green) site and a face-1 (blue) site of the prototypical 225-atom nanoparticle, where the site types are as defined in Figure 4.2. Average values over multiple sites of the same type are given in Table S6. On the left are the free energies of particles with adsorbed OH, and on the right are the free energies of particles with vacancies (blue and green) and a clean $Pt_{178}Ni_{47}$ nanoparticle (black). The values on the diagonal lines are the vacancy formation energies. All values are with respect to clean $Pt_{178}Ni_{47}$, bulk Pt, and OH at 0.95V vs the RHE in aqueous solution. The calculated free energies depend on this choice of reference states, but the difference between free energies for the different sites does not.

Table 4.8. In oxidizing conditions, comparison between the DFT-calculated and cluster expansion-predicted vacancy formation energies (VFE) for surface Pt/Ni atoms for $Pt_{178}Ni_{47}$ nanoparticles (Figure 4.1). For each type defined in Figure 4.2, I calculated one individual atomic configuration for Ni, and three different atomic configurations for Pt (average values are listed). The mean absolute error is 114 meV / site.

$Pt_{178}Ni_{47}$ nanoparticles (in oxidizing conditions)	VFE(Ni) / eV		VFE(Pt) / eV	
	DFT	cluster expansion	DFT	cluster expansion
vertex	1.250	1.179	1.019	1.040
edge-1	1.698	1.621	1.702	1.489
edge-2	1.550	1.367	1.399	1.330
face-1	1.430	1.306	1.517	1.449
face-2	1.367	1.252	1.327	1.210
face-3	1.135	1.096	0.913	1.004

Table 4.9. In oxidizing conditions, comparison between the DFT-calculated and cluster expansion-predicted VFE of surface Pt/Ni atoms for $Pt_{178}Ni_{41}Mo_6$ nanoparticles (Figure 4.1). I calculated one individual site for each type (Figure 4.2). The mean absolute error is 146 meV / site.

$Pt_{178}Ni_{41}Mo_6$ nanoparticles (in oxidizing conditions)	VFE(Ni) / eV		VFE(Pt) / eV	
	DFT	cluster expansion	DFT	cluster expansion
vertex	1.342	1.343	1.187	1.326
edge-1	1.749	1.599	1.710	1.445
edge-2	1.545	1.333	1.417	1.242
face-1	1.445	1.297	1.513	1.450
face-2	1.418	1.200	1.344	1.215
face-3	1.149	1.229	1.026	1.197

The oxidation of the edges of the nanoparticle could explain another apparent discrepancy between my calculated results and experiments: the experimental observation of Pt-rich edges in Pt-Ni nanoparticles. I have used the cluster expansion to calculate the average occupancy of individual sites at 443 K (Figure 4.16 and Figure 4.17). As with the extended surface[92], for Pt_3Ni ($Pt_{3398}Ni_{1175}$) nanoparticles (Figure 4.16), the outermost layer is predominantly Pt skin, with a disordered Ni-rich second layer and increasing order in subsequent layers. In both vacuum and oxidizing conditions at 443 K, the vertex and edge sites in the second layer are much more likely to contain Ni than Pt atoms. To better compare with the results of Cui. et al.[59], I have generated similar composition maps for $PtNi_{1.5}$ ($Pt_{1829}Ni_{2744}$) nanoparticles (Figure 4.17). The calculated composition maps (Figure 4.16 and Figure 4.17) do not indicate that in thermodynamic equilibrium the edges of particles should become Pt-rich, with relatively Ni-rich facets, in contrast with experimental results.[59-60]

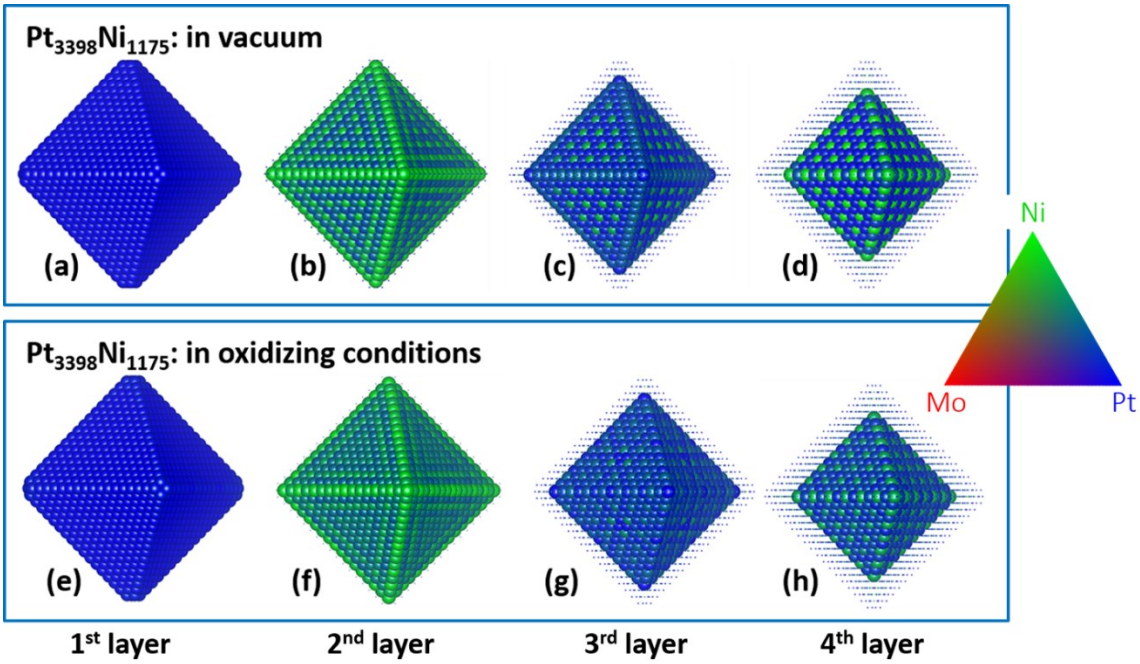

Figure 4.16. For the Pt_3Ni ($Pt_{3398}Ni_{1175}$) nanoparticles, the predicted Pt/Ni average site occupancies of the (a) first, (b) second, (c) third, and (d) fourth layers in vacuum, and the (e) first, (f) second, (g) third, and (h) fourth layers in oxidizing conditions at 443 K as determined by Monte Carlo simulations. Blue spheres represent pure Pt, green represent pure Ni, and red represent pure Mo. Other colors represent fractional occupancies, as indicated by the color triangle on the right. Small spheres represent the positions of atoms in the outer layers.

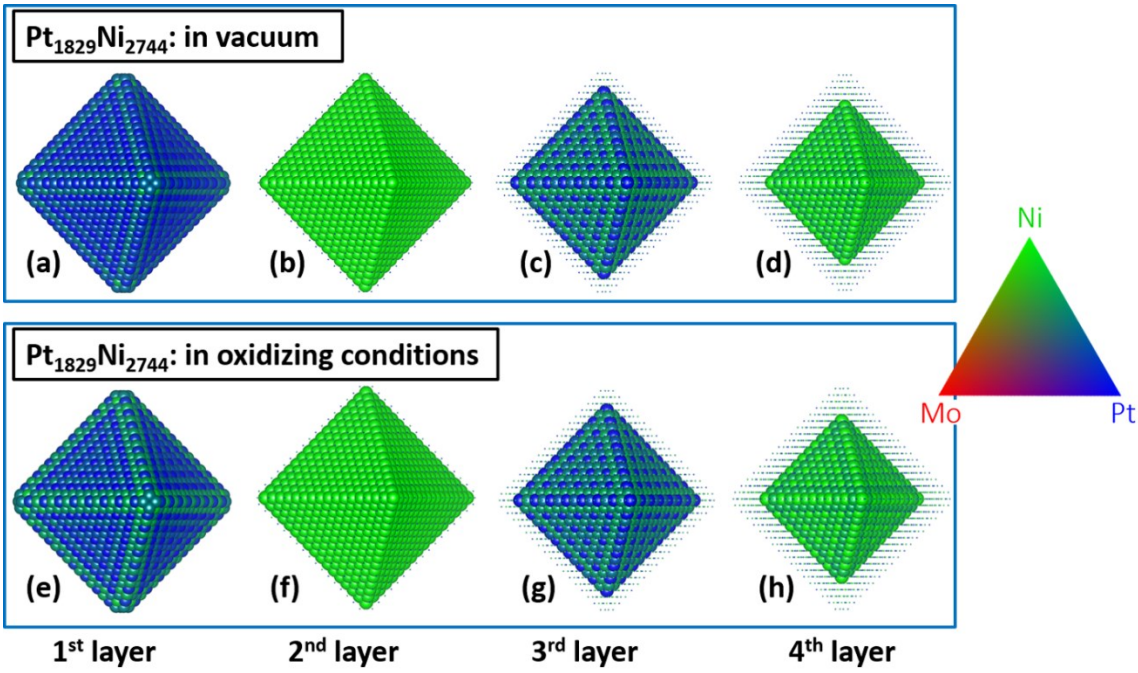

Figure 4.17. For the $PtNi_{1.5}$ ($Pt_{1829}Ni_{2744}$) nanoparticles, the predicted Pt/Ni average site occupancies of the (a) first, (b) second, (c) third, and (d) fourth layers in vacuum, and the (e) first, (f) second, (g) third, and (h) fourth layers in oxidizing conditions at 443 K as determined by Monte Carlo simulations. Blue spheres represent pure Pt, green represent pure Ni, and red represent pure Mo. Other colors represent fractional occupancies, as indicated by the color triangle on the right. Small spheres represent the positions of atoms in the outer layers.

This apparent discrepancy may be explained by considering that the model (in oxidizing conditions) used in this chapter captures the effects of an oxidizing environment on sub-surface sites only indirectly, through the interaction of sub-surface sites with surface sites. However it is possible that a monolayer of oxygen (or a related species) on the surface directly drives the sub-surface segregation of Pt atoms towards the oxidized region of the surface. To examine this hypothesis, I have run Monte Carlo simulations on an extended (111) surface using the cluster expansion constructed in Chapter 3 (Figure 3.14). For these calculations, I constrained the outermost layer to have a pure Pt skin. In the grand canonical ensemble, I found that as the oxygen coverage increases, the percent of Pt in the

second layer (and in the slab overall) also increases (Figure 3.14(a)). A similar result holds in the mix ensemble (Figure 3.14(b)), where Pt/Ni group is canonical ensemble under fixed Pt composition with 75% Pt, and Vacancy/O group is grand canonical ensemble. This suggests that Pt atoms will likely segregate to the sub-surface sites beneath oxidized surface sites. In Pt-Ni nanoparticles, oxidized edges could attract Pt atoms to sub-surface edge sites, accounting for the observation of Pt-rich edges in the particles.[59-60] The combination of Pt-rich edges and a protective oxide layer on the edges could result in the more rapid dissolution of Ni from facet sites. A more advanced model, which explicitly include the structures with adsorption oxygen atoms into the training set, needs to be constructed to investigate this possibility in more depth.

4.4 Effects of Mo doping

4.4.1 DFT predicted surface segregation of Mo/Ni atoms

As shown in Figure 3.14, by fixing the outermost layer as Pt-skin, the adsorption of surface oxygen atoms will drive the inner-layer Pt atoms to the second layer, when I assume that the surface structure of Pt-Ni catalysts is thermodynamically trapped in the state of Pt-skin. However, thermodynamically, the strong drive force of oxidizing adsorbates (e.g. *OH and *O) will drive Mo and Ni atoms to the surface, leading to surface segregation of Mo/Ni atoms.

To assess the energetics of surface segregation, DFT calculations were performed on both the ground-state 9-layer extended (111) slab with composition $Pt_{27}Ni_7Mo_2$ (Figure 4.18) and the ground-state $Pt_{178}Ni_{41}Mo_6$ nanoparticle (Figure 4.1). The $Pt_{27}Ni_7Mo_2$ slab (Figure 4.18) was identified by the cluster expansion built on the extended (111) surfaces in Chapter 3 as the ground-state structure at this composition, replacing two Ni atoms in the second layer with two Mo atoms. To prevent interaction between neighboring surfaces (and adsorbed molecules) in the periodic unit cell, a distance of 2.25 nm was provided between opposing surfaces. All calculations on slabs were done in a way to preserve the symmetry between the two slab surfaces. Although this $Pt_{178}Ni_{41}Mo_6$ nanoparticle (Figure 4.1) is smaller than the experimentally-observed nanoparticles (4 – 20 nm), it retains key structural features and is small enough to be modeled using density functional theory. To evaluate the chemical effects of Mo doping independent of shape/size effects, the particle

was compared with an undoped particle with composition $Pt_{178}Ni_{47}$ generated by replacing the Mo atoms on sub-surface vertex sites with Ni atoms (Figure 4.1).

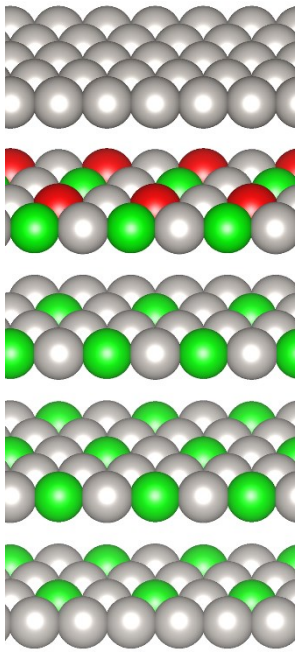

Figure 4.18. The top five layers of the nine-layer $Pt_{27}Ni_7Mo_2$ slab. Gray spheres represent Pt, blue represent Ni, and red represent Mo. The third and fourth layers are aligned so that the Ni atom is in the hollow site formed by three Pt atoms in the layer below it. The second layer is aligned so that the Mo atom falls in the hollow site formed by three Pt atoms in the third layer. The four bottom layers (not shown) are symmetrically equivalent to the four top layers.

For the clean slab in vacuum, Mo is more stable at a subsurface site than the lowest-energy surface site by 0.881 eV per Mo atom. For the nanoparticle in vacuum, the subsurface site is favored over the lowest-energy neighboring surface site by 1.110 eV. The situation reverses in the presence of oxygen. In the presence of adsorbed oxygen on the (111) surface (with ¼ monolayer coverage), there is a driving force of 1.559 eV per Mo atom for Mo to segregate to the surface, and the oxygen preferentially adsorbs atop the surface Mo atom.

For the $Pt_{178}Ni_{41}Mo_6$ nanoparticle, similar results were found: the most favorable site for Mo surface segregation in the presence of one single adsorbed oxygen atom for the $Pt_{178}Ni_{41}Mo_6$ nanoparticle was determined by evaluating Mo segregation to each of the nearest face, vertex, and edge sites for each of the symmetrically distinct Mo atoms. In each case, the adsorbed oxygen atom was placed atop the surface Mo atom (Figure 4.19(a)), as my calculations indicate that this is the most favorable site for single oxygen adsorption. Among a single adsorbed oxygen placed atop the surface face, edge, and vertex sites (Figure 4.2), Mo preferentially segregates to a vertex site, and the driving force for this segregation is 1.533 eV.

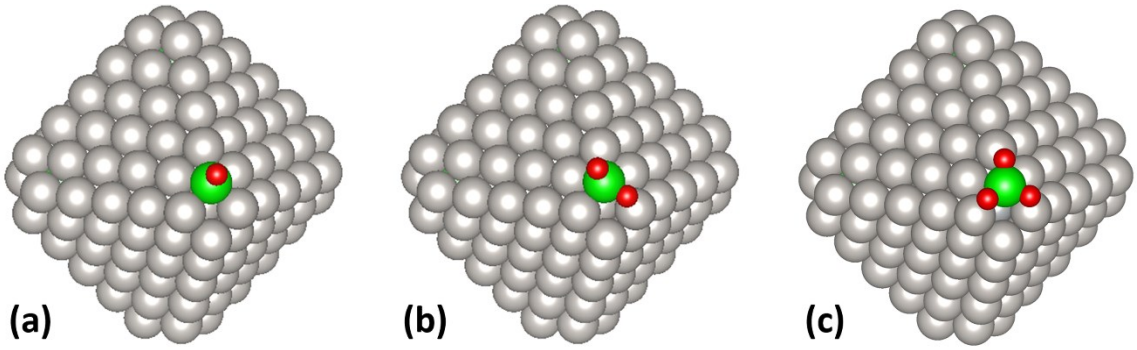

Figure 4.19. The relaxed structures used to calculate the stability of (a) one, (b) two, (c) and three oxygen atoms adsorbed on a Mo atom on the vertex of $Pt_{178}Ni_{41}Mo_6$. Grey spheres represent Pt, green represent Mo, and red represent oxygen.

Furthermore, the $Pt_{178}Ni_{41}Mo_6$ nanoparticle with a single Mo atom segregated to the energetically-preferred vertex site (Figure 4.19) was used to assess the stability of surface Mo-oxide species against reduction to H_2O. The structures used in these calculations, consisting of one (Figure 4.19(a)), two (Figure 4.19(b)), and three oxygen atoms (Figure 4.19(c)) adsorbed on the vertex Mo atom, are shown in Figure 4.19. The CHE model[55] was

used to calculate stability, where the energies of H_2O, H_2, and the nanoparticle were calculated using DFT. Zero-point energies were calculated in the harmonic approximation using DFT and the finite differences method. The slab with Mo segregated to the surface was used to estimate the zero point energy for O adsorbed atop a Mo atom, where the positions of the atoms in the slab were held fixed. Gas-phase free energies for H_2 and H_2O were taken from reference 150. Starting from 3*O, the adsorbed O was calculated to be stable against reduction to H_2O down to potentials of 0.2 V (for the first atom removed; from 3*O to 2*O), 0.3 (for the second atom removed; from 2*O to *O), and -1.0 V (for the third atom removed; from *O to clean particle) versus the RHE.

Due to the relatively strong Mo-Pt and Ni-Pt nearest-neighbor bonds, both Mo and Ni prefer to occupy similar sites with many Pt nearest neighbors. However in oxidizing conditions the energetic driving force for Mo segregation to the surface is much stronger than the driving force for Ni segregation. For the $Pt_{27}Ni_7Mo_2$ slab with ¼ monolayer oxygen coverage, the calculated driving force for second-layer Mo to migrate to the surface is 1.559 eV per atom, as opposed to 0.284 eV per atom for Ni. This suggests that in oxidizing conditions Mo atoms may "crowd out" Ni atoms on the particle surface, reducing the number of surface Ni atoms available for dissolution. All discussions in this subsection are based on DFT calculations on 9-layer slabs and 225-atom nanoparticle (with size of ~1 nm), which is much smaller than the experimentally synthesized Pt-Ni octahedral nanoparticles (with size of about 4 – 20 nm[54, 59-60, 63, 67-68]). I will explicitly demonstrate the Mo doping effects on the structure and stability of Pt-Ni octahedral nanoparticles with a size of ~4 nm in next subsection.

4.4.2 Stability enhancement due to Mo doping

To better understand the effects of Mo-doping on the highly improved durability and stability of Mo-doped Pt_3Ni nanoparticles[54] (with size of ~4 nm) at the atomic scale, I have used a quaternary Mo-Ni-Pt-Vacancy cluster expansion to calculate the equilibrium atomic structures and stability against dissolution (in terms of surface vacancy formation energy) for Mo-Pt_3Ni nanoparticles.

The composition profiles for the Mo-Pt_3Ni ($Pt_{3357}Ni_{1143}Mo_{73}$) nanoparticles as a function of temperature in both vacuum and oxidizing conditions are shown in Figure 4.20(a) and (b) for Pt and Figure 4.20(c) and (d) for Mo. In vacuum, as shown in Figure 4.20(c). Mo prefers the second layer and all Mo atoms segregate to the second layer as the temperature approaches zero. Upon doping with Mo at 443 K, Ni shifts from the second layer to inner layers and Pt shifts from inner layers to the second layer, with the Ni composition in the second layer reduced from 55.7% to 48.8%, and Pt composition in the second layer enhanced from 44.3% to 45.4% (Table 4.3 and Table 4.4). Accordingly, the Pt composition is reduced in all layers deeper than the second layer.

In oxidizing conditions, the structure is similar to the structure in vacuum. The main difference is that all Mo atoms are pulled from inner layers to the surface (Figure 4.20(d)) to form a Mo-oxide on the surface, consistent with the experimental observation of oxidized Mo atoms in Mo-Pt and Mo-Ni-Pt particles.[54, 148] Compared to the undoped particle, the Pt composition in the second layer is enhanced from 45.4% to 47.4% (Table 4.3). This may partially explain the enhanced ORR activity in Mo-Pt_3Ni nanoparticles, as

my results on extended surfaces indicate that a higher Pt composition in the second layer will likely lead to higher catalytic activity.[92]

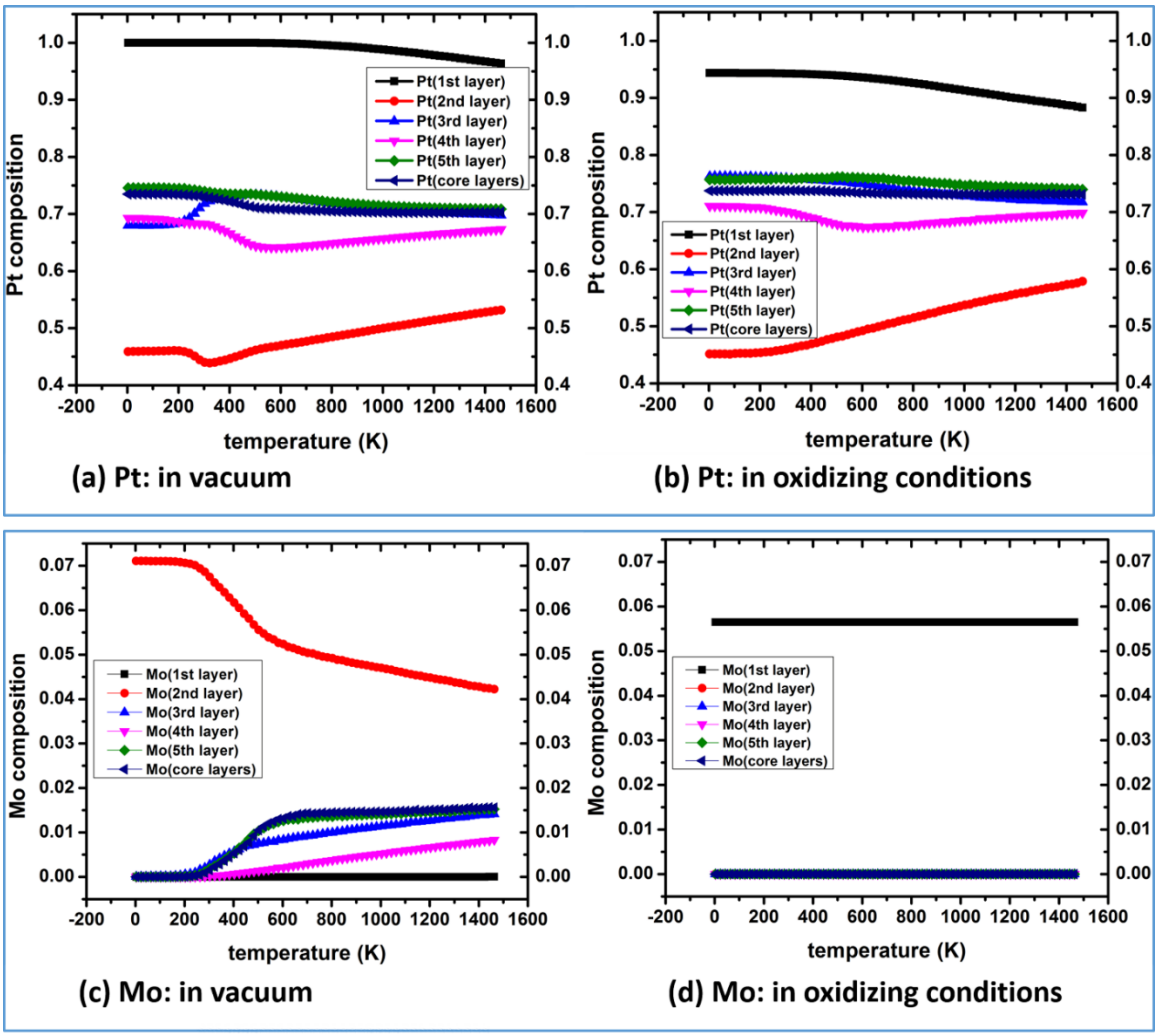

Figure 4.20. The cluster expansion predicted composition profile of Mo-Pt_3Ni ($Pt_{3357}Ni_{1143}Mo_{73}$) nanoparticles for (a) Pt and (c) Mo in vacuum, and (b) Pt and (d) Mo in oxidizing conditions. "Core layers" represent all layers deeper than the fifth layer.

For Mo-Pt_3Ni nanoparticles, at 443 K, the average occupancies of individual sites in thermodynamic equilibrium predicted by cluster expansion in both vacuum and oxidizing

conditions are shown in Figure 4.21. In vacuum Mo prefers the second-layer vertex sites (with 100% Mo) and edge sites (with 1.2 % – 51.0 % Mo). In oxidizing conditions, Mo prefers vertex sites and edge sites in the outermost layer (Figure 4.21(e)), with 25% Mo on vertex sites, and 13.3 % – 48.8 % Mo on edge sites, which agrees with experimental observation of the existence of oxidized Mo.[54, 148]

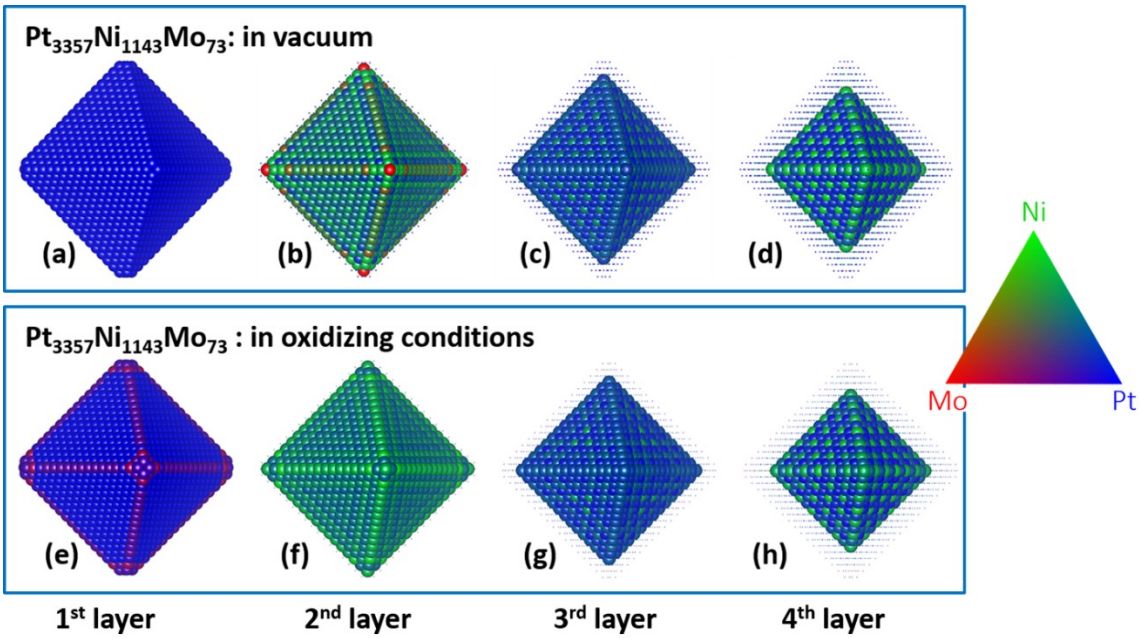

Figure 4.21. For the Mo-Pt_3Ni ($Pt_{3357}Ni1_{143}Mo_{73}$) nanoparticles, the predicted Pt/Ni/Mo average site occupancies of the (a) first, (b) second, (c) third, and (d) fourth layers in vacuum, and the (e) first, (f) second, (g) third, and (h) fourth layers in oxidizing conditions at 443K as determined by Monte Carlo simulations. Blue spheres represent pure Pt, green represent pure Ni, and red represent pure Mo. Other colors represent fractional occupancies, as indicated by the color triangle on the right. Small spheres represent the positions of atoms in the outer layers.

In oxidizing conditions at 443 K, my Monte Carlo simulations predict that the existence of Mo-oxide in the outermost layer lowers the average Ni composition in the surface layer from 1.06% to 0.27% (a factor of ~4) (Figure 4.13(c) and (d)). This effect is particularly

apparent on vertex, nearest-vertex facet, and edge sites. Ni average site occupancies are reduced from 4.412% to 0.118% (a factor of ~37) on vertex sites, reduced from 13.040% to 0.471% (a factor of ~28) on nearest-vertex facet sites, and reduced from 3.235% to 0.529% (by a factor of ~6) on edge sites. These results suggest that Mo atoms stabilize Pt_3Ni nanoparticles in part by greatly reducing the amount of surface Ni atoms exposed to aqueous solution, especially on low-coordinated edge and vertex sites that may be particularly vulnerable to dissolution. A similar result holds in vacuum. The existence of Mo in the second layer lowers the average composition of Ni in the surface layer for Pt_3Ni nanoparticles from 0.0324% to 0.0185% (a factor of ~2) (Figure 4.13(a) and (b)). The effect is more pronounced on vertex sites, where the Ni composition is reduced from 0.24% to 1.53E-3% (a factor of ~157).

For Pt_3Ni nanoparticles without Mo doping in oxidizing conditions, my calculations indicate that both Pt and Ni atoms at vertex sites are most vulnerable to dissolution (Figure 4.14(a) and (b)), which can lead to the loss of the octahedral shape. On the other hand, for Mo-Pt_3Ni nanoparticles, Pt and Ni atoms on facet sites become most vulnerable to dissolution from the surface (Figure 4.14(c) and (d)) because the formation of surface Mo oxide on vertex/edge sites (Figure 4.21(e)) provides additional stabilization to surface Pt/Ni atoms on vertex sites. Thus, the edges (including both vertex and edge sites) of Pt_3Ni octahedral nanoparticles are further stabilized due to Mo doping, which agrees with the experimental observation of the highly retained octahedral shape.[54]

By directly subtracting vacancy formation energies (VFEs) of Pt_3Ni nanoparticles (Figure 4.14(a) and (b)) from those of Mo-Pt_3Ni nanoparticles (Figure 4.14(c) and (d)), I have calculated the average surface vacancy formation energy change (ΔVFE) due to Mo doping

(Figure 4.22). For both Ni and Pt, the largest increase in vacancy formation energies are on vertex sites: 255 meV for Ni, and 484 meV for Pt respectively. On edge sites, the enhancement of the vacancy formation energy for Pt is 108 meV to 304 meV (Figure 4.22(b)). On the other hand, the vacancy formation energies for Ni on edge sites are reduced by 12 meV – 57 meV due to Mo doping (Figure 4.22(a)), but they are still higher than those on facet sites (Figure 4.14(c)) so that surface Ni atoms are still more energetically favorable to dissolve from facet sites than edges sites.

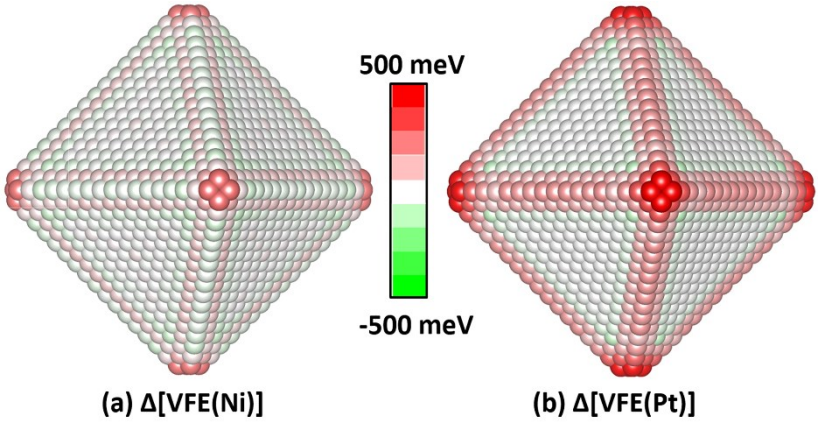

Figure 4.22. In oxidizing conditions at 443 K, the average vacancy formation energy (VFE) change for Pt/Ni atoms (ΔVFE) due to doping Mo: (a) The change in vacancy formation energies for Ni (b) The change in vacancy formation energies for Pt. Here, red spheres represent $\Delta VFE > 0$, which means that it becomes harder for Pt/Ni atoms to dissolve due to Mo doping; green spheres mean $\Delta VFE < 0$, meaning that it becomes easier for the atoms to dissolve.

Thus, my simulation results provide evidence to quantitatively explain the highly improved stability of Pt3Ni nanoparticles due to Mo doping. There are two mechanisms that are thought to lead to the loss of stability of Pt-Ni nanoparticles. One is the dissolution of surface Ni atoms,[58-59] and the other one is the migration of Pt in the surface layer.[60] For

the first mechanism, Mo doping protects against Ni dissolution by significantly reducing the Ni composition in the surface layer of Pt3Ni nanoparticles in oxidizing conditions (especially on vertex and edge sites). Thus fewer Ni atoms will be exposed to aqueous solution, making the particles more resistant to Ni dissolution (Figure 4.13(c) and (d)). In addition, vulnerable Ni atoms on vertex sites are protected against dissolution by the formation of a surface Mo-oxide. For the second mechanism, recently Beermann et al. argued that the migration of Pt on the particle surface is mainly responsible for the octahedral shape loss for Pt/Ni nanoparticles.[60] The cluster expansion predicts that Mo doping increases the vacancy formation energies for Pt and Ni on vertex sites of Pt3Ni nanoparticles by 250 ~ 500 meV in oxidizing conditions (Figure 4.14), due to the proximity of nearby oxidized Mo atoms. I expect a similar result to hold for other sites with similarly low coordination, suggesting that Mo stabilizes the surface atoms that are most likely to be mobile. The combination of the reduction of surface Ni composition and the stabilization of sites with low coordination provides an explanation for why doping a small amounts of Mo atoms (1.6% molar) can greatly stabilize the shape and composition of octahedral Pt_3Ni nanoparticles.[54]

4.4.3 ORR activity enhancement due to Mo doping

As shown in section 4.4.2, doping a small amount of Mo (1.6 % molar) stabilizes the shape of octahedral nanoparticles and reduces the Ni composition in the surface layer, so as to prevent the degradation of Pt-Ni nanoparticles under cell operating conditions. Also, at 443K in oxidizing conditions I predict that in the second layer, Pt composition is enhanced from 45.4 % to 47.4 %, and Ni composition is reduced from 54.6 % to 52.6 %, which partially explains the highly improved ORR activity of Mo-Pt_3Ni nanoparticles[54] according to the results on extended surfaces from both the experimental work[53] and computational work[92] (demonstrated in Chapter 3 of this thesis).

Given the relationship between ORR activity and oxygen binding energy (ΔE_O) shown in the volcano plot (Figure 1.1), it may be more straightforward to investigate Mo doping effects on ORR activity in terms of predicting the change of oxygen binding energies on the surface of nanoparticles. Thus, I calculated the oxygen binding energies on all fcc and hcp hollow sites on the (111) facet of the 225-atom $Pt_{178}Ni_{41}Mo_6$ and $Pt_{178}Ni_{47}$ nanoparticles (Figure 4.1), as shown in Figure 4.23. In Figure 4.23(a), the oxygen binding energy on the $Pt_3Ni(111)$ surface was calculated at ¼ coverage using the ground-state 9-layer $Pt_{27}Ni_9$ slab predicted by the cluster expansion in Chapter 3 (Figure 3.7(b)). Binding energies were evaluated on all symmetrically distinct fcc and hcp sites at ¼ monolayer coverage, and the lowest binding energy (strongest binding), which was found on an fcc site, was used in Figure 4.23. For the Pt(111) surface, the oxygen binding energy was

calculated on the fcc site of a 9-layer slab at ¼ monolayer coverage.

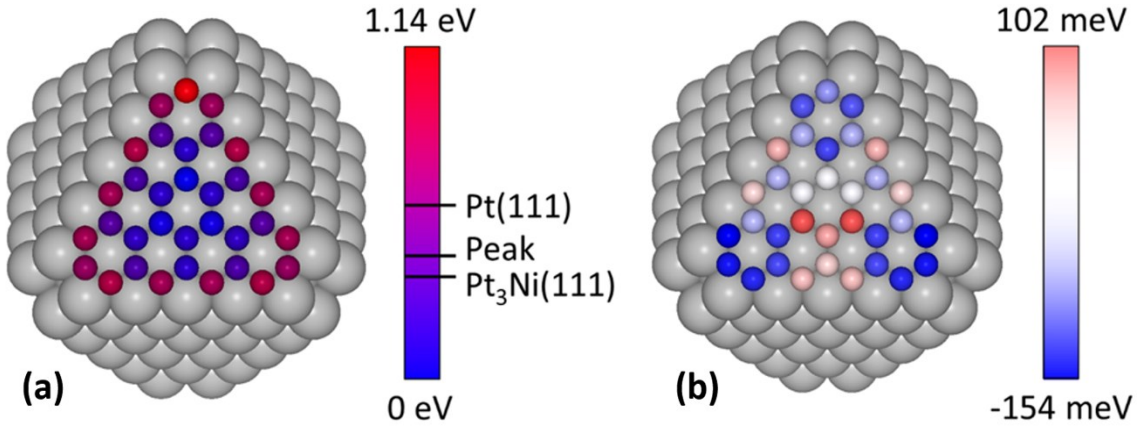

Figure 4.23. DFT calculations results. (a) The calculated binding energies for a single oxygen atom on all fcc and hcp sites on the (111) facet of the $Pt_{178}Ni_{41}Mo_6$ nanoparticle (Figure 4.1), relative to the lowest binding energy. Grey spheres represent Pt and colored spheres represent oxygen sites. Three binding energies are provided for reference: the calculated binding energy on the fcc site of a pure Pt (111) surface, the binding energy corresponding to the peak of the Sabatier volcano[57], and the binding energy on a $Pt_3Ni(111)$ surface. (b) The change in binding energies when a $Pt_{178}Ni_{47}$ nanoparticle is transformed to a $Pt_{178}Ni_{41}Mo_6$ nanoparticle by the substitution of Mo on its energetically favored sites in the second layer below the vertices.

Although the exact mechanisms by which the surface-Mo-doped Pt_3Ni octahedral nanoparticles shows exceptional catalytic performance demand more detailed studies, local changes in oxygen binding energies provide a possible explanation for some of the observed increase in specific activity.[54] A Sabatier volcano of ORR catalysts predicts that ORR activity will be maximized when the oxygen binding energy is ~0.2 eV less than the binding energy on Pt(111).[57] As shown in Figure 4.23(a), my calculations on the $Pt_{178}Ni_{41}Mo_6$ nanoparticle (Figure 4.1) indicate that sites near the particle edge bind oxygenated species too strongly, such as in Pt(111), and sites near the facets of the particles bind oxygenated species too weakly, such as in $Pt_3Ni(111)$. However, compared with the

undoped nanoparticle ($Pt_{178}Ni_{47}$), the oxygen binding energies in the doped nanoparticle ($Pt_{178}Ni_{41}Mo_6$) near the Mo atoms are decreased by up to 154 meV, and binding energies on sites closer to the center of the (111) facet are increased by up to 102meV (Figure 4.23(b)). Thus, if Mo migrates to the thermodynamically favored sites near the particle edges, it may shift the oxygen binding energies on these sites closer to the peak of the volcano plot. Similarly, Mo doping may increase the oxygen binding energies on sites closer to the center of the (111) facet that bind oxygen too weakly. In total, the oxygen binding energies on the surface sites are push to the peak position of volcano plot. As a result of these shifts, some sites may become highly active for catalysis so that the average current of ORR on the surface, defined in Chapter 3 (Eq. (3.20) and Eq. (3.21)), will be highly enhanced.

The DFT-calculated oxygen binding energies in Figure 4.23 were on nanoparticles with a Pt-skin surface, on which both DFT calculations and cluster expansion predictions show that Mo prefers vertex/edge sites in the second layer in vacuum. However, the ORR happens under cell operating conditions (oxidizing conditions) where all Mo atoms prefer vertex/edge sites in the outermost layer (Figure 4.21). I do admit that there is an apparent discrepancy here. Given the oxygen binding energies on Pt_3Ni extended surfaces (Table 3.5) are weaker than the peak of volcano plot, I propose that segregated Mo atoms on the surface of nanoparticles in oxidizing conditions improve the ORR activity not only by enhancing the Pt composition in the second layer (Table 4.3 and Table 4.4), but also by pushing the oxygen binding energies closer to the peak of volcano plot from the right hand side, leading to high ORR activity. A more detailed cluster expansion that can predict the oxygen binding energies on the surface of an octahedral nanoparticle as a function of local

atomic order and oxygen coverage needs to be built to further investigate this proposed explanation that Mo-doping pushes the oxygen binding energies to the peak of volcano plot.

4.5 Summary and discussion

In this chapter, I have used a DFT-based quaternary (Pt/Ni/Mo/Vacancy) cluster expansion to investigate the structure-property relationships for Mo-doped Pt-Ni alloy nanoparticles as a function of size, shape, composition, and internal atomic order. To mimic the electro-chemical environment under cell operating conditions, I extended the cluster expansion model to oxidizing conditions by applying correction terms accounting for the possible presence of oxygenated adsorbates (*O and *OH) on the surface of nanoparticles. Although this approach provides only an approximate model of the effects of an oxidizing environment, it enables us to investigate the stability of Pt-Ni nanoparticles under an applied potential of 0.95 V where the ORR activity is experimentally measured.[54, 58, 61, 146-147]

The key findings of cluster expansion built on Pt-Ni and Pt-Ni-Mo nanoparticles are summarized as follows.[54, 93]

In vacuum, the shape of Pt_3Ni and Mo-doped Pt_3Ni nanoparticles is predicted to be octahedron (Figure 4.1) after annealing from 1500 K to 0 K by simultaneously optimizing the shape and internal atomic order under canonical ensemble with compositions of $Pt_{178}Ni_{41}Mo_6$. The size effect is also investigated: as the size of slightly truncated octahedral Pt_3Ni nanoparticles increases, the composition profile (layer by layer) converges at a size of around 4 nm, which is nearly the size of experimentally-prepared Pt-Ni particles.[54]

For Pt_3Ni nanoparticles in vacuum a Pt-skin structure is identified at low temperatures, and my calculations indicate that Pt and Ni atoms on the edge and vertex sites on the

particle surface are most vulnerable to dissolution (Figure 4.12(a) and (b)). My results of tendency to dissolution in vacuum are inconsistent with the experimental observation of preferential Ni dissolution from Ni-rich facets, and I propose that the discrepancy may be explained by the effects of oxidizing adsorbates on the particle surface (especially on the edges). I predict that the presence of such adsorbates stabilizes the edges of the particle, making edge sites more resistant to dissolution than facet sites (Figure 4.14(a) and (b)). I further proposed that the oxidation of the edges of the particle may drive sub-surface segregation of Pt atoms to the particle edges, explaining the observation of Pt-rich edges in Pt-Ni nanoparticles.[59-60] This effect is supported by calculations on extended Pt-Ni (111) surfaces (Figure 3.14), but it would not be modeled well on a nanoparticle by applying the simple correction terms for *O and *OH used in this chapter, as these terms do not directly capture the interaction between adsorbates and sub-surface metal atoms. A more detailed cluster expansion model, which explicit includes the adsorbates (*O or *OH) on the surface of nanoparticles, needs to be built to further investigate this hypothesis.

My predictions for Pt_3Ni nanoparticles also shown that Ni compositions in the outermost layer are enhanced by a factor of ~33 (especially on vertex and edge sites) because the existence of adsorbed oxygen atoms (*O) and hydroxyl groups (*OH) on the surface pull out Ni atom in the inner layers to the outermost layer (Figure 4.13(a) and (c)). I believe the enhanced Ni compositions on the surface and the relatively high tendency to dissolution on facet and vertex sites are the reasons of the loss of durability and catalytic activity of Pt_3Ni nanoparticles after a particular number (several thousands) of potential cycles using the accelerated durability test (ADT).[54]

For Mo-doped Pt_3Ni nanoparticles, I found that Mo atoms in the inner layers (preferring

vertex and edge sites) in vacuum are pulled to the surface layer on vertex and edge sites and oxidized in oxidizing conditions. Doping a small amount of Mo (1.6% molar) on an octahedral nanoparticle with edge length of about 4 nm reduces the surface Ni composition by a factor of approximately 4, with the greatest reduction occurring on vertex and edge sites (Figure 4.13(c) and (d)). The Pt composition in the second layer increases slightly upon Mo doping, which might contribute to improved catalytic activity since calculations indicate that greater Pt composition in the second layer will push the oxygen adsorption energy closer towards the peak of volcano plot.[92] Moreover, the vacancy formation energies of Pt/Ni atoms on vertex sites are further enhanced by an amount of 250 ~ 500 meV (Figure 4.14), due to the proximity of nearby oxidized Mo atoms. I expect a similar result to hold for other sites with similarly low coordination, suggesting that Mo stabilizes the surface atoms that are most likely to be mobile. The combination of the reduction of equilibrium surface Ni composition and the stabilization of sites with low coordination provides an explanation for why doping a small amounts of Mo atoms (1.6% in molar)[54] can greatly stabilize the shape and composition of octahedral Pt3Ni nanoparticles. Moreover, according to the DFT calculations of oxygen binding energies on the surface of ground state 225-atom nanoparticles (in vacuum; as shown in Figure 4.23), due to Mo doping, the oxygen binding energies on the surface are push forward to be closer to the peak position of volcano plot (Figure 3.15) as to the enhance the average current density of ORR over all the possible binding sites. All of these findings support the highly enhanced stability and improved catalytic activity due to Mo doping.[54]

Chapter 5

CO_2 / CO reduction mechanisms on the Cu nanowires

5.1 Introduction of Cu catalysts for CO_2/CO reduction

Copper (Cu) is a promising electrocatalyst for converting CO_2 and H_2O into synthetic fuels and chemical products. Various nanostructured forms of Cu catalysts synthesized by tailoring the surface morphology, including cuprite-derived electrodes,[80] nanoparticles,[83] and nanowires,[84] were recently reported to be capable of reducing CO_2 into CO, and then further reducing CO into ethanol, both at very low overpotentials (<0.5 V). The active sites of these nanostructures are believed to be correlated with the twin grain boundaries enriched in these high-surface-area catalysts,[79, 157-158] but detailed surface structures accounting for the catalytic enhancements still remain elusive. Early studies on single crystal extended surfaces show that the product distribution of CO_2/CO reduction is structure-sensitive, with CH_4 being favorable on Cu(111) and C_2H_4 on Cu(100).[82, 87, 159]

These work were however performed at very large overpotentials (>1.0 V), which may not be able to explain the low-overpotentials and selective pathways enabled by the nanostructured catalysts. In 2015, in the work of Raciti et al.[84], who are my collaborators, Cu nanowires synthesized from CuO through electrochemical reduction (denoted as ECR) were reported to have low overpotentials (~0.3 V) for CO_2 reduction towards CO(g).

As a follow-up investigation, the same experimental group studied Cu nanowires for electrochemical CO reduction and improved catalytic activity and selectivity by tailoring their nanocrystalline and surface structures.[85] Three types of Cu nanowires with different surface structures were synthesized and investigated: ECR nanowires, nanowires obtained from reduction CuO in forming gas at 150 ºC (denoted as HR-150) and at 300 ºC (denoted as HR-300). ECR and HR-150 nanowires were found to have and high selectivity of CO reduction to C_2 products at very low potentials (-0.2 – -0.4 V). But HR-300 nanowires have low activities for CO reduction. Moreover, the experimental temperature-programed CO desorption (CO-TPD)[85] and electrochemical studies of OH adsorption (OH_{ad})[85] measurement have been used to characterize the surface structures of ECR and HR Cu nanowires. ECR and HR-150 nanowires were found to have relatively higher fractions of coordinately unsaturated Cu(110) facet than HR-300, which is considered to be responsible for the low overpotentials and selective reduction of CO toward oxygenated C_2 products on the Cu nanowires by the experimental group.

To explain the experimentally observed low overpotentials and high selectivity of HR-150 and ECR nanowires, I have constructed free energy diagrams of possible pathways of CO reduction to C_2 products based on density functional theory (DFT) calculations on four different Cu facets: Cu(211), Cu(110), Cu(100) and Cu(111), because experimental data[85]

indicates that these facets are the most prevalent facets on the synthesized Cu nanowire. I have used the RPBE[102-103] exchange-correlation functional with the D3[160] van der Waals contribution in my calculations, as this approach has been shown to result in accurate calculated properties for water and small organic molecules on metal surfaces,[161-164] and it correctly predicts the relative strengths of OH and CO adsorption on the four facets considered here (details are provided in 5.2 Section). To treat the effects of the aqueous solvent on adsorption energies, I have used the VASPsol implicit solvation method.[165-166] Additional details of the DFT calculations are provided in 5.2 Section.

5.2 DFT calculations and free energy calculations

5.2.1 Details of DFT calculations

Electronic structure calculations were performed to find the lowest free-energy pathways for CO reduction to C_2 products. All density functional theory (DFT)[14] calculations were performed with the Vienna Ab initio Simulation Package (VASP)[15-16], in which the Kohn-Sham equations are solved by self-consistent algorithms. The C_GW_new, Cu_pv_GW, H_GW, and O_GW PBE projector-augmented wave (PAW)[101] potentials provided with VASP were used to improve the calculation efficiency, and VASP was run with high precision. The revised Perdew-Burke-Ernzerhof (RPBE)[102-103] exchange-correlation functional was used for all DFT-calculations unless otherwise noted. Van der Waals interactions were accounted for by using the DFT-D3 method[160] (which I will refer to as RPBE-D3). The calculations without inclusion of van der Waals interactions are referred as RPBE calculations. Spin polarization was taken into account in the calculations and the Methfessel–Paxton method[104] of order 2 was employed to determine electron occupancies with a smearing parameter of 0.2 eV. The convergence criteria for the electronic self-consistent iteration and the ionic relaxation loop were set to be 10^{-4} eV and 10^{-3} eV, respectively. To treat the effects of the aqueous solvent on adsorption energies, I have used the VASPsol implicit solvation method.[165-166]

The Brillouin zone was sampled using grids generated by the *k*-point grid server[167] with a minimum distance of 46.5 Å between real-space lattice points. The shift vectors were

automatically chosen to minimize the number of irreducible *k*-points, and the grids were automatically optimized for slab calculations. For all four surface slabs representing different Cu facets, the lattice constant was fixed to the calculated lattice constant for a relaxed bulk Cu fcc crystal (3.65 Å). On the fcc(111) surface, calculations were performed on a 3×3 periodic unit cell with a 4-layer slab and 15 Å of vacuum. The fcc(100) facet used a 3×3 periodic unit cell with a 4-layer slab and 16 Å of vacuum. Also, the fcc(110) facet used a 3×3 periodic unit cell with a 3-layer slab and 16 Å of vacuum. Moreover, the fcc(211) facet used a 4×3 periodic unit cell with a 4-layer slab and 16 Å of vacuum. The unit cells for clean slabs of these four Cu facets: Cu(111), Cu(100),Cu(110) and Cu(211) are as shown in Figure 5.1. For the calculations of binding energies of adsorbates, during structure optimization, the 2 bottom layers were fixed at the optimized bulk positions to mimic the bulk crystal structure beneath the surface, while the adsorbates and the topmost layers were allowed to relax in all directions. For the calculations of free energies of different facets, all atoms are allowed to fully relax. I have tested for the convergence with respect to slab thickness in terms of surface energies of clean slabs and *CO adsorption energies on all four fcc(111), fcc(100), fcc(110) and fcc(211) facets. The convergence criteria for surface energy and *CO adsorption energy were 1~2 meV/Å^2 and 10 meV, respectively.

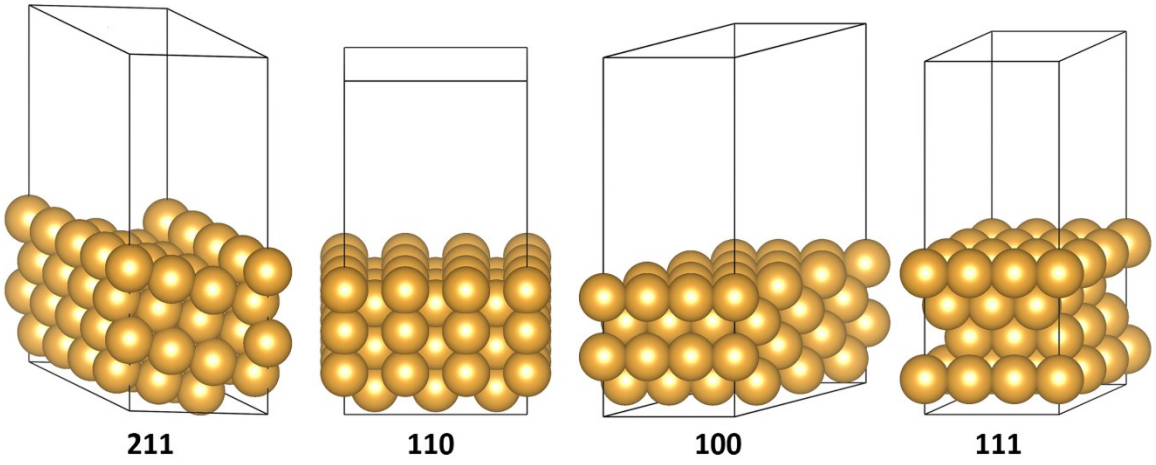

Figure 5.1. Unit cells for clean slabs of these four Cu facets: Cu(111), Cu(100),Cu(110) and Cu(211). Golden spheres represent the Cu atoms.

5.2.2 Computational hydrogen electrode (CHE) model

In the computational hydrogen electrode (CHE) model[55], at 0 V versus RHE, the chemical potential of a proton-electron pair, $\mu(\mathrm{H}^+)+\mu(\mathrm{e}^-)$ is equal to half of the chemical potential of gas-phase hydrogen molecule $\frac{1}{2}\mu(\mathrm{H_2(g)})$ at 101,325 Pa, at all pH values, and at all temperatures. Thus, the chemical potential of the proton-electron pair can be adjusted as a function of applied potential by the standard relation between chemical and electrical potential, $\Delta\mu = -eU$. Thus, the total value of $\mu(\mathrm{H}^+)+\mu(\mathrm{e}^-)$ as a function of applied potential at all temperature, and pH values can be expressed as follows:

$$\mu(\mathrm{H}^+)+\mu(\mathrm{e}^-)=\frac{1}{2}\mu(\mathrm{H_2(g)})-\mathrm{eU}. \tag{5.1}$$

The free energy change for each intermediate step that involves an electron transfer will be a function of the applied electrical potential (U). As the electrical potential is lowered

to more negative in the CHE model, the free energies of the adsorbates with n pairs of electron-proton transfer referenced to CO(g) will decrease by ne$U$. The entire reduction pathway will become exergonic (downhill in the free energy diagram from left to right) when the applied potential is sufficiently low. The potential at which the pathway first becomes exergonic is the calculated lower bound for the onset potential of the pathway.

5.2.3 Free energy calculations

I calculated the free energy change of the CO reduction intermediates at zero potential (U=0) as,

$$\Delta G(U=0) = \Delta E_{DFT} + \Delta ZPE - T\Delta S + \Delta\int C_P \mathrm{d}T \,, \tag{5.2}$$

where ΔE_{DFT} is the electronic energy for the intermediate step of the CO reduction directly obtained from DFT calculations, ΔZPE is the difference in zero point energies corresponding to the certain reaction, ΔC_P is the difference in constant-pressure heat capacities, ΔS is the change in entropy, and T is the temperature (I choose291.65K, to be consistent with the work of Peterson et al.[55]). Values for the last three terms in Eq. (5.2) are are listed in Table 5.1 and Table 5.2 below.

At an applied potential U, the total change in free energy is calculated by

$$\Delta G(U) = \Delta E_{DFT} + \Delta ZPE - T\Delta S + \Delta\int C_P \mathrm{d}T - eU \,. \tag{5.3}$$

Here, e is the number of $(H^+ + e^-)$ that have been transferred.

Table 5.1. Zero point energies corrections ($ZPEs$), enthalpic temperature corrections ($\int C_p dT$), and entropy contributions (TS) for adsorbed species in this chapter. Here, the data for *H, *CO, *CHO, and *COH are from the work of Peterson et al.[168] The data for *COCHO, *COCOH, and *OCHCHO* are from the work of Calle-Vallejo et al.[86]

adsorbate	*ZPE* (eV)	*TS* (eV)	$\int C_p dT$ (eV)
*H	0.16	0.007	0.005
*CO	0.192	0.153	0.076
*CHO	0.444	0.184	0.086
*COH	0.451	0.11	0.068
OCHCHO	1.03	0.22	0.12
*COCHO	0.68	0.25	0.12
*COCOH	0.70	0.24	0.12

Table 5.2. Zero point energies corrections ($ZPEs$), enthalpic temperature corrections ($\int C_p dT$), and entropy contributions (TS) for non-adsorbed species used in this chapter are from the work of Peterson et al.[168], and the data for C_2H_2 and C_2H_6 are from the work of Calle-Vallejo et al.[86]

species	*ZPE* (eV)	*TS* (eV)	$\int C_p dT$ (eV)
CO_2	0.31	0.65	0.10
CO	0.14	0.61	0.09
H_2	0.27	0.42	0.09
H_2O	0.58	0.65	0.10
CH_4	1.20	0.60	0.10
C_2H_2	0.72	0.62	0.10
C_2H_4	1.36	0.71	0.11
C_2H_6	1.98	0.71	0.11
H_2(ref)	0.27	0.39	0.09

5.2.3.1 Free energies of adsorbates

The electronic energies of all intermediate states reported in this chapter are calculated using the lowest-energy bonding sites and optimized geometries for *CO, 2*CO, *CHO,

*COH, *CO+*CHO, 2*CHO, *OCHCHO*, *COCHO, and *COCOH. ΔE_{DFT} for adsorbates are calculated as the electronic energy of the state minus the electronic energy of corresponding clean slab (Cu(211), Cu(110), Cu(100) and Cu(111)), with C atoms referenced to graphene, H atoms to 1/2 H_2, and O atoms to (H_2O-H_2). Here is an example for *CO,

$$\Delta E_{DFT}(*\mathrm{CO}) = E_{DFT}(*\mathrm{CO}) - \mathrm{E}_{DFT}(*) - \mathrm{E}(\mathrm{C(graphene)}) - \mathrm{E}(\mathrm{H_2O}) + E(\mathrm{H_2}), \quad (5.4)$$

where $E(\mathrm{O}) = E(\mathrm{H_2O}) - E(\mathrm{H_2})$.

5.2.3.2 Gas-phase corrections for CO_2(g) and CO(g)

In the work of Blaylock et al.[169], the gas-phase thermodynamic reaction energies calculated using RPBE functional were particularly inconsistent with experimental reference values. In this chapter, the CO reduction involves gas-phase molecules of CO, H_2, and H_2O, and the initial state of free energy diagrams is the free energy of CO(g). Thus I evaluated whether it was necessary to apply a gas-phase free-energy correction to my DFT calculations by comparing calculated and experimental gas-phase reaction enthalpies at 25 ºC and 101325 Pa, using the same method in reference 168. The reactions I chose are listed in Table 5.3. As shown in Table 5.4, the average and standard deviation of reaction enthalpy errors (ΔH) for RPBE gas-phase values in reactions containing CO(g) are -0.04 eV and 0.02 eV, respectively, which are relatively small. In reactions containing CO_2(g), the average and standard deviation of ΔH are 0.32 eV (larger than 0.2 eV, which is consistent with the value in reference 168) and 0.02 eV. Thus, I decided not to apply any gas-phase free energy correction to CO(g), and apply gas-phase free energy correction to CO_2(g) by 0.32 eV for the DFT (RPBE) calculations in this chapter.

Table 5.3. Reactions analyzed for gas-phase ΔH comparison (at $25\ ^oC$ and 101325 Pa).

Reaction #	Reactions containing	Stoichiometry
0	CO_2(g)	$4H_2 + CO_2 \rightarrow CH_4 + H_2O$
1		$7/2H_2 + CO_2 \rightarrow 1/2C_2H_6 + 2H_2O$
2		$3H_2 + CO_2 \rightarrow 1/2C_2H_4 + 2H_2O$
3		$5/2H_2 + CO_2 \rightarrow 1/2C_2H_2 + 2H_2O$
4	CO(g)	$3H_2 + CO \rightarrow CH_4 + H_2O$
5		$5/2H_2 + CO \rightarrow 1/2C_2H_6 + H_2O$
6		$2H_2 + CO \rightarrow 1/2C_2H_4 + H_2O$
7		$3/2H_2 + CO \rightarrow 1/2C_2H_2 + H_2O$

Table 5.4. Reaction enthalpies (eV) of reactions (for RPBE gas-phase values) listed Table 5.3, are compared with the experimental reference values ΔH_{ref}, which are from NIST.[170]

Reaction #	Reactions containing	ΔH_{ref}/eV	ΔH/eV	Error $(\Delta H - \Delta H_{ref})$/eV
0	CO_2(g)	-1.71	-1.40	0.31
1		-1.37	-1.04	0.33
2		-0.66	-0.35	0.31
3		0.25	0.59	0.34
4	CO(g)	-2.14	-2.20	-0.06
5		-1.8	-1.84	-0.04
6		-1.09	-1.14	-0.05
7		-0.19	-0.20	-0.01
	Average of errors for reactions containing CO_2(g)			0.32
	Standard deviation of errors for reactions containing CO_2(g)			0.02
	Average of errors for reactions containing CO(g)			-0.04
	Standard deviation of errors for reactions containing CO(g)			0.02

5.2.4 Comparison of RPBE, RPBE-D3, and optB86b

5.2.4.1 Trend of binding energies for both CO and OH on Cu facets

To evaluate the ability of different exchange-correlation functionals to accurately model adsorption energies I have calculated OH and CO binding energies using both RPBE and RPBE-D3. I have also evaluated the optB86b-vdW functional[171-173] (which I will refer to as optB86b) as a potential alternative to RPBE-D3. The experimental order of *OH binding strength is Cu(211) > Cu(100) > Cu(110) > Cu(111), and the experimental order of *CO binding strength is Cu(211) > Cu(110) > Cu(100) > Cu(111).[85, 174-175] As shown in Table 5.5 and Table 5.6, among the RPBE, RPBE-D3, and optB86b methods, RPBE-D3 is the only functional I tested that gets the order of adsorbate binding energies on Cu surfaces in agreement with experiments for both CO and OH. RPBE is in agreement with experiments for CO but not OH; optB86b method is in agreement with experiments for OH but not CO.

Table 5.5. OH binding energies in solvation using three different DFT approaches, RPBE, RPBE-D3, and optB86b, compared with the experimental order of OH_{ad} (Cu(211) > Cu(100) > Cu(110) > Cu(111)).[85] The effects of the aqueous solvent on adsorption energies were treated via the VASPsol implicit solvation model.[165-166]

	OH binding energy in solvation relative to Cu(111) (kJ/mol)			
	Cu(211)	Cu(110)	Cu(100)	Cu(111)
RPBE	38.7	15.5	11.0	0
RPBE-D3	32.9	14.3	16.3	0
optB86b	22.2	2.9	12.3	0

Table 5.6. CO binding energies in gas phase using three different DFT approaches, RPBE, RPBE-D3, and optB86b, compared with the order of experimental CO TPD data (Cu(211) > Cu(110) > Cu(100) > Cu(111)).[85]

	CO binding energy in gas phase (kJ/mol)			
	Cu(211)	Cu(110)	Cu(100)	Cu(111)
RPBE	69.9	63.2	57.7	50.9
RPBE-D3	96.1	95.0	91.4	75.4
optB86b	99.1	95.3	93.1	94.4
experimental CO TPD[85]	71.4	62.9	56.1	49.1

Moreover, I note that RPBE-D3 likely overestimates the free energy change from *CO to *CHO, as it is known to anomalously overbind CO.[161, 176] On the other hand, RPBE without the van der Waals correction calculates CO adsorption energies that are close to experimental values.[114, 177] Using RPBE, I calculate CO adsorption energies of 70, 63, 58, and 51 kJ / mol on the (211), (110), (100), and (111) facets respectively (Table 5.6 and Figure 5.2(a)), which are in excellent agreement with the experimental energies of 71, 63, 56, and 49 kJ / mol on the (211), (110), (100) and (111) derived from the CO TPD data on HR-150 nanowires.[85] The data in Table 5.7 suggests that the RPBE-D3 free energies for *CO are about 0.3 eV too low. Thus, for the free energy diagrams I draw in this chapter, to correct for this error of *CO, I have used plain RPBE to calculated the adsorption energies of *CO and 2*CO, used an average of the RPBE and RPBE-D3 values to calculate the adsorption energy of *CO+*CHO, and used the RPBE-D3 adsorption energies for other adsorbates.

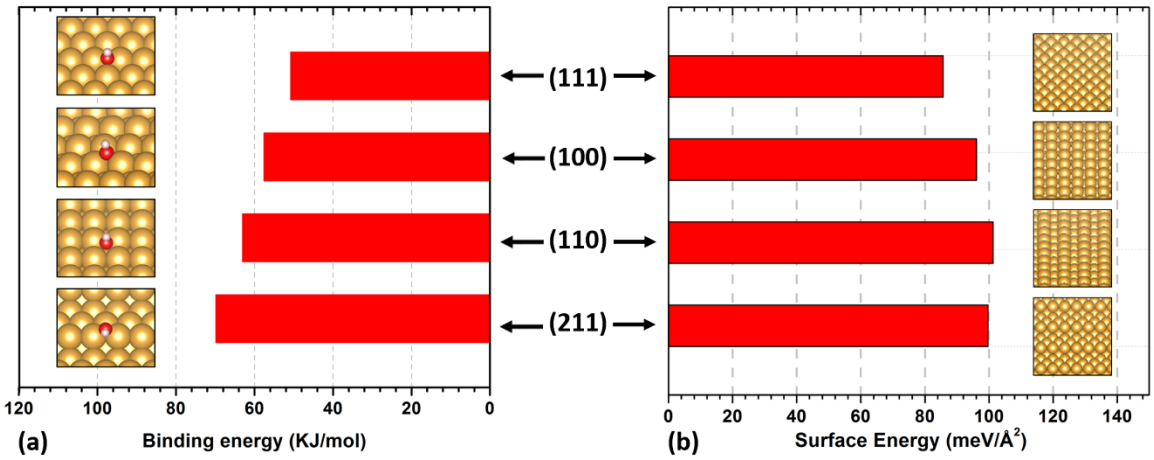

Figure 5.2. The DFT-calculated (a) CO binding energies on four different Cu facets using RPBE, and (b) surface energies of four different Cu facets using PBEsol[178] functional (details in 5.2.5 Section).

5.2.4.2 Comparison of free energies between RPBE and RPBE-D3

Table 5.7. Comparison of free energies for *CO, *CHO, *COH and *COCHO on four different facets, which are referenced to clean slab, with C atoms referenced to graphene, H atoms to 1/2 H_2, and O atoms to (H_2O-H_2).

Cu facet	*CO (eV)		*COH (eV)		*CHO (eV)		*COCHO (eV)	
	RPBE	RBPE-D3	RPBE	RPBE-D3	RPBE	RPBE-D3	RPBE	RPBE-D3
(211)	-0.24	-0.51	1.17	0.65	0.57	0.22	0.88	0.31
(110)	-0.19	-0.49	1.34	0.97	0.59	0.08	0.74	-0.03
(100)	-0.12	-0.46	0.77	0.24	0.76	0.28	0.90	0.14
(111)	-0.06	-0.32	1.10	0.78	0.89	0.48	1.34	0.49

5.2.5 Surface energies for Cu and CuO crystals

The surface energies of the different Cu and CuO facets were performed using spin-polarized DFT calculations with the PBEsol[179] exchange correlation functional. The PBEsol exchange-correlation functional has been shown to give more accurate results for surface energies for different metals than RPBE[177, 180] including of Cu.[181] To correct for the tendency of DFT to over-delocalize the electrons in transition-metal oxides such as CuO, we have used the DFT+U method as developed by Dudarev et al.[182] with a $U_{\text{eff}} = U - J$ value of 6.52 eV[183] for CuO surfaces. All CuO slabs and Cu slabs are (1x1) primitive cells with thicknesses of greater than 15 Angstroms. The vacuum layers in between are also greater than 15 Angstroms thick.

The surface energy of a facet is defined in Eq. (3.1). The calculated surface energies for different Cu and CuO facets are listed in Table 5.8 and Table 5.9.

Table 5.8. DFT-calculated surface energies for various Cu facets.

	Facet	Surface energy (meV/Å^2)	Surface energy (J/m^2)
Cu	(1 0 0)	94.85	1.518
Cu	(1 1 0)	100.35	1.606
Cu	(1 1 1)	84.58	1.353
Cu	(2 1 1)	96.84	1.549

Table 5.9. DFT-calculated surface energies for various CuO facets. Here, * stands for oxygen terminated surfaces. This table was created based on the calculations from my collaborator, Chenyang Li.[85]

	CuO Facet	Equivalent Cu facet	Surface energy (meV/Å^2)	Surface energy (J/m^2)	Reference values (Mishra et al.[184]) (J/m^2)
CuO	*(0 1 0)	Cu (100)	90.21	1.44	1.35
CuO	(0 0 1)		106.71	1.71	-
CuO	*(1 0 0)		110.87	1.77	1.68
CuO	(1 0 0)		112.53	1.80	1.83
CuO	*(0 1 1)	Cu (110)	64.58	1.03	0.94
CuO	(0 1 -1)		64.25	1.03	-
CuO	(1 0 1)		71.64	1.15	1.17
CuO	(1 0 -1)		76.81	1.23	-
CuO	(1 1 0)		85.70	1.37	1.37
CuO	(-1 1 0)		91.96	1.47	-
CuO	(1 1 1)	Cu (111)	50.84	0.81	0.75
CuO	(1 -1 -1)		62.63	1.00	0.89
CuO	(1 1 -1)		66.94	1.07	-
CuO	(1 -1 1)		82.17	1.31	-
CuO	(1 1 2)	Cu (211)	91.25	1.46	-
CuO	(1 2 1)		93.71	1.50	-
CuO	(2 1 1)		100.51	1.61	-

5.3 Free energy diagrams of CO_2/CO reduction

I consider two steps for the reduction of CO_2/CO on each of these surfaces. In the first step, CO_2(g)/CO(g) reduce to C_1 products. In the second step, CO(g) reduces to C_2 products. For the reduction of CO on each of these facets (Cu(211), Cu(110), Cu(100) and Cu(111), three possible paths are considered. The first two paths start with the protonation of adsorbed CO (denoted *CO) to form either *COH or *CHO.[88, 185-186] The third path involves the direct coupling of CO molecules to form an $OCCO^{\delta-}$ dimer as an intermediate species.[86] This mechanism has been proposed to explain the observation that on the Cu(100) surface C_2 products are formed at low overpotentials (versus RHE) without the formation of C_1 products.[82, 87] The CO dimer is believed to become negatively charged prior to a proton transfer, which would explain the observed pH-dependence of the overpotential on the Cu(100) facet versus the RHE.

To model these mechanisms, I have used the computational hydrogen electrode (CHE)[55] approach (details are provided in Section 5.2), which the free energy of ($H^+ + e^-$) is calculated using the fact that ($H^+ + e^-$) is in equilibrium with (1/2)H_2(g) at zero potential versus RHE. The calculated onset potential is the smallest applied potential (in absolute value) at which all reaction steps become exergonic. The onset potentials I calculate are estimates of the lower bounds of the true onset potentials, as I do not include intermediate states for which the uncertainty in the free energy is high. Specifically, I do not calculate the free energies of the unstable transition states between intermediates, as these depend

on the exact path of the transition and the molecular structure of the solvent, which I have not investigated here. However such kinetic effects may be important, for example, in differentiating the *CHO and *COH pathways in aqueous solution if the free energies of *CHO and *COH are similar.[185, 187] In addition, I do not calculate the free energy of the changed $*OCCO^{\delta-}$ intermediate in the CO-CO coupling mechanism, which depends on both the pH and the applied potential. Accurately calculating the free energy of this intermediate using DFT is challenging; different approaches for calculating the free energy for the transition from 2*CO to $*OCCO^{\delta-}$, involving different treatments of solvent and the applied potential, produce values that differ by more than 1 eV.[91, 188]

5.3.1 Free energy diagrams for CO_2/CO reduction to C_1 products

As reported in the work of Daciti et al.[84], for electrochemical reduced Cu nanowires (ECR nanowires), CO(g) is the dominate product of CO_2(g) reduction at low potentials (-0.2 V – -0.5 V). The overpotential is as low as 0.3 V when the product of CO_2 reduction has 60% of CO(g).[84] The reaction pathway of CO_2(g) reduction to CO(g) is expressed as:

$$CO_2(g) \rightarrow *COOH \rightarrow *CO \rightarrow CO(g). \quad (5.5)$$

The corresponding free energy diagrams for Eq. (5.5) are shown in Figure 5.3. The calculated onset potentials for CO_2(g) to CO(g) is -0.34, -0.26, -0.58, and -0.75 V on the (211), (110), (100), and (111) facets, respectively. The Cu(110) has the lowest

computational onset potential (-0.26 V), whose absolute value is closest to the experimental overpotential (0.3 V).[84] Thus I believe Cu(110) facet is responsible for the low observed overpotentials for CO_2(g) reduction to CO(g) for ECR nanowires.

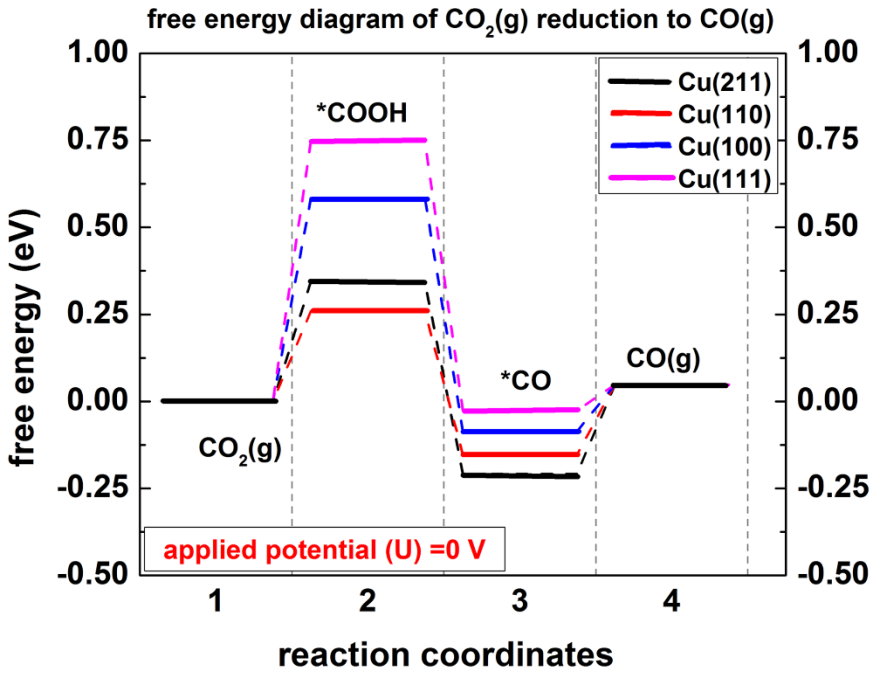

Figure 5.3. Free energy diagrams of CO_2 reduction to CO(g) on four Cu facets, Cu(211), Cu(110), Cu(100) and Cu(111), at an applied potential of zero, with the corresponding onset potentials of -0.34 V, -0.26 V, -0.58 V and -0.75 V, respectively. Here, I use the RPBE adsorption energies for *CO, and the RPBE-D3 adsorption energies for *COOH.

Further reduction of CO(g) is necessary to convert CO_2 into synthetic fuels and chemical products. For CO(g) reduction to C_1 products, the key step is the protonation of adsorbed CO (denoted *CO) to form either *COH or *CHO, as expressed as follow.

$$CO(g) \rightarrow *CO \rightarrow *CHO \text{ (or } *COH). \quad (5.6)$$

My calculations (Table 5.7) show that the formation of *CHO is more thermodynamically favorable than the formation of *COH on Cu(211), Cu(110) and Cu(111) facets, consistent with previous studies.[185, 189] On the Cu(100) facet, I find that the free energy states of *COH and *CHO are similar to each other. As shown in Table 5.7, using RPBE-D3 approach, *COH is thermodynamically more stable than *CHO by about 40 meV; using RPBE without inclusion of van der Waals interactions, *CHO is more stable than *COH by about 10 meV. Previous computational works have predicted that subsequent protonation of *CHO is relatively facile compared with protonation of *CO to form *CHO.[88, 168, 185, 190] There are various C_1 products, such as CH_4, CH_3OH, HCOOH, and so on, which I do not discuss here. On the (110) facet, the free energy of *CHO is 891 meV less than the free energy of *COH. The magnitude of this difference suggests that the *CHO path would be preferred on this surface even if kinetics were fully considered. From now on, I will consider *CHO as the next intermediate after the protonation of *CO in this chapter.

According to my calculations, I would like to point out that the onset potential for the *CHO pathway ($CO(g) \rightarrow *CO \rightarrow *CHO$) is lowest on the (110) facet (Figure 5.4). As shown in Figure 5.4, the predicted onset potentials from *CO to *CHO on Cu(211), Cu(110), Cu(100), and Cu(111) facets are -0.46 eV, -0.27 eV, -0.41 eV, and -0.51 eV respectively, which are much lower than the values predicted by previous computational works by an amount of about 300 meV.[168, 187, 190] On Cu(211) facet, the calculated rate-limiting step for CO_2 reduced to CH_4 was reported to be from *CO to *CHO with a free energy barrier of 0.74 eV at an applied potential of zero.[168] In the work of Durand et al.[190], the free energy barriers from *CO to *CHO are about 0.7 eV, 0.8 eV, and 0.9 eV for Cu(211), Cu(100) and Cu(111) facets respectively. My calculated free energy barriers are much

lower than these values primarily due to the inclusion of van der Waals interactions. I find that the inclusion of van der Waals interactions, which is often necessary to get accurate adsorption energies for organic molecules,[191-193] reduces free energy barriers by significantly increasing the adsorption energies for hydrogenated adsorbates. Table 5.7 shows the difference of free energies between RPBE and RPBE-D3 for various adsorbates.

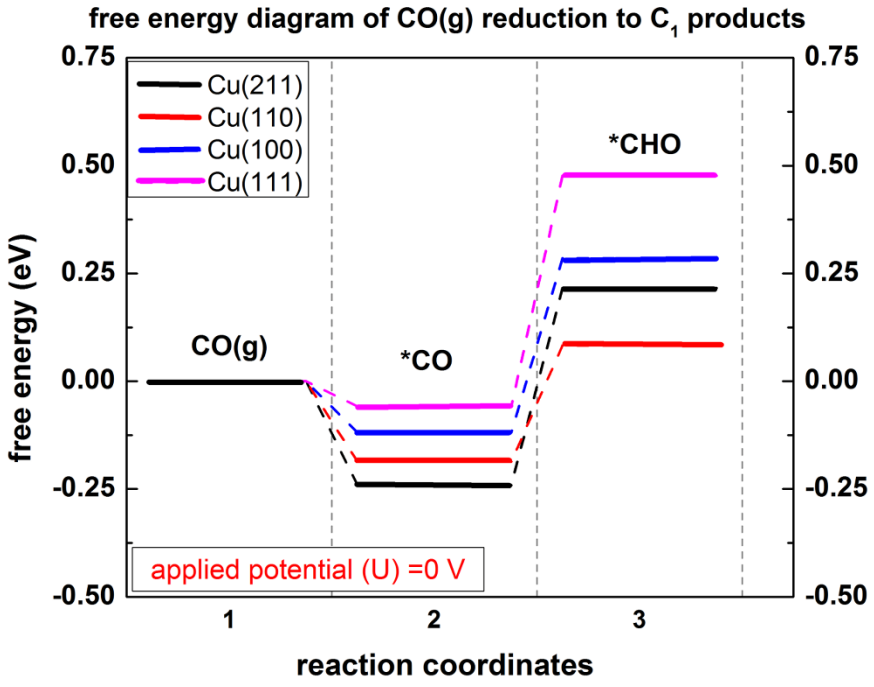

Figure 5.4. Free energy diagrams of CO reduction via *CHO pathway (CO(g) → *CO → *CHO) on four Cu facets, Cu(211), Cu(110), Cu(100) and Cu(111), at an applied potential of zero, with the corresponding onset potentials of -0.46 V, -0.27 V, -0.41 V and -0.51 V, respectively. Here, I use the RPBE adsorption energies for *CO, and RPBE-D3 adsorption energies for *CHO.

5.3.2 Free energy diagrams for CO reduction to C_2 products

For CO(g) reduction to C_2 products, I will discuss two competing C-C coupling mechanisms, CHO-CHO coupling and CO-CO coupling mechanisms. The difference between them is that C-C bond forms after the protonation of *CO to *CHO for CHO-CHO coupling mechanism, but C-C bond forms without the protonation of *CO to *CHO for the later mechanism.

5.3.2.1 CHO-CHO coupling mechanism

For the CHO-CHO coupling mechanism, it has been proposed that C_2 species form via an *OCHCHO* intermediate after the formation of *CHO,

$$2CO(g) \rightarrow CO(g) + *CO \rightarrow 2*CO \rightarrow *CO+*CHO \rightarrow 2*CHO \rightarrow *OCHCHO*, \quad (5.7)$$

and after the formation of *OCHCHO* additional protonation to form C_2 products should proceed rapidly.[88] On all four surfaces, I predict the coupling of carbon atoms to form *OCHCHO* to be relatively facile (Figure 5.5(a)), so that the rate-limiting step for the *OCHCHO* path is the protonation of *CO to form *CHO. As discussed in 5.2 Section, if I use the RPBE adsorption energies for *CO and 2*CO instead of the RPBE-D3 energies, and use an average of the RPBE and RPBE-D3 adsorption energies for *CO+*CHO, the calculated minimum onset potentials of CHO-CHO coupling mechanism are -0.46, -0.36, -0.45, and -0.57 V on the (211), (110), (100), and (111) facets respectively (Figure 5.5(a)), indicating that the (110) surface would be most active for this mechanism. The rate-

limiting step in the pathway of Eq. (5.7) is $2^*CO \rightarrow {}^*CO + {}^*CHO$ on all four facets. These calculated onset potentials are somewhat lower than other studies,[168, 185, 190] but are in agreement with the experimentally-observed low potentials of -0.2 – -0.4 V for C_2 production on ECR and HR-150 nanowires.[85] This is likely because I do not calculate the free energies of transition states, and because I include van der Waals interactions in my calculations for adsorbates other than CO. To my knowledge, this is the first time that van der Waals interactions have been included into the calculations of the free energy diagrams for CO_2/CO reduction.

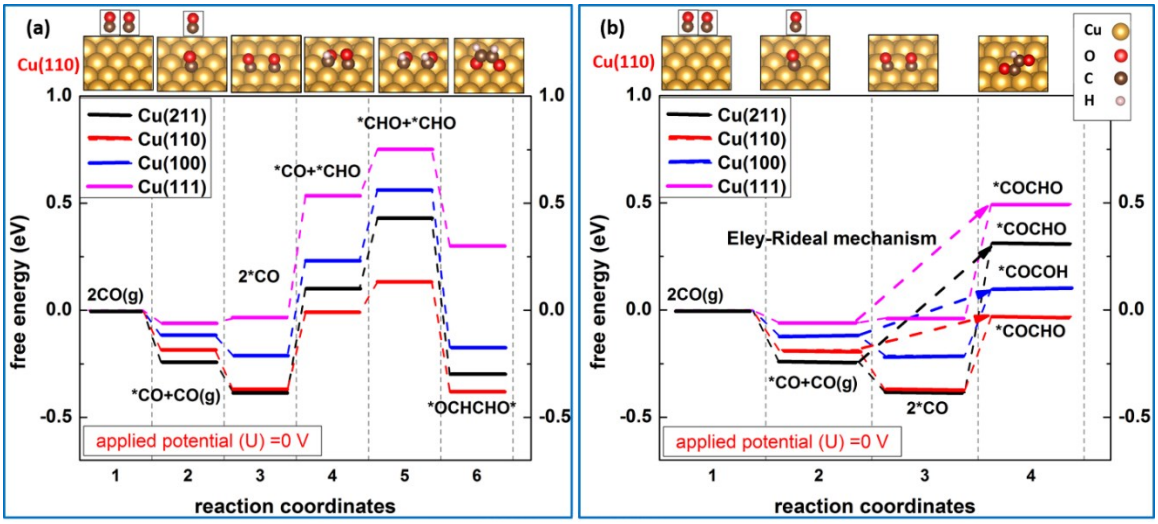

Figure 5.5. Free energy diagrams for CO reduction to C_2 products via (a) the CHO-CHO coupling mechanism, and (b) the CO-CO coupling mechanism. The dashed arrows in (b) represent possible CO-CO coupling through an Eley-Rideal mechanism. The likely formation of $^*OCCO^{\delta-}$ between steps 3 and 4 is not included for reasons discussed in the text. The illustrations of the configurations of surface adsorbates are on the Cu(110) facet.

5.3.2.2 CO-CO coupling mechanism

I find a similar trend of calculated onset potentials for the CO-CO coupling pathway:

$$2CO(g) \rightarrow CO(g) + *CO \rightarrow 2*CO \rightarrow *COCHO \text{ (or } *COCOH). \quad (5.8)$$

As shown in Figure 5.5(b), the calculated lower bounds on the onset potentials, again using the RPBE value for the free energy of *CO, are -0.69, -0.34, -0.31, and -0.52 V on the (211), (110), (100), and (111) surfaces, respectively. The rate-limiting step is

$$2*CO + H^+ + e^- \rightarrow *COCHO \text{ (or } *COCOH). \quad (5.9)$$

Alternatively, CO-CO coupling could occur through an Eley-Rideal mechanism:

$$*CO + CO(g) + H^+ + e^- \rightarrow *COCHO \text{ (or } *COCOH). \quad (5.10)$$

In this case, the calculated lower bounds on the onset potentials are -0.55, -0.16, -0.22, and -0.54 V on the (211), (110), (100), and (111) surfaces respectively. In both of the above steps, I have skipped over the likely formation of the $*OCCO^{\delta-}$ intermediate, due to the aforementioned uncertainty in the calculated free energy for this species. Under conditions in which the $*OCCO^{\delta-}$ state has greater free energy than *COCHO (or *COCOH), the onset potentials would be higher than the lower bounds listed above. However at sufficiently high pH, the free energy of the $*OCCO^{\delta-}$ state will drop below the free energies of *COCHO and *COCOH. The CO-CO coupling mechanism could potentially then proceed on the (110) surface at very low potentials versus the RHE.

5.4 Summary and discussion

Although my calculations of free energy diagrams indicate that the Cu(110) surface could be capable of reducing CO to C_2 products at very low onset potentials (about -0.3 – -0.4 V, shown in Figure 5.5). It may not be present on polycrystalline Cu samples because of its high surface energy (Figure 5.2 (b), and Table 5.8), and it does not show up on a calculated Wulff construction of the equilibrium crystal shape for Cu.[178] To understand why the Cu(110) surface is present on the reduced nanowires, we consider the "equivalent" CuO surfaces, which are those that would relax to a Cu(110) surface if all oxygen disappeared from a CuO crystal. Figure 5.6 shows that a CuO(011) surface and its corresponding Cu(110) surface are aligned so that this transition is apparent. We similarly consider CuO surfaces that are equivalent to Cu(211), Cu(100), and Cu(111). The calculated surface energies of these surfaces are provided in Table 5.9 (based on the calculations of my collaborator, Chenyang Li). The surfaces with the lowest surface energy are equivalent to the Cu(111) surface, followed closely by the CuO(011) surface, which is equivalent to the Cu(110) surface. Thus it is likely that CuO(011) surfaces are present in the CuO nanowires, and upon reduction, some of them may transform into Cu(110) surfaces. Because the Cu(110) surfaces are not thermodynamically stable, they will disappear after annealing at sufficiently high temperature for sufficiently long time, explaining why ECR and HR-150 nanowires have a much higher percentage of Cu(110) facets than HR-300 nanowires. Together with the predicted low onset potentials (about -0.3 – -0.4 V) on Cu(110) facet

(Figure 5.5), I are confident to argue that the experimentally-observed low overpotentials and high selectivities for CO reduction to C_2 products on ECR and HR-150 nanowires are attributed to the high percentage of the Cu(110) facet.

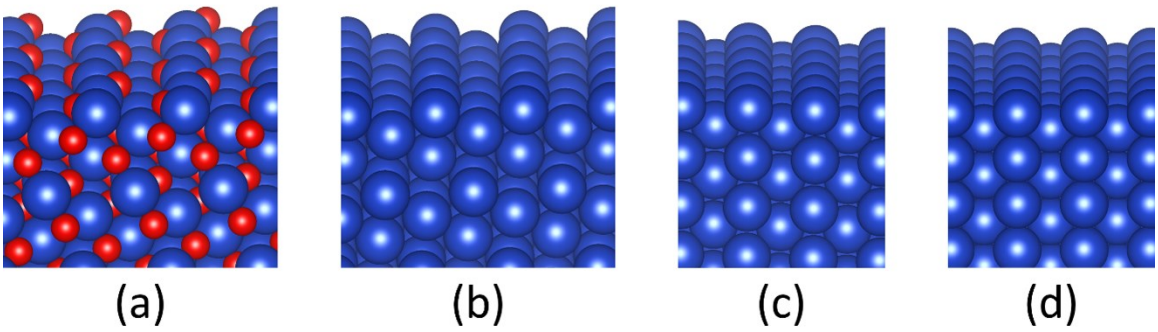

Figure 5.6. (a) The low-energy CuO(011) surface (b) The CuO(011) surface with oxygen atoms removed. (c) The CuO(011) surface with oxygen atoms removed and subsequent relaxation of atomic positions using density functional theory. (d) The high-energy Cu(110) surface. The blue spheres represent the Cu atoms, and red represent the oxygen atoms.

Chapter 6

Future work

6.1 Extension of cluster expansion

Having using cluster expansion models to investigate structure-property relationships of Pt-Ni catalysts at the atomic scale, additional work needs to be done to generalize my results to more realistic Pt-Ni catalysts.

In Chapter 3, I built a cluster expansion on the extended surfaces with the limitation that lattice parameter of the Pt-Ni(111) surface structures in training set was fixed to that of bulk Pt_3Ni. However, when experimentally synthesizing extended alloy surfaces or nanoparticles by alloying Pt atoms with transitional metals (Ni and Mo in this thesis), size effects, composition effects, and sub-surface structures (such as core-shell nanoparticles[194]) can result in a range of different lattice parameters. Moreover, I do know that lattice parameters in the near surface of catalysts do affect the catalytic properties.[73, 194] It will be interesting that the relaxed lattice parameter dependence and catalytic activity dependence could be investigated using cluster expansion built on Pt-Ni extended surface with the

changeable lattice constants. The strategy is to create two sets of cluster expansions for one given set of training set. One cluster expansion is fitted to the formation energies of training structures and the one is fitted to the relaxed local lattice parameters of training structures.

In Chapter 4, I built a cluster expansion on nanoparticles without including surface oxygen adsorbates (or *OH) into the training set, which prohibits us to predict the effects of an oxidizing conditions on the stability and activity of Pt-Ni nanoparticles through the direct interactions between adsorbed oxygen and sub-surface sites. To better mimic oxidizing environment of cell operation, I are currently developing a cluster expansion (Pt-Ni-Mo-O) built on 225-atom (Pt/Ni/Mo) nanoparticles with a monolayer of oxygen/vacancy on the surface of nanoparticles, which is capable of more accurate predicting the effects of adsorbed oxygen on the structure and stability of Pt-Ni nanoparticles in oxidizing conditions.

Recently, the fabrication of hollow nanoparticles[58, 62, 195] instead of solid ones becomes one of the strategies for researchers to tailor the surface morphology and composition to explore the potential catalysts with optimal durability and catalytic activity. For instance, initially beginning with $PtNi_3$ polyhedral nanoparticles, Pt-rich nanoframes with high durability and ORR activity were synthesized through the interior erosion.[58] Also, to synthesize the Pt-based nanocages[62, 195], Pt atoms were deposited on the surface of palladium (Pd) nanoparticles at first place, then Pd atom were etched away so as to leave Pt atoms on the edges of nanoparticles.

Moreover, the understanding of growth and dissolution processes of nanocrystals may enable rational design of catalysts with desired properties. Recently, Gan et al.[141] experimentally followed the anisotropic growth process of Pt-Ni octahedral nanoparticles,

and revealed that Pt-rich phase on the vertex and edge sites were initially formed, then followed by the deposition of Ni atoms to the facet sites, which explains the experimental observation by the same research group that the Ni dissolution of Pt-Ni octahedral nanoparticles starts from facet sites, leading to the formation of concave octahedra.[59] Thus, it has merit if I can build a cluster expansion that allows for the diffusion of metal atoms (e.g. Pt/Ni atoms) in the inner layers of nanoparticles, so as to enable kinetic Monte Carlo simulations. Hopefully, this kinetic model is able to mimic the growth and dissolution process under different chemical potentials, temperatures, applied potentials at a variety of realistic catalytic systems.

I am continuing to extend my cluster expansion approach in ways that address these interesting problems mentioned above. Although, in this thesis I only have demonstrated that how the cluster expansion could be used to investigate the binary Pt-Ni and ternary Pt-Ni-Mo alloy catalysts, without loss of generality, the cluster expansion approaches developed on both extended surfaces and nanoparticles also can be used to other materials systems, such as Pt-Cu, Au-Pd, and so on.

6.2 CO_2/CO reduction mechanisms

Recently, the CO_2/CO reduction is a popular topic for both experimentalists and theorists. To improve the electrocatalytic performance of CO_2/CO reduction, different synthesis strategies have been adopted to tailor the surface structures of Cu catalysts, such as, control the particle size,[83] surface roughness,[80] and alloy Cu with other metals, such as Ni, Au, Cd, and Ag.[196-199] Theoretically, there are still un-identified reaction pathways that are for C_1 and C_2 products. For example, recent study[185] shows that $*CHO \rightarrow *CHOH$ is the dominant pathway instead of $*CHO \rightarrow *CH_2O$ for CO_2 reduction to CH_4.

In Chapter 5, I investigated the CO_2/CO reduction mechanisms on four different Cu facets, Cu(211), Cu(110), Cu(100), and Cu(111). Among these four facets, Cu(110) facet is barely investigated by other computational groups because it is thermodynamically unstable due to its high free energy of Cu(110),[178] which is also supported my calculations of surface energies (Table 5.8). However, the predicted onset potentials on Cu(110) facet for CO_2(g)/CO(g) reduction to C_2 products agree well with the experimentally-observed overpotentials in the range of low potential (-0.2 – -0.5 V).[79, 82, 84, 157] My calculations demonstrate that Cu(110) facet may be responsible for low potentials and high selectivity of the ECR nanowires.[84-85]

In Chapter 5, I used the implicit solvation model developed by Mathew et al.[165-166] to mimic the liquid-solid phase of CO_2/CO reduction reaction on the surface of different Cu facets. For the same adsorbate, I found that the corrections attributed to the implicit solvation model on different facets are different (by an amount of about 10 – 20 meV). It

is worth building explicit solvation models by adding one or more layers of water layers[50, 91, 140, 164, 185] to the surface of different Cu facets to investigate solvation effects in the future.

Also, in Chapter 5, the kinetic effects have not been taken into account when I built the free energy diagrams and calculated the onset potentials. However, such kinetic effects may be important in determining the rate-limiting step for CO_2/CO reduction. To account for kinetic effects, nudged elastic band (NEB) method[89-90] could be used to determine the kinetic activation barriers for competing intermediate adsorbates (such as *CHO versus *COH) during the reduction pathway of CO_2/CO.[88, 187]

Moreover, there are still un-solved problems for pH and potential dependences on CO_2/CO reduction to C_1/C_2 products, which determine the possible pathways on different factes. For the competition between CHO-CHO coupling and CO-CO coupling mechanism in Chapter 5, CHO-CHO mechanism happens via the transfer of coupled electron-proton pair; while CO-CO mechanism happens via electron transfer first to form the negative charged $*OCCO^{\delta-}$ and proton transfer second (electron-proton transfers are decoupled). Thus, CO-CO coupling mechanism depends on the pH, but the CHO-CHO coupling mechanism does not. In Chapter 5, I did not calculate the free energy of the charged $*OCCO^{\delta-}$ intermediate due to the large variance (more than 1 eV) produced by different approaches.[91, 188] A new method recently proposed by Chan et al.[200-201], may be used to determine the free energy barrier for the intermediate step of $2*CO \rightarrow *OCCO^{\delta-}$ as a function of applied potential versus RHE. It will help us better understand the mechanisms of CO_2/CO reduction to C_2 products via CO-CO direct coupling if I can accurately and quantitatively differentiate the facets by the pH dependence and applied potential, which may aid rational synthesis of tailored Cu and Cu alloy catalysts for CO_2/CO reduction.

Bibliography

[1] Sanchez, J. M.; Ducastelle, F.; Gratias, D., Generalized Cluster Description of Multicomponent Systems. *Phys. A (Amsterdam, Neth.)* **1984**, *128*, 334-350.

[2] Ising, E., Beitrag zur Theorie des Ferromagnetismus. *Zeitschrift für Physik* **1925**, *31*, 253-258.

[3] Ozoliņš, V.; Wolverton, C.; Zunger, A., Cu-Au, Ag-Au, Cu-Ag, and Ni-Au Intermetallics: First-Principles Study of Temperature-Composition Phase Diagrams and Structures. *Phys. Rev. B* **1998**, *57*, 6427-6443.

[4] Sluiter, M. H. F.; Watanabe, Y.; Fontaine, D. d.; Kawazoe, Y., First-Principles Calculation of the Pressure Dependence of Phase Equilibria in the Al-Li System. *Phys. Rev. B* **1996**, *53*, 6137-6151.

[5] Van der Ven, A.; Aydinol, M. K.; Ceder, G.; Kresse, G.; Hafner, J., First-Principles Investigation of Phase Stability in Li_xCoO_2. *Phys. Rev. B* **1998**, *58*, 2975-2987.

[6] Zarkevich, N. A.; Tan, T. L.; Johnson, D. D., First-Principles Prediction of Phase-

Segregating Alloy Phase Diagrams and a Rapid Design Estimate of Their Transition Temperatures. *Phys. Rev. B* **2007**, *75*, 104203.

[7] Burton, B. P., Empirical Cluster Expansion Models of Cation Order-Disorder in $A(B'_{1/3},B''_{2/3})O_3$ Perovskites. *Phys. Rev. B* **1999**, *59*, 6087-6091.

[8] Wolverton, C.; Zunger, A., Prediction of Li Intercalation and Battery Voltages in Layered vs. Cubic Li_xCoO_2. *J. Electrochem. Soc.* **1998**, *145*, 2424-2431.

[9] Seko, A.; Yuge, K.; Oba, F.; Kuwabara, A.; Tanaka, I., Prediction of Ground-State Structures and Order-Disorder Phase Transitions in II-III Spinel Oxides: A Combined Cluster-Expansion Method and First-Principles Study. *Phys. Rev. B* **2006**, *73*, 184117/1-184117/5.

[10] Kolb, B.; Hart, G. L. W., Nonmetal Ordering in $TiC_{1-x}N_x$: Ground-State Structure and the Effects of Finite Temperature. *Phys. Rev. B* **2005**, *72*, 224207/1-224207/7.

[11] Franceschetti, A.; Zunger, A., The Inverse Band-Structure Problem of Finding An Atomic Configuration with Given Electronic Properties. *Nature* **1999**, *402*, 60-63.

[12] van de Walle, A., A Complete Representation of Structure-Property Relationships in Crystals. *Nat. Mater.* **2008**, *7*, 455-458.

[13] Mueller, T.; Ceder, G., Effective Interactions between the N-H Bond Orientations in Lithium Imide and a Proposed Ground-State Structure. *Phys. Rev. B* **2006**, *74*, 134104/1-134104/7.

[14] Kohn, W.; Sham, L. J., Self-Consistent Equations Including Exchange and Correlation Effects. *Phys. Rev.* **1965**, *140*, A1133-A1138.

[15] Kresse, G.; Furthmueller, J., Efficient Iterative Schemes for Ab initio Total-Energy

Calculations Using a Plane-Wave Basis Set. *Phys. Rev. B* **1996**, *54*, 11169-11186.

[16] Kresse, G.; Furthmuller, J., Efficiency of Ab-initio Total Energy Calculations for Metals and Semiconductors Using a Plane-Wave Basis Set. *Comput. Mater. Sci.* **1996**, *6*, 15-50.

[17] Zunger, A.; Wei, S. H.; Ferreira, L. G.; Bernard, J. E., Special Quasirandom Structures. *Phys. Rev. Lett.* **1990**, *65*, 353-356.

[18] Van de Walle, A.; Ceder, G., Automating First-Principles Phase Diagram Calculations. *J. Phase Equilib.* **2002**, *23*, 348-359.

[19] Seko, A.; Koyama, Y.; Tanaka, I., Cluster Expansion Method for Multicomponent Systems Based on Optimal Selection of Structures for Density-Functional Theory Calculations. *Phys. Rev. B* **2009**, *80*, 165122/1-165122/7.

[20] Mueller, T.; Ceder, G., Exact Expressions for Structure Selection in Cluster Expansions. *Phys. Rev. B* **2010**, *82*, 184107/1-184107/6.

[21] Mueller, T.; Ceder, G., Bayesian Approach to Cluster Expansions. *Phys. Rev. B* **2009**, *80*, 024103/1-024103/13.

[22] Mueller, T.; Ceder, G., *Ab initio* Study of the Low-Temperature Phases of Lithium Imide. *Phys. Rev. B* **2010**, *82*, 174307/1-174307/7.

[23] Sadigh, B.; Asta, M.; Ozoliņš, V.; Schmid, A. K.; Bartelt, N. C.; Quong, A. A.; Hwang, R. Q., Short-Range Order and Phase Stability of Surface Alloys: PdAu on Ru(0001). *Phys. Rev. Lett.* **1999**, *83*, 1379-1382.

[24] Wieckhorst, O.; Müller, S.; Hammer, L.; Heinz, K., First-Principles-Based Surface Phase Diagram of Fully Relaxed Binary Alloy Surfaces. *Phys. Rev. Lett.* **2004**, *92*,

195503/1-195503/4.

[25] Han, B. C.; Van der Ven, A.; Ceder, G.; Hwang, B.-J., Surface Segregation and Ordering of Alloy Surfaces in the Presence of Adsorbates. *Phys. Rev. B* **2005**, *72*, 205409/1-205409/9.

[26] Mueller, T.; Ceder, G., Effect of Particle Size on Hydrogen Release from Sodium Alanate Nanoparticles. *ACS Nano* **2010**, *4*, 5647-5656.

[27] Tan, T. L.; Wang, L.-L.; Johnson, D. D.; Bai, K., A Comprehensive Search for Stable Pt-Pd Nanoalloy Configurations and Their Use as Tunable Catalysts. *Nano Lett.* **2012**, *12*, 4875-4880.

[28] Yuge, K., First-Principles-based Optimization of Electronic Structures for Bimetallic Nanoparticles. *CALPHAD: Comput. Coupling Phase Diagrams Thermochem.* **2014**, *47*, 144-147.

[29] Litster, S.; McLean, G., PEM Fuel Cell Electrodes. *J. Power Sources* **2004**, *130*, 61-76.

[30] Antolini, E., Formation of Carbon-Supported PtM Alloys for Low Temperature Fuel Cells: A Review. *Materials Chemistry and Physics* **2003**, *78*, 563-573.

[31] Shao, M.; Chang, Q.; Dodelet, J.-P.; Chenitz, R., Recent Advances in Electrocatalysts for Oxygen Reduction Reaction. *Chem. Rev.* **2016**, *116*, 3594-3657.

[32] Chen, J.; Lim, B.; Lee, E. P.; Xia, Y., Shape-Controlled Synthesis of Platinum Nanocrystals for Catalytic and Electrocatalytic Applications. *Nano Today* **2009**, *4*, 81-95.

[33] Wu, J.; Yang, H., Platinum-Based Oxygen Reduction Electrocatalysts. *Acc. Chem.*

Res. **2013**, *46*, 1848-1857.

[34] Campbell, C. T.; Ertl, G.; Kuipers, H.; Segner, J., A Molecular Beam Study of the Adsorption and Desorption of Oxygen from a Platinum(111) Surface. *Surf. Sci.* **1981**, *107*, 220-236.

[35] Wang, C.; Daimon, H.; Onodera, T.; Koda, T.; Sun, S., A General Approach to the Size- and Shape-Controlled Synthesis of Platinum Nanoparticles and Their Catalytic Reduction of Oxygen. *Angew. Chem., Int. Ed.* **2008**, *47*, 3588-3591.

[36] Zhang, J.; Zhang, H.; Wu, J.; Zhang, J., Chapter 3 - Techniques for PEM Fuel Cell Testing and Diagnosis. In *Pem Fuel Cell Testing and Diagnosis*, Elsevier: Amsterdam, 2013; pp 81-119.

[37] Wang, H.; Yuan, X.-Z.; Li, H., *PEM Fuel Cell Diagnostic Tools*; CRC Press, 2011.

[38] Stamenkovic, V. R.; Mun, B. S.; Mayrhofer, K. J. J.; Ross, P. N.; Markovic, N. M., Effect of Surface Composition on Electronic Structure, Stability, and Electrocatalytic Properties of Pt-Transition Metal Alloys: Pt-Skin versus Pt-Skeleton Surfaces. *J. Am. Chem. Soc.* **2006**, *128*, 8813-8819.

[39] Venarusso, L. B.; Sato, R. H.; Fiorito, P. A.; Maia, G., Platinum Systems Electrodeposited in the Presence of Iron or Palladium on a Gold Surface Effectively Catalyze Oxygen Reduction Reaction. *J. Phys. Chem. C* **2013**, *117*, 7540-7551.

[40] Zhang, S.; Zhang, X.; Jiang, G.; Zhu, H.; Guo, S.; Su, D.; Lu, G.; Sun, S., Tuning Nanoparticle Structure and Surface Strain for Catalysis Optimization. *J. Am. Chem. Soc.* **2014**, *136*, 7734-7739.

[41] Jayasayee, K.; Veen, J. A. R. V.; Manivasagam, T. G.; Celebi, S.; Hensen, E. J. M.; de

Bruijn, F. A., Oxygen Reduction Reaction (ORR) Activity and Durability of Carbon Supported PtM (Co, Ni, Cu) Alloys: Influence of Particle Size and Non-Noble Metals. *Appl. Catal., B* **2012**, *111–112*, 515-526.

[42] Kakade, B. A.; Wang, H.; Tamaki, T.; Ohashi, H.; Yamaguchi, T., Enhanced Oxygen Reduction Eeaction by Bimetallic CoPt and PdPt Nanocrystals. *RSC Adv.* **2013**, *3*, 10487-10496.

[43] Fowler, B.; Lucas, C. A.; Omer, A.; Wang, G.; Stamenkovic, V. R.; Markovic, N. M., Segregation and Stability at $Pt_3Ni(111)$ Surfaces and $Pt_{75}Ni_{25}$ Nanoparticles. *Electrochim. Acta* **2008**, *53*, 6076-6080.

[44] Jeon, T.-Y.; Yoo, S. J.; Cho, Y.-H.; Lee, K.-S.; Kang, S. H.; Sung, Y.-E., Influence of Oxide on the Oxygen Reduction Reaction of Carbon-Supported Pt−Ni Alloy Nanoparticles. *J. Phys. Chem. C* **2009**, *113*, 19732-19739.

[45] Gland, J. L.; Sexton, B. A.; Fisher, G. B., Oxygen Interactions with the Platinum (111) Surface. *Surf. Sci.* **1980**, *95*, 587-602.

[46] Jacob, T.; Merinov, B. V.; Goddard, W. A., Chemisorption of Atomic Oxygen on Pt(1 1 1) and Pt/Ni(1 1 1) Surfaces. *Chem. Phys. Lett.* **2004**, *385*, 374-377.

[47] Jacob, T.; Goddard, W. A., III, Adsorption of Atomic H and O on the (111) Surface of Pt_3Ni Alloys. *J. Phys. Chem. B* **2004**, *108*, 8311-8323.

[48] Stamenkovic, V.; Mun, B. S.; Mayrhofer, K. J. J.; Ross, P. N.; Markovic, N. M.; Rossmeisl, J.; Greeley, J.; Norskov, J. K., Changing the Activity of Electrocatalysts for Oxygen Reduction by Tuning the Surface Electronic Structure. *Angew. Chem., Int. Ed.* **2006**, *45*, 2897-2901.

[49] Greeley, J.; Stephens, I. E. L.; Bondarenko, A. S.; Johansson, T. P.; Hansen, H. A.; Jaramillo, T. F.; Rossmeisl, J.; Chorkendorff, I.; Norskov, J. K., Alloys of Platinum and Early Transition Metals as Oxygen Reduction Electrocatalysts. *Nat. Chem.* **2009**, *1*, 552-556.

[50] Matanovic, I.; Garzon, F. H.; Henson, N. J., Theoretical Study of Electrochemical Processes on Pt-Ni Alloys. *J. Phys. Chem. C* **2011**, *115*, 10640-10650.

[51] Hyman, M. P.; Medlin, J. W., Effects of Electronic Structure Modifications on the Adsorption of Oxygen Reduction Reaction Intermediates on Model Pt(111)-Alloy Surfaces. *J. Phys. Chem. C* **2007**, *111*, 17052-17060.

[52] Gasteiger, H. A.; Kocha, S. S.; Sompalli, B.; Wagner, F. T., Activity Benchmarks and Requirements for Pt, Pt-Alloy, and non-Pt Oxygen Reduction Catalysts for PEMFCs. *Appl. Catal., B* **2005**, *56*, 9-35.

[53] Stamenkovic, V. R.; Fowler, B.; Mun, B. S.; Wang, G.; Ross, P. N.; Lucas, C. A.; Markovic, N. M., Improved Oxygen Reduction Activity on $Pt_3Ni(111)$ via Increased Surface Site Availability. *Science* **2007**, *315*, 493-497.

[54] Huang, X.; Zhao, Z.; Cao, L.; Chen, Y.; Zhu, E.; Lin, Z.; Li, M.; Yan, A.; Zettl, A.; Wang, Y. M., et al., High-Performance Transition Metal-doped Pt_3Ni Octahedra for Oxygen Reduction Reaction. *Science* **2015**, *348*, 1230-1234.

[55] Norskov, J. K.; Rossmeisl, J.; Logadottir, A.; Lindqvist, L.; Kitchin, J. R.; Bligaard, T.; Jonsson, H., Origin of the Overpotential for Oxygen Reduction at a Fuel-Cell Cathode. *J. Phys. Chem. B* **2004**, *108*, 17886-17892.

[56] Karlberg, G. S.; Rossmeisl, J.; Norskov, J. K., Estimations of Electric Field Effects on

the Oxygen Reduction Reaction based on the Density Functional Theory. *Phys. Chem. Chem. Phys.* **2007**, *9*, 5158-5161.

[57] Rossmeisl, J.; Karlberg, G. S.; Jaramillo, T.; Norskov, J. K., Steady State Oxygen Reduction and Cyclic Voltammetry. *Faraday Discuss.* **2008**, *140*, 337-346.

[58] Chen, C.; Kang, Y.; Huo, Z.; Zhu, Z.; Huang, W.; Xin, H. L.; Snyder, J. D.; Li, D.; Herron, J. A.; Mavrikakis, M., et al., Highly Crystalline Multimetallic Nanoframes with Three-Dimensional Electrocatalytic Surfaces. *Science* **2014**, *343*, 1339-1343.

[59] Cui, C.; Gan, L.; Heggen, M.; Rudi, S.; Strasser, P., Compositional Segregation in Shaped Pt Alloy Nanoparticles and Their Structural Behaviour during Electrocatalysis. *Nat. Mater.* **2013**, *12*, 765-771.

[60] Beermann, V.; Gocyla, M.; Willinger, E.; Rudi, S.; Heggen, M.; Dunin-Borkowski, R. E.; Willinger, M.-G.; Strasser, P., Rh-Doped Pt–Ni Octahedral Nanoparticles: Understanding the Correlation between Elemental Distribution, Oxygen Reduction Reaction, and Shape Stability. *Nano Lett.* **2016**, *16*, 1719-1725.

[61] Wang, C.; Chi, M.-F.; Li, D.-G.; Strmcnik, D.; van der Vliet, D.; Wang, G.-F.; Komanicky, V.; Chang, K.-C.; Paulikas, A. P.; Tripkovic, D., et al., Design and Synthesis of Bimetallic Electrocatalyst with Multilayered Pt-Skin Surfaces. *J. Am. Chem. Soc.* **2011**, *133*, 14396-14403.

[62] Zhang, L.; Roling, L. T.; Wang, X.; Vara, M.; Chi, M.; Liu, J.; Choi, S.-I.; Park, J.; Herron, J. A.; Xie, Z., et al., Platinum-Based Nanocages with Subnanometer-Thick Walls and Well-Defined, Controllable Facets. *Science* **2015**, *349*, 412-416.

[63] Cui, C.; Gan, L.; Li, H.-H.; Yu, S.-H.; Heggen, M.; Strasser, P., Octahedral PtNi

Nanoparticle Catalysts: Exceptional Oxygen Reduction Activity by Tuning the Alloy Particle Surface Composition. *Nano Lett.* **2012**, *12*, 5885-5889.

[64] Snyder, J.; McCue, I.; Livi, K.; Erlebacher, J., Structure/Processing/Properties Relationships in Nanoporous Nanoparticles As Applied to Catalysis of the Cathodic Oxygen Reduction Reaction. *J. Am. Chem. Soc.* **2012**, *134*, 8633-8645.

[65] Wang, C.; Chi, M.; Wang, G.; van der Vliet, D.; Li, D.; More, K.; Wang, H.-H.; Schlueter, J. A.; Markovic, N. M.; Stamenkovic, V. R., Correlation between Surface Chemistry and Electrocatalytic Properties of Monodisperse Pt_xNi_{1-x} Nanoparticles. *Adv. Funct. Mater.* **2011**, *21*, 147-152.

[66] Sakamoto, R.; Omichi, K.; Furuta, T.; Ichikawa, M., Effect of High Oxygen Reduction Reaction Activity of Octahedral PtNi Nanoparticle Electrocatalysts on Proton Exchange Membrane Fuel Cell Performance. *J. Power Sources* **2014**, *269*, 117-123.

[67] Carpenter, M. K.; Moylan, T. E.; Kukreja, R. S.; Atwan, M. H.; Tessema, M. M., Solvothermal Synthesis of Platinum Alloy Nanoparticles for Oxygen Reduction Electrocatalysis. *J. Am. Chem. Soc.* **2012**, *134*, 8535-8542.

[68] Choi, S.-I.; Xie, S.; Shao, M.; Odell, J. H.; Lu, N.; Peng, H.-C.; Protsailo, L.; Guerrero, S.; Park, J.; Xia, X., et al., Synthesis and Characterization of 9 nm Pt–Ni Octahedra with a Record High Activity of 3.3 A/mgPt for the Oxygen Reduction Reaction. *Nano Lett.* **2013**, *13*, 3420-3425.

[69] Mueller, T., Ab initio Determination of Structure-Property Relationships in Alloy Nanoparticles. *Phys. Rev. B* **2012**, *86*, 144201/1-144201/5.

[70] Yuge, K., Segregation of $Pt_{28}Rh_{27}$ Bimetallic Nanoparticles: A First-Principles Study.

J. Phys.: Condens. Matter **2010**, *22*, 245401.

[71] Yuge, K., Concentration Effects on Segregation Behavior of Pt-Rh Nanoparticles. *Phys. Rev. B* **2011**, *84*, 085451.

[72] Wu, J.; Zhang, J.; Peng, Z.; Yang, S.; Wagner, F. T.; Yang, H., Truncated Octahedral Pt_3Ni Oxygen Reduction Reaction Electrocatalysts. *J. Am. Chem. Soc.* **2010**, *132*, 4984-4985.

[73] Chen, M.; Kumar, D.; Yi, C.-W.; Goodman, D. W., The Promotional Effect of Gold in Catalysis by Palladium-Gold. *Science* **2005**, *310*, 291-293.

[74] Olah, G. A.; Prakash, G. K. S.; Goeppert, A., Anthropogenic Chemical Carbon Cycle for a Sustainable Future. *J. Am. Chem. Soc.* **2011**, *133*, 12881-12898.

[75] Kuhl, K. P.; Cave, E. R.; Abram, D. N.; Jaramillo, T. F., New Insights into the Electrochemical Reduction of Carbon Dioxide on Metallic Copper Surfaces. *Energy Environ. Sci.* **2012**, *5*, 7050-7059.

[76] Hori, Y.; Wakebe, H.; Tsukamoto, T.; Koga, O., Electrocatalytic Process of CO Selectivity in Electrochemical Reduction of CO_2 at Metal Electrodes in Aqueous Media. *Electrochim. Acta* **1994**, *39*, 1833-1839.

[77] Hori, Y.; Murata, A.; Takahashi, R., Formation of Hydrocarbons in the Electrochemical Reduction of Carbon Dioxide at A Copper Electrode in Aqueous Solution. *J. Chem. Soc., Faraday Trans. 1* **1989**, *85*, 2309-2326.

[78] Gattrell, M.; Gupta, N.; Co, A., A Review of the Aqueous Electrochemical Reduction of CO_2 to Hydrocarbons at Copper. *J. Electroanal. Chem.* **2006**, *594*, 1-19.

[79] Li, C. W.; Ciston, J.; Kanan, M. W., Electroreduction of Carbon Monoxide to Liquid

Fuel on Oxide-Derived Nanocrystalline Copper. *Nature* **2014**, *508*, 504-507.

[80] Li, C. W.; Kanan, M. W., CO_2 Reduction at Low Overpotential on Cu Electrodes Resulting from the Reduction of Thick Cu_2O Films. *J. Am. Chem. Soc.* **2012**, *134*, 7231-7234.

[81] Hori, Y.; Takahashi, I.; Koga, O.; Hoshi, N., Selective Formation of C_2 Compounds from Electrochemical Reduction of CO_2 at a Series of Copper Single Crystal Electrodes. *J. Phys. Chem. B* **2002**, *106*, 15-17.

[82] Schouten, K. J. P.; Qin, Z.; Gallent, E. P.; Koper, M. T. M., Two Pathways for the Formation of Ethylene in CO Reduction on Single-Crystal Copper Electrodes. *J. Am. Chem. Soc.* **2012**, *134*, 9864-9867.

[83] Reske, R.; Mistry, H.; Behafarid, F.; Roldan Cuenya, B.; Strasser, P., Particle Size Effects in the Catalytic Electroreduction of CO_2 on Cu Nanoparticles. *J. Am. Chem. Soc.* **2014**, *136*, 6978-6986.

[84] Raciti, D.; Livi, K. J.; Wang, C., Highly Dense Cu Nanowires for Low-Overpotential CO2 Reduction. *Nano Lett.* **2015**, *15*, 6829-6835.

[85] Raciti, D.; Li, C.; Cao, L.; Rottmann, P.; Livi, K.; Bowen, K.; Hemker, K.; Mueller, T.; Wang, C., Tailoring Cu Nanowires for Electrochemical CO Reduction. *Submitted* **2016**.

[86] Calle-Vallejo, F.; Koper, M. T. M., Theoretical Considerations on the Electroreduction of CO to C2 Species on Cu(100) Electrodes. *Angew. Chem., Int. Ed.* **2013**, *52*, 7282-7285.

[87] Schouten, K. J. P.; Pérez Gallent, E.; Koper, M. T. M., Structure Sensitivity of the

Electrochemical Reduction of Carbon Monoxide on Copper Single Crystals. *ACS Catal.* **2013**, *3*, 1292-1295.

[88] Montoya, J. H.; Peterson, A. A.; Nørskov, J. K., Insights into C–C Coupling in CO_2 Electroreduction on Copper Electrodes. *ChemCatChem* **2013**, *5*, 737-742.

[89] Henkelman, G.; Uberuaga, B. P.; Jónsson, H., A Climbing Image Nudged Elastic Band Method for Finding Saddle Points and Minimum Energy Paths. *J. Chem. Phys.* **2000**, *113*, 9901-9904.

[90] Henkelman, G.; Jónsson, H., Improved Tangent Estimate in the Nudged Elastic Band Method for Finding Minimum Energy Paths and Saddle Points. *J. Chem. Phys.* **2000**, *113*, 9978-9985.

[91] Montoya, J. H.; Shi, C.; Chan, K.; Nørskov, J. K., Theoretical Insights into a CO Dimerization Mechanism in CO_2 Electroreduction. *J. Phys. Chem. Lett.* **2015**, *6*, 2032-2037.

[92] Cao, L.; Mueller, T., Rational Design of Pt_3Ni Surface Structures for the Oxygen Reduction Reaction. *J. Phys. Chem. C* **2015**, *119*, 17735-17747.

[93] Cao, L.; Mueller, T., Theoretical Insights into the Effects of Oxidation and Mo-Doping on the Structure and Stability of Pt-Ni Nanoparticles *Submitted* **2016**.

[94] Sakurai, J. J., *Modern Quantum Mechanics (Revised Edition)*; Addison Wesley, 1993.

[95] Atkins, P. W., *Molecular Quantum Mechanics Parts I and II: An Introduction to QUANTUM CHEMISTRY (Volume 1)*; Oxford University Press, 1977.

[96] Sholl, D.; Steckel, J. A., *Density functional theory: a practical introduction*; John Wiley & Sons, 2011.

[97] Hohenberg, P.; Kohn, W., Inhomogeneous Electron Gas. *Phys. Rev.* **1964**, *136*, B864-B871.

[98] Kresse, G.; Hafner, J., Ab initio Molecular Dynamics of Liquid Metals. *Phys. Rev. B* **1993**, *47*, 558-561.

[99] Kresse, G.; Hafner, J., Ab initio Molecular Dynamics for Open-Shell Transition Metals. *Phys. Rev. B* **1993**, *48*, 13115-13118.

[100] Kresse, G.; Hafner, J., Ab initio Molecular-Dynamics Simulation of the Liquid-Metal-Amorphous-Semiconductor Transition in Germanium. *Phys. Rev. B* **1994**, *49*, 14251-14269.

[101] Blöchl, P. E., Projector Augmented-Wave Method. *Phys. Rev. B* **1994**, *50*, 17953-17979.

[102] Perdew, J. P.; Burke, K.; Ernzerhof, M., Generalized Gradient Approximation Made Simple. *Phys. Rev. Lett.* **1996**, *77*, 3865-3868.

[103] Zhang, Y.; Yang, W., Comment on "Generalized Gradient Approximation Made Simple". *Phys. Rev. Lett.* **1998**, *80*, 890.

[104] Methfessel, M.; Paxton, A. T., High-Precision Sampling for Brillouin-Zone Integration in Metals. *Phys. Rev. B* **1989**, *40*, 3616-3621.

[105] Kikuchi, R., A Theory of Cooperative Phenomena. *Phys. Rev.* **1951**, *81*, 988-1003.

[106] Denison, D.; Holmes, C.; Mallick, B.; Smith, A., *Bayesian Methods for Nonlinear Classification and Regression*; John Wiley & Sons: Chichester, UK, 2002.

[107] Garbulsky, G. D.; Ceder, G., Linear-Programming Method for Obtaining Effective Cluster Interactions in Alloys from Total-Energy Calculations: Application to the fcc

Pd-V System. *Phys. Rev. B* **1995**, *51*, 67-72.

[108] Mueller, T. Computational Studies of Hydrogen Storage Materials and the Development of Related Methods. Massachusetts Institute of Technology, Boston, MA, 2007.

[109] Metropolis, N.; Rosenbluth, A. W.; Rosenbluth, M. N.; Teller, A. H.; Teller, E., Equation of State Calculations by Fast Computing Machines. *J. Chem. Phys.* **1953**, *21*, 1087-1092.

[110] Frenkel, D.; Smit, B., *Understanding Molecular Simulation: from Algorithms to Applications*; Academic press, 2001; Vol. 1.

[111] Perdew, J. P.; Chevary, J. A.; Vosko, S. H.; Jackson, K. A.; Pederson, M. R.; Singh, D. J.; Fiolhais, C., Atoms, Molecules, Solids, and Surfaces: Applications of the Generalized Gradient Approximation for Exchange and Correlation. *Phys. Rev. B* **1992**, *46*, 6671-6687.

[112] Jones, R. O.; Gunnarsson, O., The Density Functional Formalism, its Applications and Prospects. *Rev. Mod. Phys.* **1989**, *61*, 689-746.

[113] Patton, D. C.; Porezag, D. V.; Pederson, M. R., Simplified Generalized-Gradient Approximation and Anharmonicity: Benchmark Calculations on Molecules. *Phys. Rev. B* **1997**, *55*, 7454-7459.

[114] Hammer, B.; Hansen, L. B.; Nørskov, J. K., Improved Adsorption Energetics within Density-Functional Theory using Revised Perdew-Burke-Ernzerhof Functionals. *Phys. Rev. B* **1999**, *59*, 7413-7421.

[115] Wang, L.; Maxisch, T.; Ceder, G., Oxidation Energies of Transition Metal Oxides

within the GGA+U Framework. *Phys. Rev. B* **2006**, *73*, 195107/1-195107/6.

[116] NIST-JANAF Thermochemical Tables (http://kinetics.nist.gov/janaf/). National Institute of Standards and Technology.

[117] Yeo, Y. Y.; Vattuone, L.; King, D. A., Calorimetric Heats for CO and Oxygen Adsorption and for the Catalytic CO Oxidation Reaction on Pt{111}. *J. Chem. Phys.* **1997**, *106*, 392-401.

[118] Stamenkovic, V. R.; Mun, B. S.; Arenz, M.; Mayrhofer, K. J. J.; Lucas, C. A.; Wang, G.; Ross, P. N.; Markovic, N. M., Trends in Electrocatalysis on Extended and Nanoscale Pt-Bimetallic Alloy Surfaces. *Nat. Mater.* **2007**, *6*, 241-247.

[119] Ma, Y.; Balbuena, P. B., Surface Properties and Dissolution Trends of Pt3M Alloys in the Presence of Adsorbates. *J. Phys. Chem. C* **2008**, *112*, 14520-14528.

[120] Ma, Y.; Balbuena, P. B., Pt Surface Segregation in Bimetallic Pt_3M Alloys: A Density Functional Theory Study. *Surf. Sci.* **2008**, *602*, 107-113.

[121] Sha, Y.; Yu, T. H.; Merinov, B. V.; Shirvanian, P.; Goddard, W. A., III, Mechanism for Oxygen Reduction Reaction on Pt3Ni Alloy Fuel Cell Cathode. *J. Phys. Chem. C* **2012**, *116*, 21334-21342.

[122] Yang, Z.; Wang, J.; Yu, X., The Adsorption, Diffusion and Dissociation of O_2 on Pt-skin Pt_3Ni(1 1 1): A Density Functional Theory Study. *Chem. Phys. Lett.* **2010**, *499*, 83-88.

[123] Anderson, A. B.; Jinnouchi, R.; Uddin, J., Effective Reversible Potentials and Onset Potentials for O2 Electroreduction on Transition Metal Electrodes: Theoretical Analysis. *J. Phys. Chem. C* **2013**, *117*, 41-48.

[124] Xu, W.; Cheng, D.; Niu, M.; Shao, X.; Wang, W., Modification of the Adsorption Properties of O and OH on Pt-Ni Bimetallic Surfaces by Subsurface Alloying. *Electrochim. Acta* **2012**, *76*, 440-445.

[125] Su, H.-Y.; Bao, X.-H.; Li, W.-X., Modulating the Reactivity of Ni-Containing Pt(111)-skin Catalysts by Density Functional Theory Calculations. *J. Chem. Phys.* **2008**, *128*, 194707/1-194707/7.

[126] Greeley, J.; Norskov, J. K., A General Scheme for the Estimation of Oxygen Binding Energies on Binary Transition Metal Surface Alloys. *Surf. Sci.* **2005**, *592*, 104-111.

[127] Kitchin, J. R.; Norskov, J. K.; Barteau, M. A.; Chen, J. G., Modification of the Surface Electronic and Chemical Properties of Pt(111) by Subsurface 3d Transition Metals. *J. Chem. Phys.* **2004**, *120*, 10240-10246.

[128] Anniyev, T.; Kaya, S.; Rajasekaran, S.; Ogasawara, H.; Nordlund, D.; Nilsson, A., Tuning the Metal–Adsorbate Chemical Bond through the Ligand Effect on Platinum Subsurface Alloys. *Angew. Chem., Int. Ed.* **2012**, *51*, 7724-7728.

[129] Duan, Z.; Wang, G., A First Principles Study of Oxygen Reduction Reaction on a Pt(111) Surface Modified by a Subsurface Transition Metal M (M = Ni, Co, or Fe). *Phys. Chem. Chem. Phys.* **2011**, *13*, 20178-20187.

[130] Monkhorst, H. J.; Pack, J. D., Special Points for Brillouin-Zone Integrations. *Phys. Rev. B* **1976**, *13*, 5188-5192.

[131] Momma, K.; Izumi, F., VESTA: A Three-Dimensional Visualization System for Electronic and Structural Analysis. *J. Appl. Crystallogr.* **2008**, *41*, 653-658.

[132] Kitchin, J. R.; Miller, S. D.; Sholl, D. S., Density functional theory studies of alloys in

heterogeneous catalysis. *Chem. Modell.* **2008**, *5*, 150-181.

[133] Landau, D.; Binder, K., *A Guide to Monte Carlo Simulations in Statistical Physics*; Cambridge University Press, 2005.

[134] Dahmani, C. E.; Cadeville, M. C.; Pierron-Bohnes, V., Temperature Dependences of Atomic Order Relaxations in Nickel-Platinum and Cobalt-Platinum Alloys. *Acta Metall.* **1985**, *33*, 369-377.

[135] Dahmani, C. E.; Cadeville, M. C.; Sanchez, J. M.; Moran-Lopez, J. L., Nickel-Platinum Phase Diagram: Experiment and Theory. *Phys. Rev. Lett.* **1985**, *55*, 1208-1211.

[136] Cadeville, M. C.; Dahmani, C. E.; Kern, F., Magnetism and Spatial Order in Nickel-Platinum and Cobalt-Platinum Alloys. *J. Magn. Magn. Mater.* **1986**, *54-57*, 1055-1056.

[137] Stamenkovic, V.; Schmidt, T. J.; Ross, P. N.; Markovic, N. M., Surface Composition Effects in Electrocatalysis: Kinetics of Oxygen Reduction on Well-Defined Pt3Ni and Pt3Co Alloy Surfaces. *J. Phys. Chem. B* **2002**, *106*, 11970-11979.

[138] Grossmann, A.; Erley, W.; Ibach, H., Adsorbate-Induced Surface Stress and Surface Reconstruction: Oxygen, Sulfur and Carbon on Ni(111). *Surf. Sci.* **1995**, *337*, 183-189.

[139] Abild-Pedersen, F.; Greeley, J.; Studt, F.; Rossmeisl, J.; Munter, T. R.; Moses, P. G.; Skúlason, E.; Bligaard, T.; Nørskov, J. K., Scaling Properties of Adsorption Energies for Hydrogen-Containing Molecules on Transition-Metal Surfaces. *Phys. Rev. Lett.* **2007**, *99*, 016105.

[140] Rossmeisl, J.; Logadottir, A.; Norskov, J. K., Electrolysis of Water on (Oxidized) Metal

Surfaces. *Chem. Phys.* **2005**, *319*, 178-184.

[141] Gan, L.; Cui, C.; Heggen, M.; Dionigi, F.; Rudi, S.; Strasser, P., Element-Specific Anisotropic Growth of Shaped Platinum Alloy Nanocrystals. *Science* **2014**, *346*, 1502-1506.

[142] Hautier, G.; Jain, A.; Ong, S. P., From the Computer to the Laboratory: Materials Discovery and Design using First-Principles Calculations. *J. Mater. Sci.* **2012**, *47*, 7317-7340.

[143] Wei, S.; Chou, M. Y., First-Principles Determination of Equilibrium Crystal Shapes for Metals at T=0. *Phys. Rev. B* **1994**, *50*, 4859-4862.

[144] Chepulskii, R. V.; Butler, W. H., Temperature and Particle-Size Dependence of the Equilibrium Order Parameter of FePt Alloys. *Phys. Rev. B* **2005**, *72*, 134205/1-134205/18.

[145] Guo, S.; Li, D.; Zhu, H.; Zhang, S.; Markovic, N. M.; Stamenkovic, V. R.; Sun, S., FePt and CoPt Nanowires as Efficient Catalysts for the Oxygen Reduction Reaction. *Angew. Chem., Int. Ed.* **2013**, *52*, 3465-3468.

[146] Kang, Y.; Snyder, J.; Chi, M.; Li, D.; More, K. L.; Markovic, N. M.; Stamenkovic, V. R., Multimetallic Core/Interlayer/Shell Nanostructures as Advanced Electrocatalysts. *Nano Lett.* **2014**, *14*, 6361-6367.

[147] van der Vliet, D. F.; Wang, C.; Tripkovic, D.; Strmcnik, D.; Zhang, X. F.; Debe, M. K.; Atanasoski, R. T.; Markovic, N. M.; Stamenkovic, V. R., Mesostructured Thin Films as Electrocatalysts with Tunable Composition and Surface Morphology. *Nat. Mater.* **2012**, *11*, 1051-1058.

[148] Liu, Z.; Hu, J. E.; Wang, Q.; Gaskell, K.; Frenkel, A. I.; Jackson, G. S.; Eichhorn, B., PtMo Alloy and MoO_x@Pt Core−Shell Nanoparticles as Highly CO-Tolerant Electrocatalysts. *J. Am. Chem. Soc.* **2009**, *131*, 6924-6925.

[149] *CRC Handbook of Chemistry and Physics*, 81st ed.; CRC Press: Boca Raton, FL, 2000, p 2556.

[150] Atkins, P. W., *Physical Chemistry*, 6 ed.; Oxford Univ. Press: Oxford, 1998.

[151] Kandoi, S.; Gokhale, A. A.; Grabow, L. C.; Dumesic, J. A.; Mavrikakis, M., Why Au and Cu Are More Selective Than Pt for Preferential Oxidation of CO at Low Temperature. *Catal. Lett.* **2004**, *93*, 93-100.

[152] Shao, M.; Peles, A.; Shoemaker, K., Electrocatalysis on Platinum Nanoparticles: Particle Size Effect on Oxygen Reduction Reaction Activity. *Nano Lett.* **2011**, *11*, 3714-3719.

[153] Praserthdam, S.; Balbuena, P. B., Effects of Oxygen Coverage, Catalyst Size, and Core Composition on Pt-Alloy Core-Shell Nanoparticles for Oxygen Reduction Reaction. *Catal. Sci. Technol.* **2016**, *6*, 5168-5177.

[154] Gan, L.; Rudi, S.; Cui, C.; Heggen, M.; Strasser, P., Size-Controlled Synthesis of Sub-10 nm $PtNi_3$ Alloy Nanoparticles and their Unusual Volcano-Shaped Size Effect on ORR Electrocatalysis. *Small* **2016**, *12*, 3189-3196.

[155] Leroux, C.; Cadeville, M. C.; Pierron-Bohnes, V.; Inden, G.; Hinz, F., Comparative Investigation of Structural and Transport Properties of $L1_0$ NiPt and CoPt Phases; the Role of Magnetism. *J. Phys. F: Met. Phys.* **1988**, *18*, 2033-2051.

[156] Sanati, M.; Wang, L. G.; Zunger, A., Adaptive Crystal Structures: CuAu and NiPt.

Phys. Rev. Lett. **2003**, *90*, 045502/1-045502/4.

[157] Verdaguer-Casadevall, A.; Li, C. W.; Johansson, T. P.; Scott, S. B.; McKeown, J. T.; Kumar, M.; Stephens, I. E. L.; Kanan, M. W.; Chorkendorff, I., Probing the Active Surface Sites for CO Reduction on Oxide-Derived Copper Electrocatalysts. *J. Am. Chem. Soc.* **2015**, *137*, 9808-9811.

[158] Feng, X.; Jiang, K.; Fan, S.; Kanan, M. W., A Direct Grain-Boundary-Activity Correlation for CO Electroreduction on Cu Nanoparticles. *ACS Cent. Sci.* **2016**, *2*, 169-174.

[159] Hori, Y.; Takahashi, I.; Koga, O.; Hoshi, N., Electrochemical Reduction of Carbon Dioxide at Various Series of Copper Single Crystal Electrodes. *J. Mol. Catal. A: Chem.* **2003**, *199*, 39-47.

[160] Grimme, S.; Antony, J.; Ehrlich, S.; Krieg, H., A Consistent and Accurate ab initio Parametrization of Density Functional Dispersion Correction (DFT-D) for the 94 Elements H-Pu. *J. Chem. Phys.* **2010**, *132*, 154104/1-154104/19.

[161] Sakong, S.; Groß, A., The Importance of the Electrochemical Environment in the Electro-Oxidation of Methanol on Pt(111). *ACS Catal.* **2016**, *6*, 5575-5586.

[162] Reckien, W.; Eggers, M.; Bredow, T., Theoretical Study of the Adsorption of Benzene on Coinage Metals. *Beilstein J. Org. Chem.* **2014**, *10*, 1775-1784.

[163] Sakong, S.; Naderian, M.; Mathew, K.; Hennig, R. G.; Groß, A., Density Functional Theory Study of the Electrochemical Interface between a Pt Electrode and an Aqueous Electrolyte using an Implicit Solvent Method. *J. Chem. Phys.* **2015**, *142*, 234107/1-234107/12.

[164] Tonigold, K.; Groß, A., Dispersive Interactions in Water Bilayers at Metallic Surfaces: A Comparison of the PBE and RPBE Functional including Semiempirical Dispersion Corrections. *J. Comput. Chem.* **2012**, *33*, 695-701.

[165] Mathew, K.; Sundararaman, R.; Letchworth-Weaver, K.; Arias, T. A.; Hennig, R. G., Implicit Solvation Model for Density-Functional Study of Nanocrystal Surfaces and Reaction Pathways. *J. Chem. Phys.* **2014**, *140*, 084106/1-084106/8.

[166] Mathew, K.; Hennig, R. G., Implicit Self-Consistent Description of Electrolyte in Plane-Wave Density-Functional Theory. *arXiv* **2016**, arXiv:1601.03346.

[167] Wisesa, P.; McGill, K. A.; Mueller, T., Efficient Generation of Generalized Monkhorst-Pack Grids through the Use of Informatics. *Phys. Rev. B* **2016**, *93*, 155109/1-155109/10.

[168] Peterson, A. A.; Abild-Pedersen, F.; Studt, F.; Rossmeisl, J.; Norskov, J. K., How Copper Catalyzes the Electroreduction of Carbon Dioxide into Hydrocarbon Fuels. *Energy Environ. Sci.* **2010**, *3*, 1311-1315.

[169] Blaylock, D. W.; Ogura, T.; Green, W. H.; Beran, G. J. O., Computational Investigation of Thermochemistry and Kinetics of Steam Methane Reforming on Ni(111) under Realistic Conditions. *J. Phys. Chem. C* **2009**, *113*, 4898-4908.

[170] Afeefy, H. Y.; Liebman, J. F.; Stein, S. E., Neutral Thermochemical Data. In *NIST Chemistry WebBook, NIST Standard Reference Database Number 69*, Linstrom, E. P. J.; Mallard, W. G., Eds. National Institute of Standards and Technology: Gaithersburg MD, USA, 2010.

[171] Klimeš, J.; Bowler, D. R.; Michaelides, A., Van der Waals Density Functionals

Applied to Solids. *Phys. Rev. B* **2011**, *83*, 195131/1-195131/3.

[172] Jiří, K.; David, R. B.; Angelos, M., Chemical Accuracy for the van der Waals Density Functional. *J. Phys.: Condens. Matter* **2010**, *22*, 022201.

[173] Román-Pérez, G.; Soler, J. M., Efficient Implementation of a van der Waals Density Functional: Application to Double-Wall Carbon Nanotubes. *Phys. Rev. Lett.* **2009**, *103*, 096102/1-096102/4.

[174] Droog, J. M. M.; Schlenter, B., Oxygen Electrosorption on Copper Single Crystal Electrodes in Sodium Hydroxide Solution. *J. Electroanal. Chem. Interfacial Electrochem.* **1980**, *112*, 387-390.

[175] Vollmer, S.; Witte, G.; Wöll, C., Determination of Site Specific Adsorption Energies of CO on Copper. *Catal. Lett.* **2001**, *77*, 97-101.

[176] Zhao, P.; He, Y.; Cao, D.-B.; Wen, X.; Xiang, H.; Li, Y.-W.; Wang, J.; Jiao, H., High Coverage Adsorption and Co-Adsorption of CO and H_2 on Ru(0001) from DFT and Thermodynamics. *Phys. Chem. Chem. Phys.* **2015**, *17*, 19446-19456.

[177] Schimka, L.; Harl, J.; Stroppa, A.; Grüneis, A.; Marsman, M.; Mittendorfer, F.; Kresse, G., Accurate Surface and Adsorption Energies from Many-Body Perturbation Theory. *Nat. Mater.* **2010**, *9*, 741-744.

[178] Tran, R.; Xu, Z.; Radhakrishnan, B.; Winston, D.; Sun, W.; Persson, K. A.; Ong, S. P., Surface energies of elemental crystals. *Scientific Data* **2016**, *3*, 160080.

[179] Perdew, J. P.; Ruzsinszky, A.; Csonka, G. I.; Vydrov, O. A.; Scuseria, G. E.; Constantin, L. A.; Zhou, X.; Burke, K., Restoring the Density-Gradient Expansion for Exchange in Solids and Surfaces. *Phys. Rev. Lett.* **2008**, *100*, 136406.

[180] Stroppa, A.; Kresse, G., The Shortcomings of Semi-Local and Hybrid Functionals: What We Can Learn From Surface Science Studies. *New Journal of Physics* **2008**, *10*, 063020.

[181] Fishman, M.; Zhuang, H. L.; Mathew, K.; Dirschka, W.; Hennig, R. G., Accuracy of Exchange-Correlation Functionals and Effect of Solvation on the Surface Energy of Copper. *Phys. Rev. B* **2013**, *87*, 245402/1-245402/7.

[182] Dudarev, S. L.; Botton, G. A.; Savrasov, S. Y.; Humphreys, C. J.; Sutton, A. P., Electron-Energy-Loss Spectra and the Structural Stability of Nickel Oxide: An LSDA+U Study. *Phys. Rev. B* **1998**, *57*, 1505-1509.

[183] Anisimov, V. I.; Zaanen, J.; Andersen, O. K., Band Theory and Mott Insulators: Hubbard *U* instead of Stoner *I*. *Phys. Rev. B* **1991**, *44*, 943-954.

[184] Mishra, A. K.; Roldan, A.; de Leeuw, N. H., CuO Surfaces and CO_2 Activation: A Dispersion-Corrected DFT+U Study. *J. Phys. Chem. C* **2016**, *120*, 2198-2214.

[185] Shi, C.; Chan, K.; Yoo, J. S.; Nørskov, J. K., Barriers of Electrochemical CO_2 Reduction on Transition Metals. *Org. Process Res. Dev.* **2016**, *20*, 1424-1430.

[186] Li, Y.; Chan, S. H.; Sun, Q., Heterogeneous Catalytic Conversion of CO_2: a Comprehensive Theoretical Review. *Nanoscale* **2015**, *7*, 8663-8683.

[187] Luo, W.; Nie, X.; Janik, M. J.; Asthagiri, A., Facet Dependence of CO_2 Reduction Paths on Cu Electrodes. *ACS Catal.* **2016**, *6*, 219-229.

[188] Xiao, H.; Cheng, T.; Goddard, W. A.; Sundararaman, R., Mechanistic Explanation of the pH Dependence and Onset Potentials for Hydrocarbon Products from Electrochemical Reduction of CO on Cu (111). *J. Am. Chem. Soc.* **2016**, *138*, 483-

486.

[189] Cheng, T.; Xiao, H.; Goddard, W. A., Free-Energy Barriers and Reaction Mechanisms for the Electrochemical Reduction of CO on the Cu(100) Surface, Including Multiple Layers of Explicit Solvent at pH 0. *J. Phys. Chem. Lett.* **2015**, *6*, 4767-4773.

[190] Durand, W. J.; Peterson, A. A.; Studt, F.; Abild-Pedersen, F.; Nørskov, J. K., Structure Effects on the Energetics of the Electrochemical Reduction of CO_2 by Copper Surfaces. *Surf. Sci.* **2011**, *605*, 1354-1359.

[191] Liu, W.; Savara, A.; Ren, X.; Ludwig, W.; Dostert, K.-H.; Schauermann, S.; Tkatchenko, A.; Freund, H.-J.; Scheffler, M., Toward Low-Temperature Dehydrogenation Catalysis: Isophorone Adsorbed on Pd(111). *J. Phys. Chem. Lett.* **2012**, *3*, 582-586.

[192] Liu, W.; Tkatchenko, A.; Scheffler, M., Modeling Adsorption and Reactions of Organic Molecules at Metal Surfaces. *Acc. Chem. Res.* **2014**, *47*, 3369-3377.

[193] Błoński, P.; López, N., On the Adsorption of Formaldehyde and Methanol on a Water-Covered Pt(111): a DFT-D Study. *J. Phys. Chem. C* **2012**, *116*, 15484-15492.

[194] Strasser, P.; Koh, S.; Anniyev, T.; Greeley, J.; More, K.; Yu, C.; Liu, Z.; Kaya, S.; Nordlund, D.; Ogasawara, H., et al., Lattice-Strain Control of the Activity in Dealloyed Core-Shell Fuel Cell Catalysts. *Nat. Chem.* **2010**, *2*, 454-460.

[195] Wang, X.; Figueroa-Cosme, L.; Yang, X.; Luo, M.; Liu, J.; Xie, Z.; Xia, Y., Pt-Based Icosahedral Nanocages: Using a Combination of {111} Facets, Twin Defects, and Ultrathin Walls to Greatly Enhance Their Activity toward Oxygen Reduction. *Nano Lett.* **2016**, *16*, 1467-1471.

[196] Christophe, J.; Doneux, T.; Buess-Herman, C., Electroreduction of Carbon Dioxide

on Copper-Based Electrodes: Activity of Copper Single Crystals and Copper–Gold Alloys. *Electrocatalysis* **2012**, *3*, 139-146.

[197] Hori, Y.; Murata, A.; Ito, S.-y.; Yoshinami, Y.; Koga, O., Nickel and Iron Modified Copper Electrode for Electroreduction of CO_2 by In-situ Electrodeposition. *Chem. Lett.* **1989**, *18*, 1567-1570.

[198] Hori, Y.; Murata, A.; Ito, S.-y., Enhanced Evolution of CO and Suppressed Formation of Hydrocarbons in Electroreduction of CO_2 at a Copper Electrode Modified with Cadmium. *Chem. Lett.* **1990**, *19*, 1231-1234.

[199] Ishimaru, S.; Shiratsuchi, R.; Nogami, G., Pulsed Electroreduction of CO_2 on Cu-Ag Alloy Electrodes. *J. Electrochem. Soc.* **2000**, *147*, 1864-1867.

[200] Chan, K.; Nørskov, J. K., Electrochemical Barriers Made Simple. *J. Phys. Chem. Lett.* **2015**, *6*, 2663-2668.

[201] Chan, K.; Nørskov, J. K., Potential Dependence of Electrochemical Barriers from ab Initio Calculations. *J. Phys. Chem. Lett.* **2016**, *7*, 1686-1690.

Vita

Liang Cao was born in March, 1988 in Jinhua, Zhejiang, China. He enrolled at the University of Science and Technology of China (USTC) in 2006. In July 2010, he received his B.S. degree in Physics, and he started his Ph.D. program in the Department of Physics and Astronomy at Johns Hopkins University in August 2010. His research interest is in the field of Condensed Matter Physics and Materials Science. Since the January of 2012, under the supervision of Prof. Tim Mueller, he has performed research in Pt/Ni alloy catalysts for oxygen reduction reaction (ORR), and Cu & Cu-based alloy catalysts for CO_2/CO reduction through the first principle calculations and cluster expansion modeling. He is interested in developing and applying computational methods to build a direct bridge between the atomic structures of nano-scale materials and their properties so as to discover and design new materials. He has multiple papers published in or submitted to peer-reviewed journals including: Science, Journal of Physical Chemistry C, Nano Letters, and Nature Materials.